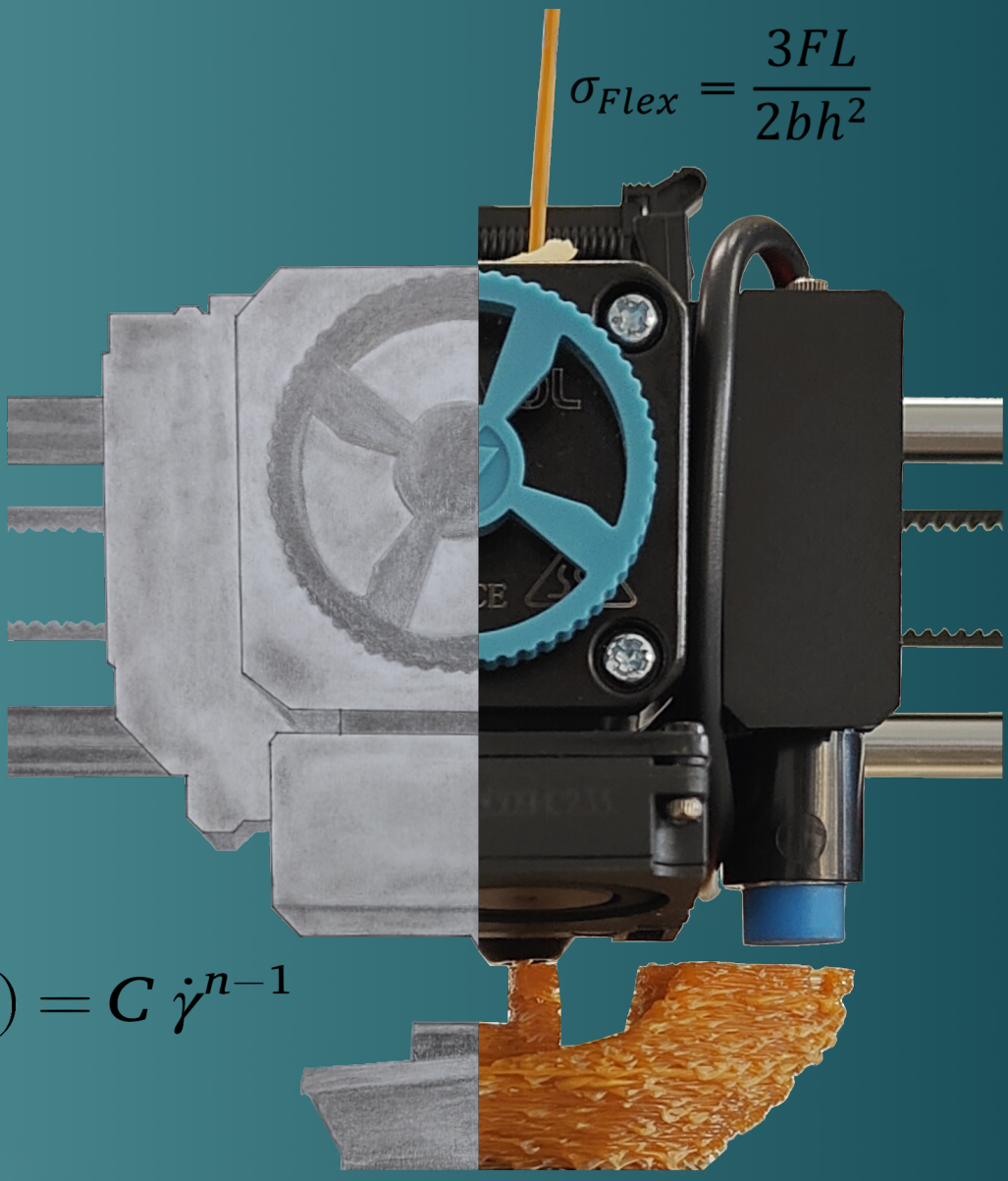
Strong, flexible and responsive

Reinventing structural material engineering using food ingredients

$$\sigma_{Flex} = \frac{3FL}{2bh^2}$$



$$\eta(\dot{\gamma}) = C\,\dot{\gamma}^{n-1}$$

Quinten Steffens

Propositions

1. Good robotic design combines rigidity with flexibility.
(this thesis)

2. Utilizing food materials to replace synthetic polymer materials reduces the environmental impact.
(this thesis)

3. The competitive nature of science compromises its efficiency.

4. Scientists need to leave communication of their results to communication experts.

5. Science is an artistic endeavour.

6. Right-to-repair is meaningless as long as proprietary tools are required for repairs.

7. People need to have full control over their pension funds.

Propositions belonging to the thesis, entitled

Strong, flexible and responsive: Reinventing structural material engineering using food ingredients

Quinten Steffens
Wageningen, 23 October 2026

Strong, flexible and responsive

Reinventing structural material engineering

using food ingredients

Quinten Steffens

Thesis committee

Promotors

Prof. Dr Remko M. Boom

Professor of Food Process Engineering

Wageningen University & Research

Prof. Dr Ruud G.M. van der Sman

Special Professor in Food Process Engineering

Wageningen University & Research

Co-promotor

Dr Lu Zhang

Assistant Professor of Food Process Engineering

Wageningen University & Research

Other members

Dr Leonard M.C. Sagis, Wageningen University & Research

Prof Dr Ir Edwin Zondervan, University of Twente, Enschede

Dr Paola Fanzio, Delft University of Technology

Dr Steven Cornet, Nederlands Instituut voor Zuivelonderzoek, Ede

This research was conducted under the auspices of VLAG Graduate School (Biobased, Biomolecular, Chemical, Food and Nutrition Sciences)

Strong, flexible and responsive

Reinventing structural material engineering using food ingredients

Quinten Steffens

Thesis

submitted in fulfilment of the requirements for the degree of doctor

at Wageningen University

by the authority of the Rector Magnificus,

Prof. Dr C. Kroeze,

in the presence of the

Thesis Committee appointed by the Academic Board

to be defended in public

on Friday 23 October 2026

at 3.30 p.m. in the Omnia Auditorium.

Quinten Steffens

Strong, flexible and responsive: Reinventing structural material engineering using food ingredients

217 pages

PhD thesis, Wageningen University, Wageningen, the Netherlands (2026)

With references, with summary in English

https://doi.org/10.18174/681733

Contents

Chapter 1	Introduction	7
Chapter 2	3D-printing of thermoplastic protein-based composites by fused deposition modelling	21
Chapter 3	Zein-based Edible Filament: Formulation Development, Fabrication and Fused Deposition Modelling Performance	61
Chapter 4	Mechanical characterization of elastic edible films with single, crosslinked and interpenetrating biopolymer networks using combined uniaxial and biaxial analysis	111
Chapter 5	General Discussion	155
References		173
Summary		191
Appendices		203

Chapter 1

Introduction

1.1 Rethinking material engineering using food ingredients

By exploring the opportunities that edible materials offer beyond direct consumption, numerous novel material applications can be uncovered that benefit human health, society and the environment. These materials could enable the development of advanced edible robots and robotic foods, while also revolutionizing simpler but highly impactful applications, including packaging, pharmaceutics, and food texturization. For example, they could be used to design safer sensors for *in vivo* health monitoring, environmental monitoring devices that fully biodegrade after use or tablets that provide controlled drug delivery (Bouman et al., 2015; Chambers et al., 2014; Floreano et al., 2024).

Since raw food materials are inherently complex and a large variability exists even within harvests of the same crop due to natural variance, it is not trivial to derive final product characteristics directly from raw materials, despite the attempts of many scientists. Although many theoretical models and equations have been used to describe the general properties of food systems, their applicability to complex food systems remains somewhat limited as ingredient interactions can yield behaviour that is not easily captured by simple models (De Angelis et al., 2024). As an example, the Krieger-Dougherty equation in combination with a power law can be used to describe the effective viscosity of food systems, but it cannot distinguish between the interactions of multiple components and is therefore less suitable to predict final product properties from ingredient characteristics (Lie-Piang et al., 2022).

However, (food) material behaviour can often be generalized at the level of composites. Composites are materials formed by combining one or more ingredients through specific formulation and processing steps. These

ingredients can include solvents, plasticizers, fibres, fillers and other additives, which influence matrix structures after processing. At the composite level, structure-function relationships that govern key composite characteristics can be derived (Joardder et al., 2017). For example, the relationships between formulation, processing and composite properties of gels and glasses have been well described. A better understanding of the relationship between formulation, processing and mechanical properties of the composites could aid the development of design guidelines for edible composites. These edible composites with designed properties could be utilized in applications that benefit health, society and the environment. Such a rational design approach greatly reduces trial-and-error in composite development. However, edible materials are currently studied almost exclusively in the context of food processing and sensorial qualities, so there is an urgent need for design guidelines that can be used to rationalize selection of food ingredients and processing methods to design composite materials with desired properties and functionality.

The main objective of this thesis is therefore to rethink structural material engineering using food ingredients and establish guidelines for the design of composite materials that possess the appropriate, strength, flexibility and responsiveness for their intended application. Such applications could entail the manufacture of edible robots and robotic foods.

1.2 Material requirements for the design of soft, edible robots

When designing a composite, it is paramount to keep the final application in mind. The properties required for composites materials suited for the design of edible robots and robotic foods are often inspired by biology (Floreano et al., 2024). This biomimicry approach is especially popular within the soft robotics field, where robots are fabricated using highly deformable materials

following bioinspired designs (Xavier et al., 2022). Typical examples include grippers inspired by elephant trunks and octopus tentacles, actuation mechanisms inspired by worms and snakes, underwater locomotion mechanisms inspired by fish, earth-penetrating robots inspired by living roots or even self-replicating and growing robots (Baumgartner et al., 2020; Del Dottore et al., 2018; Tang et al., 2022). Edible robots take this approach one step further, by allowing robots to become nutrition for organisms after their serviceable life, thereby also preventing environmental pollution (Floreano et al., 2024). To achieve more complex functionalities, multiple components can be integrated into assemblies (**Fig.1.1**). Each component may incorporate multiple composites, such as stiff, rigid ones for electronic circuits and scaffolds and soft, flexible ones for actuators and fluidic circuits.

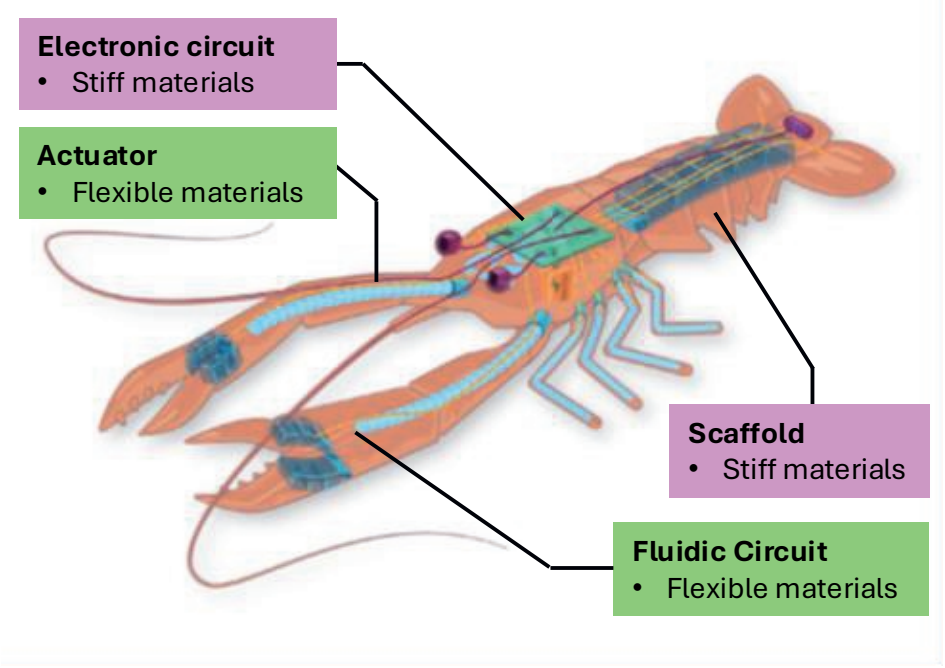


Fig.1.1 *Artistic rendition of a future edible robot showcasing a biomimicry approach. Both stiff, rigid and soft, flexible materials are required to fabricate the robot. Image modified from (Floreano et al., 2024).*

High material deformability, combined with low stiffness and organic movement patterns, enables soft robots to interact safely with dynamic environments and living organisms that are sensitive to physical contact (Tang et al., 2022). Locomotion in robots with compliant behaviour, such as the grippers inspired by elephant trunks and octopus tentacles, can be achieved using pneumatic actuation. Pneumatic actuators are lightweight, inexpensive to manufacture, offer fast response times and enable motion with high degrees of freedom (Xavier et al., 2022). Their simple, modular architecture also enables easy integration into a variety of robotic designs.

An elementary pneumatic actuator that is often used in scientific studies due to its simple and modular architecture is the 'pneunet', a pneumatic actuator that consists of multiple interconnected air chambers, with a stiff baseplate on one side (**Fig.1.2**). The ratio of the stiffness of the baseplate to the flexibility of the material that forms the air chambers provides a means to create anisotropy, which governs the bending or extending motion of the pneunet actuator as result of a change in pressure. Understanding the tensile, flexural, uniaxial extensional, and biaxial extensional properties of the actuator materials thus informs its design rationale. In this thesis, we focused on two distinct material behaviours with the ultimate goal of informing design choices for edible robotics. The first focus is on stiff and rigid materials to create strong bodies, such as scaffolds and exoskeletons. The second focus is on extendable, flexible soft materials to enable actuation. Integrating stiff and flexible materials in a single design, for example an artificial muscle or pneunet actuator, brings us closer to the realization of edible robots.

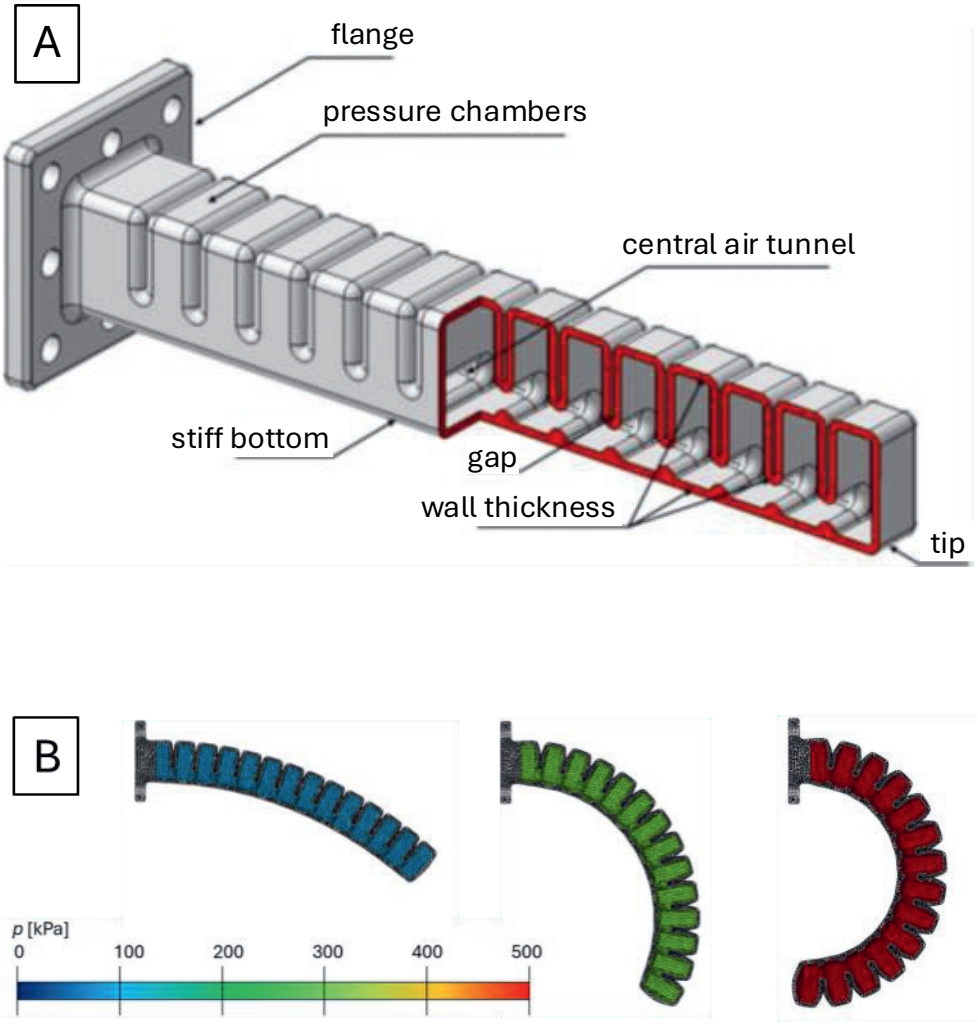


Fig.1.2 *A: sectional view of a pneunet actuator with a stiff base and flexible pressure chambers B: Numerically simulated deformation result for a thermoplastic polyurethane pneunet under internal pressurization between 0 and 500 kPa. Images modified from Schreiber at al. (2025).*

1.3 Fabrication methods and material development: challenges and opportunities

Since food production processes inherently have different goals from structural material manufacturing, the first research gap that is addressed in this thesis is how food process engineering and manufacturing technologies

can be combined to fabricate rigid and flexible composites with the desired material characteristics.

Research gap #1:
Beyond direct consumption, edible composite materials have the potential to enable innovations that benefit animal and human health, society and environment. However, it is not yet well understood how fabrication technologies can be applied to create composites with tailored properties. Therefore, the first research gap addressed is:

"How can food process engineering and manufacturing technologies be combined to fabricate rigid and flexible composites with desired material characteristics?"

Furthermore, processing technologies put constraints on the material formulation, that is, not every material is suited for every processing technology. For example, to obtain composites with anisotropic structure using extrusion processes, the raw materials should have the specific properties that enable the texturization during processing.

1.3.1 Stiff and rigid components by additive manufacturing

Material extrusion presents exciting opportunities to utilize food materials beyond food applications, such as the manufacture of packaging films or filaments (Rowat et al., 2021). Such filaments can be utilized in additive manufacturing processes, in which objects are constructed in a layer-by-layer fashion, such as 3D printing. The core principle of 3D printing is the sequential extrusion of material through a nozzle guided by a computer-aided design (CAD) model to fabricate complex objects. Commonly studied 3D food printing techniques include paste extrusion, melt extrusion, ink-jet printing, powder bed printing, sheet lamination and bio-printing (Nachal et al., 2019; Portanguen et al., 2019). Food printing is often employed to fabricate foods with personalized nutritional and textural properties

(Venkatachalam et al., 2023a). Since additive manufacturing eliminates the need for costly moulds and other tooling required in subtractive processes, food printing provides a cost-effective route to customized products. However, these methods for constructing customized foods yield objects with low mechanical strength and these objects often require post-processing to stabilize their shape and shelf life, such as heating or drying (Godoi et al., 2016a; Lille et al., 2018). On the contrary, fused deposition modelling is a 3D printing technique that is often utilized in engineering as it allows for manufacture of complex digital designs with low marginal cost and advantageous mechanical properties (Dey et al., 2021; Wallin et al., 2018). Moreover, the manufactured item does not need to post-processed to stabilize it, enabling high shape fidelity compared to common food printing technologies. However, prior to this thesis, only one scientific group had been able to develop edible feedstocks for FDM, and feasibility of large-scale production of such feedstock was not yet proven (Chaunier et al., 2017b).

To be compatible with the FDM process, a material needs to be thermoplastic. A thermoplastic material behaves like a fluid above a certain transition temperature, which enables hot melt deposition through a nozzle, but solidifies after cooling down. Protein composites naturally exhibit such transition behaviour, behaving as solid glasses below their glass transition temperature (T_g) and as fluid materials above their T_g. Since protein composites can be quite brittle, the addition of plasticizers is often required to reduce the brittleness of the final product, such as packaging films. Plasticizers weaken the intra- and intermolecular bonds between polymers, thereby reducing the glass transition temperature and brittleness. The effect of plasticizers on material states can be described using state diagrams.

Thus, edible composites can be formulated for the manufacture of rigid components of soft robots, such as scaffolds and exoskeletons, and these components can subsequently be fabricated using 3D printing techniques.

1.3.2 Soft and stretchable components through hydrogel formation

For the other focus, on extendable, flexible soft components that enable actuation, hydrogels are good candidates. These components can be fabricated from hydrogels using conventional moulding techniques or 3D printing techniques. For example, several highly stretchable, although non-edible, hydrogels suited for soft actuators have been 3D printed (Bakarich et al., 2013; Bootsma et al., 2017; Hong et al., 2015). Heiden et. al developed a 3D printing process for fabrication of a pneumatic actuator with fast response times using a gelatine-based hydrogel, with an important limitation being the inability to print overhangs or bridging structures (2022). Simultaneously, several edible, soft actuators based on conventional moulding techniques have been developed using hydrogels based on biopolymers such as gelatine and konjac (Chambers et al., 2014; Kanno et al., 2024; Shintake et al., 2017). Similarly to rigid materials, properties of such composites can be modified with additives, for example plasticizers or crosslinkers, which affect important tensile properties such as Young's modulus and fracture strength.

Edible hydrogels and films have been well studied in the context of biocompatibility and biodegradability and are highly favoured compared to conventional materials such as plastics. However, the tensile strength and flexibility of edible films are significantly lower than those of conventional packaging materials. The biaxial stress response is an important material property, yet it is not frequently analysed in studies evaluating the mechanical performance of hydrogels and films. However, the biaxial stress response is crucial for predicting a materials behaviour in applications such as soft

robotics actuators and packaging. Its importance has been widely recognized for materials applied in packaging, metal- and thermoforming and tissue engineering.

In general, food characterization methods are not aimed at evaluating foods in the context of material engineering, therefore the second research gap that needs to be addressed is how (food) characterization methods can be applied to study the performance of food materials in non-food applications, like structural material engineering. Preferably, such characterization methods should be fast and accurate to allow for rapid screening of many composites in order to derive general learnings on structure-function relationships that can be leveraged to guide material composite design.

Research gap #2:

To enable rational design of edible composite materials, characterization methods need to be developed to evaluate their properties in the context of their final application. However, in food science, materials are almost exclusively evaluated in the context of food processing and sensorial qualities. Therefore, the second research gap is:

"How can food characterization methods be applied to study the performance of edible composites in non-food applications, like structural material engineering?"

Measurement techniques that study planar biaxial stretching or membrane/bubble inflation can be utilized to quantify the biaxial stress response of materials. In the food industry, the alveograph has been developed to characterize biaxial deformation of bread doughs, but the device is currently limited to materials within a narrow range of characteristics (Dufour et al., 2024). To translate the mechanical characteristics of hydrogels in soft robotic applications or other 'high stretch' applications, it is thus necessary to develop a generally applicable biaxial characterization method

that efficiently provides reproducible data on the mechanical performance of composites under biaxial loads. The results can be used to model and predict the performance of flexible materials in soft robots.

1.4 Aims and outline of this thesis

This thesis aims to establish design guidelines for edible composites with desired properties by taking a material science approach to formulate and process food materials into composites and by developing novel analytical methods to evaluate their behaviour. The generated insights contribute to the future development of edible robots, robotic foods and other high-impact applications. The chapters reflect both of these aims (Fig. 1.3). To enable fabrication of rigid, edible composites, a modified 3D printer was developed in **Chapter 2** followed by filament fabrication in **Chapter 3**. **Chapter 2** focuses on flow behaviour of plasticized proteins under the effect of temperature and shear. In this chapter the rheological behaviour is described using theoretical models, and the learnings are used to 3D print plasticized proteins using a pellet extruder. Based on the insights from **Chapter 2**, **Chapter 3** investigates the material extrudability and the development of standardized filaments that are compatible with commercial 3D printers. This filament is used to 3D print simple shapes for analysis of flexural and tensile properties and more complex designs for evaluation of the 3D printing qualities of the material. In addition to rigid composites, **Chapter 4** focuses on formulating and processing highly stretchable edible hydrogels with different network architectures and evaluating their uniaxial and biaxial tensile properties by combining conventional uniaxial testing with a newly developed computer-vision-based biaxial testing method. These edible hydrogels are promising candidates for use in pneumatic actuators. The key findings on process and material development in this thesis are summarized

in **Chapter 5** and are discussed in the context of further development of edible robotics and other applications.

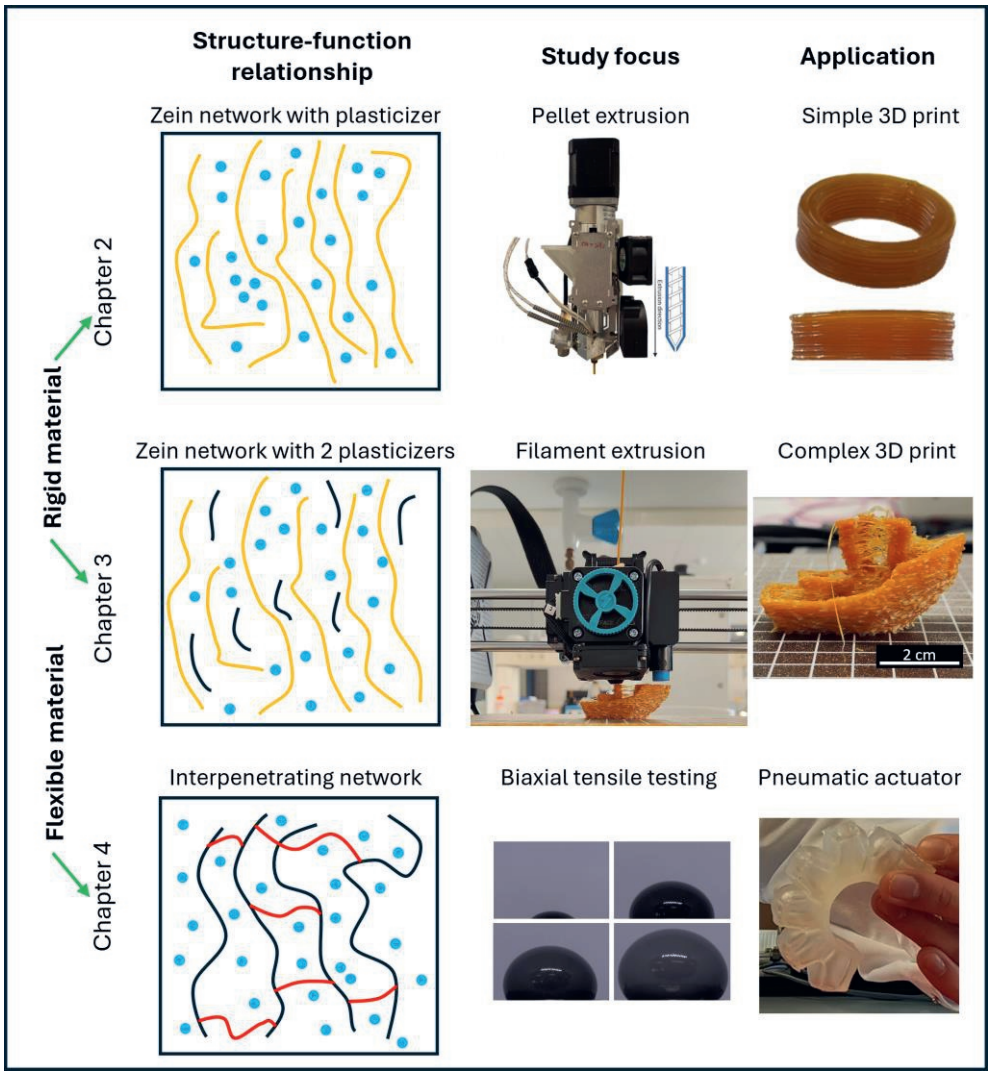


Fig. 1.3 Schematic overview of thesis topics and chapters


Q3 '26

Chapter 2

3D-printing of thermoplastic protein-based composites by fused deposition modelling

This chapter has been published as Steffens, Q., Vliek, M., Van der Sman, R.G.M., Boom, R. M., Zhang, L. (2025). 3D-printing of thermoplastic protein-based composites by fused deposition modelling. *Journal of Food Engineering*, 401, 112660. https://doi.org/10.1016/j.jfoodeng.2025.112660

Abstract

Proteins can be plasticized to create thermoplastic materials suitable for 3D printing using fused deposition modelling (FDM). This study investigates the plasticization of zein and calcium caseinate, and their blends, by glycerol regarding their thermal properties, rheological properties and 3D printing performance. Thermoplastic protein-based composites were prepared through a process of protein dissolution, plasticization, film casting and pelletisation. Calcium caseinate showed good miscibility with glycerol, whereas phase separation was observed in zein-based composites at higher glycerol concentrations. Zein-based pellets were successfully 3D printed by using a pellet extruder as the printhead. Stable 3D structures were printed without need for post-processing and an unsupported 45 degree overhang angle was achieved. Calcium caseinate-based pellets were not extrudable using the current setup due to their high viscosity. Furthermore, the thermal and rheological properties of protein composites correlated well with their printing performance. This study showed that protein-based composites are promising materials for FDM applications.

2.1 Introduction

Additive manufacturing (AM) provides several advantages for small-scale manufacture, such as fast prototyping and reduced use of materials and energy. Other benefits of AM include large design freedom, direct assembly of multiple components into a single piece and manufacture of components that cannot be produced using subtractive manufacturing methods. For these reasons, AM technologies such as 3D printing have been intensively studied in the fields of food engineering, tissue engineering and robotics (Floreano et al., 2024; Godoi et al., 2016b). For example, extrusion-based 3D printing has been employed to manufacture protein-rich food structures such as meat and fish analogues or protein bars from yield-stress materials (Cheng et al., 2025; Shi et al., 2023; Van Der Sman et al., 2024). 3D printed foods could be used promote healthier eating habits, provide novel gastronomic experiences or provide personalized nutrition (Floreano et al., 2024; Venkatachalam et al., 2023b). Recently, use of AM to produce edible robotic components such as flexible sensors and actuators has been explored (Choe et al., 2022; Edward and Golecki, 2023; Heiden et al., 2022; Y. Zhang et al., 2019).

In fused deposition modelling (FDM) the material is made flowable by heating it above its glass transition temperature (T_g) or melting point (T_m). The material cools and solidifies after deposition, which allows successive deposition of layers and hence creation of 3D structures (Vaes and Van Puyvelde, 2021). Most proteins are thermosetting due to their thermal denaturation. Some proteins like zein and caseinate exhibit thermoplastic behaviour that is comparable to that of traditionally used polymers (e.g. polylactic acid), which make them potential feedstocks for FDM of edible, or bio-compatible materials (Chaunier et al., 2017b).

In this study, we investigate the suitability of casein and zein for FDM. Zein is a byproduct of the extraction of oil and starch from corn meal (Tallawi et al., 2023) and fully digestible by humans (Kianirad et al., 2021). Due to its excellent biocompatibility, hydrophobic properties and slow dissolution rate it is frequently studied as carrier material for pharmaceutical compounds or as encapsulation material for foods (Bouman et al., 2015; Kasaai, 2018). Casein has traditionally been used not just as food ingredient, but also as paint and glue. When crosslinked it can be used to make buttons and fibres for textile (Lanital or Aralac). Use of caseinate in packaging materials has been explored as well, as its high density of polar groups makes it a good barrier to non-polar substances like oxygen and carbon dioxide (Arrieta et al., 2013; Bonnaillie et al., 2014; Chevalier et al., 2018).

Zein has a compact globular structure and casein has a micellar structure, therefore neither protein is prone to unfolding and denaturation upon heating. When heated above their glass transition temperatures the intermolecular bonds are weakened, which is a thermos-reversible process. However, both proteins have relatively high glass transition temperatures, and use of the pure proteins for FDM would require heating them near their thermal degradation temperature to achieve sufficient flowability. This can be resolved by incorporating plasticizers, which lower their T_g and reduce the brittleness of thermoplastic materials (Hernandez-Izquierdo and Krochta, 2008). Many chemicals can act as plasticizer, with glycerol being a promising candidate as it is a small, non-volatile molecule. Thus is does not evaporate during FDM. It has been reported that glycerol-plasticized zein can be extruded into an amorphous thermoplastic filament suitable for FDM (Chaunier et al., 2017b). Developing the suitable formulation using blends of zein and casein with plasticizer and may yield composites that fall within the window of rheological properties for printability (Oechsle et al., 2016). Recently, Duty

et. al (2018), Das et. al (2021) & Sola (2022) provided excellent reviews on evaluating the suitability of a polymer feedstock for FDM. Their frameworks are summarized in the theory section of the current work and utilized to evaluate if our composite materials meet fundamental conditions for successful 3D printing using FDM.

It is hypothesised that the thermorheological properties of a material correlate with its processability and can be tuned through adjusting their composition. To assess this, we investigated the effect of the formulation of zein and casein blends in combination with glycerol as plasticizer. We assessed their thermorheological properties and 3D printing performance. Modulated differential scanning calorimetry (DSC) was employed to determine the glass transitions of the composites. Temperature- and shear-dependent complex viscosity of the composites were determined using a closed cavity rheometer (CCR) which can operate at temperatures above 100 °C. A novel processing route was developed to ensure homogeneous composite materials, involving protein dissolution, plasticization, casting, evaporation and pelletizing. Obtained pellets could be fed directly to FDM printer. The findings of this research will contribute to the further advancement of FDM using edible, biocompatible materials.

2.2 Theory

2.2.1 Material requirements in FDM

A material is considered printable when it meets four requirements: (1) it can be extruded out of a nozzle, (2) it can hold its shape after deposition until the next layer is deposited, (3) it is capable of interlayer welding and (4) it remains stable during cooling to ambient temperature (Das et al., 2021; Duty et al., 2018; Sola, 2022).

To fulfil requirements 1 and 3, the viscosity of a material should be around 200 Pa·s or lower based on measurements at a shear rate of 100 s^{-1}, which is in the middle of the shear rate range of 30-200 s^{-1} that has been reported for FDM processes (Ajinjeru et al., 2017; Chaunier et al., 2017b, 2018; Das et al., 2021; Gilmer et al., 2018; Spoerk et al., 2017).

Furthermore, the extruders feeding mechanism must be able to provide enough force to push the softened material out of the nozzle. To fulfil requirement 2, a rapid transition in viscosity after extrusion is required: via lower shear rate and cooling solidification is induced. Typically, plastics utilized in FDM exhibit shear thinning during flow (Sola, 2022). This helps the material to set after it moves from a high temperature, high shear conditions in the nozzle to a low shear, low temperature conditions after deposition (Ma et al., 2022). To fulfil requirement 3, newly deposited material should be able to bond to previously deposited material through molecular diffusion in a viscous-flow sintering process with surface tension as main driving force. There is somewhat of a trade-off between requirement 2 and 3 because viscosity increase after deposition needs to be sufficiently fast for mechanical stability, but slow enough to allow fusing of the printed layers (Chaunier et al., 2018; Heiden et al., 2022). Requirement 4 can be achieved by minimizing thermal stresses over the printed object.

One of the major challenges in filament based FDM printing is the production of filaments, which are the most common feedstock for FDM processes. Production of filament requires the material to be processable without thermal degradation. The extruded filament should have a consistent diameter and sufficient bendability for spooling (Sola, 2022). During preliminary testing our composites failed to meet these requirements for the production of filament. FDM processes can also use pellets as feedstock, which are less

demanding during pre-processing. Pellet-fed FDM was therefore chosen for this study.

2.2.2 Thermal-rheological properties of composites

The processability of thermoplastic composite materials during FDM is related to their thermal and rheological properties. In this study, the glass transition temperature (T_g), shear viscosity and viscosity at different temperatures were determined experimentally. Using theoretical models to describe the experimental data can help to understand how composite materials can be optimized for FDM technology (see **Eq. 2.1-2.3**).

Specifically, shear rate dependency of viscosity can be described by the Ostwald-de Waele power law model (Acierno and Patti, 2023):

$$\eta(\dot{\gamma}) = C\,\dot{\gamma}^{n-1} \qquad \textit{Eq. 2.1}$$

With η the viscosity (Pa·s), $\dot{\gamma}$ the shear rate (s^{-1}), C the flow consistency index ($Pa \cdot s^n$) and n the power law index (-).

In addition, viscosity as function of temperature can be described by the WLF-equation:

$$log\left[\frac{\eta_T}{\eta_{T_g}}\right] = \log[a_T] = \frac{-C_1(T - T_g)}{C_2 + T - T_g} \qquad \textit{Eq. 2.2}$$

With η_T and η_{T_g} complex viscosity (Pa·s) at temperature T and T_g (K) respectively, a_T a shift factor (-) and C_1 (-) and C_2 (K) material-dependent coefficients (Acierno and Patti, 2023).

Moreover, the effect of plasticization with glycerol on the T_g of protein-based composites can be described with the Gordon-Taylor equation:

$$Tg = \frac{T_{g,pl} \cdot \omega_{pl} + k \cdot T_{g,pr} \cdot \omega_{pr}}{\omega_{pl} + k \cdot \omega_{pr}} \quad \textit{Eq. 2.3}$$

With T_g, $T_{g,pl}$, and $T_{g,pr}$ (K) the midpoint temperature of the glass transition for a protein-plasticizer blend, plasticizer or protein respectively and with ω_{pl} and ω_{pr} the mass fraction (-) of plasticizer and protein respectively (Skrdla et al., 2017). The Gordon-Taylor constant k (-) is inversely proportional to the plasticizing effect of the plasticizer on the protein.

2.2.3 Estimation of shear rate in nozzle, pressure drop and extruder force

By estimating the pressure drop these composites experience during extrusion through a nozzle, the required extrusion force can be determined (see **Eq. 2.4-2.7**). This information is useful in determining the processibility of the composites using FDM.

During FDM, the volumetric output of the extruder screw per unit of time needs to match the required flow rate, to avoid under or over-extrusion during FDM. As many materials have shear dependent viscosities, it is important to establish the relation between the materials' shear thinning properties and its flow rate. The Rabinowitsch-corrected shear rate $\dot{\gamma}$ (s^{-1}) in a cylindrical capillary during extrusion is given by:

$$\dot{\gamma} = \frac{Q}{\pi R^3} \frac{3n+1}{n} \quad \textit{Eq. 2.4}$$

With Q the flow rate (m^3/s), R the nozzle radius (m) and n the power law index (-) (Duty et al., 2018). The pressure drop across the nozzle for power-law liquids can be described by the modified Poiseuille equation:

$$\Delta P = \frac{2LC}{R}\left(\frac{Q}{\pi R^3}\frac{3n+1}{n}\right)^n \qquad \textit{Eq. 2.5}$$

with ΔP the pressure drop (Pa), L the length of the nozzle bore (m), η the viscosity (Pa·s), L the nozzle length (m), Q the flow rate (m^3/s) and R the nozzle radius (m) (Chhabra and Richardson, 2011; Schutyser et al., 2018). Here we assume fully developed laminar flow and no slip conditions at the wall of the nozzle. The distribution of flow rate and pressure over the radius of the nozzle can be further defined by defining a friction factor and Reynolds number, but this is beyond the scope of this article. As long as the pressure drop over the nozzle for a desired flow rate Q is lower than the maximum system pressure, flow rate Q can be achieved (Duty et al., 2018). The maximum system pressure can be calculated according to

$$\Delta P = \frac{F}{A} \qquad \textit{Eq. 2.6}$$

with A the cross-sectional area of the screw (Chaunier et al., 2018). The theoretical maximum force F (N) that can be provided by the motor is given by:

$$F = \frac{T\,G}{r} \qquad \textit{Eq. 2.7}$$

With T the holding torque (N·m), G the gear ratio (-) and r (m) the radius of the drive gear.

2.3 Materials and Methods

2.3.1 Preparation of plasticizer-protein composites

Composites manufactured through blending of protein and plasticizer yielded powder mixtures with poor flowability. This resulted in uneven flow rates of feed material to the extrusion screw resulting in uneven extrudate flow. A solvent casting method was adopted to improve the homogeneity of protein/plasticizer blends and with that the consistency of the extrudate flow. After grinding, free-flowing pellet was obtained which can be either directly 3D printed using the pellet-fed FDM printer. Production of composite filament was attempted. However, due to brittleness of the filament, this processing route was not further pursued in the current work.

The composite materials were prepared through i) protein dissolution and plasticization; ii) film casting, evaporation and iii) pelletizing (see **Fig. 2.1**). Specifically, zein powder (Z3625, Sigma Aldrich, ≤8% water) was dissolved in 96% ethanol (VWR chemicals). To fully dissolve the protein, the zein solution was heated to 60 °C and stirred at 200 RPM for 2 hours on a hot plate. Spray-dried calcium caseinate (CaCas) (FrieslandCampina) was dissolved in demineralized water at room temperature while stirring at 200 RPM for 2 hours. Blends of zein and CaCas were dissolved in 96% ethanol. Bidistilled glycerol (24388, VWR chemicals) was added to the protein solutions as the plasticizer. After dissolution, the composites were cast as films of 1-2 mm thickness in rimmed silicone sheets. Zein composites were dried at ambient temperature in a fume hood for 96 hours. CaCas-composites were dried in an oven at 55 °C for 48 hours. Dried films were ground using a spice grinder (Waring Commercial) and sieved through a 3 mm mesh sieve. Obtained pellets were stored in airtight containers prior to further analysis. The concentration of glycerol in the protein-based composite material ranged from 0% w/w to 35% w/w.

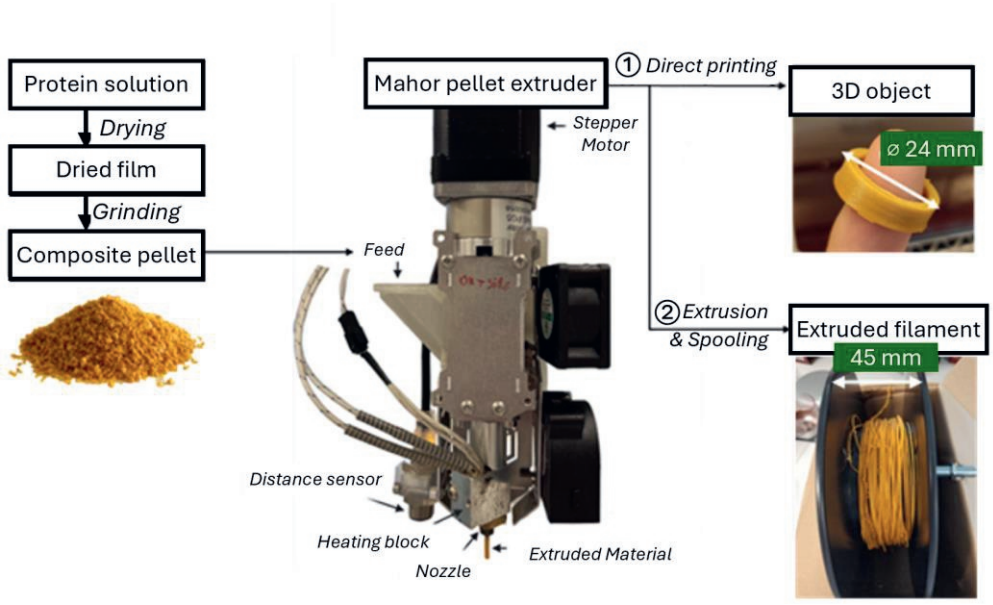


Fig. 2.1 *Schematic overview of the processes used to fabricate thermoplastic protein-based composite materials for fused deposition modelling. Pellets were produced by following the steps outlined in this schematic. Pellets can used as the feedstock in pellet-fed FDM process to directly print 3D structures or to produce filament.*

2.3.2 Rheological measurements

Rheological properties of the plasticized protein composite materials were analysed with a Closed Cavity Rheometer (CCR) (RPA Elite, TA instruments), including critical strain, temperature- and frequency-dependent complex viscosity. We assumed the Cox-Merz rule is valid for our data and can be used to determine steady shear viscosity from complex viscosity (Chaunier et al., 2017a).

For each CCR measurement, a 4.15 ± 0.05 g aliquot of pellet was sandwiched between two layers of polyester film and positioned in the CCR's cavity before the chamber was sealed at a pressure of 4 bar. The procedure used to analyse the CCR data is provided in the Supplementary Materials.

2.3.2.1 Determination of critical strain using oscillatory strain sweep

In the linear viscoelastic regime (LVR) the viscoelastic properties of a material are strain independent. This independency is lost above a critical strain (C^*), where the microstructure of the material is changed as result of deformation. For polymers, critical strain increases with temperature and decreases with frequency (Whitcomb, 2023).

The critical strains of all plasticized protein composite materials were determined through strain sweeps, performed at the lowest temperatures relevant for FDM, being 100 °C for CaCas composites and 110 °C for zein composites. The strain during strain sweeps was increased from 0.1 to 128% at a constant frequency of 10 Hz. The strain at which the storage modulus (G') was equal to 90% of its plateau value was defined as the critical strain (Whitcomb, 2023).

2.3.2.2 Shear rate dependency of complex viscosity

Complex viscosity as function of shear rate was determined by performing strain sweeps corresponding to shear rates from 0.02 to 80 s^{-1} at a constant frequency of 10 Hz and a temperature of 100 °C for CaCas composites and 110 °C for zein composites. The experimental data was fitted to the power law model (see **Eq. 2.1**).

2.3.2.3 Temperature dependency of complex viscosity

The strain was set below the critical strain to exclude influence of shear on viscosity. Complex viscosity data was recorded while the samples were heated from their T_g to 140 °C (zein) or 160 °C (CaCas). The material-dependent coefficients C_1 and C_2 were computed by minimizing the sum of squares difference between the experimentally obtained value of $\log[a_T]$ and the value calculated using C_1 and C_2 (**Eq. 2.2**). We fit the data from T_g to $T_g + 40$ °C as WLF is not valid below T_g and to prevent thermal degradation.

In short, we used the Solver function in excel to minimize: $L_2 = \sum_{Tg}^{Tg+40}\left(log\left[\frac{\eta_T}{\eta_{T_g}}\right] - \frac{-C_1(T-T_g)}{C_2+T-T_g}\right)^2$

2.3.3 Determination of glass transition temperature using modulated DSC

Glass transition temperatures were determined by modulated DSC on a DSC250 (TA Instruments). For this analysis, samples were sealed in non-hermetic, aluminium pans. The thermal analysis profile consisted of a first heating step from 20 °C up to 18 0°C at 15 °C/min to evaporate any free moisture in the samples, after which samples were equilibrated at 20 °C. Next, temperature modulation was enabled with an amplitude of 1.27 °C and a period of 60 seconds. During a second heating step the temperature was increased to 180 °C (zein) or 220 °C (CaCas) at a rate of 2 °C/min. Above these temperatures rapid thermal degradation of proteins occurs (see thermogravimetric analysis (TGA) results in Supplementary Materials) (Arrieta et al., 2013; Selling, 2010).

The T_g was determined as the inflection point of the shifted part of the thermograph (i.e. a shift in the baseline of the reversing heat flow signal), using the data obtained during the second heating cycle. We determined the exact temperature at which the inflection occurred with the 'glass transition' analysis function of TRIOS software (v5.6.0.87, TA instruments), selecting an analysis range of 30 °C under and over the visually apparent T_g in the thermograph.

The experimentally determined T_g values were fitted to the Gordon-Taylor equation (see **Eq. 2.3**). We used $T_{g,pl} = -83$ °C for glycerol (Enrione et al., 2010; Schröter and Donth, 2000; Sou et al., 2011; Zondervan et al., 2007) and $T_{g,pr}$ of pure zein and calcium caseinate as determined by DSC as input for

the model fitting. Values for k were determined by minimizing the residual sum of squares between measurement data and model prediction for miscible protein-plasticizer blends using the solver add-in in Microsoft Excel.

2.3.4 Pellet-fed 3D printing

A commercial FDM printer was modified to enable pellet-fed FDM. A single-screw extruder with a 6.25:1 length/diameter (L/D) ratio (MAHOR PX0850 v4, Spain) was mounted on the toolhead of a Felix Tec 4c 3D printer controlled through Repetier firmware (Felixprinters, The Netherlands). The extruder was driven by a Nema 17 bipolar stepper motor with a 5.18:1 planetary gearbox (17HS19-1684S-PG5). A resistive heating element inside an aluminium heating block converts power to heat, which the block transfers to the extruder barrel. The block was installed close to the nozzle (**Fig. 2.1**).

A hollow cylinder design with an inner diameter of 14 mm, height of 5 mm and wall thickness of 2.4 mm as well as a cone with a height of 10 mm, wall angle of 45° and wall thickness of 2.4 mm were designed using Solidworks 2021. Printer instructions (gcode) were generated using Orcaslicer V2.1.0. A 0.8 mm line width and a concentric print pattern were used, so objects were printed as 3 concentric circles per layer. Full slicer profiles can be found in Appendix (**Table A2.3)**.

The build plate temperatures was set (and recorded) on the printer, just below the glass transition temperature of the composites to improve bed adhesion and minimize the thermal gradient within the printed object to minimize deformation due to uneven shrinkage (warping). For composites that did not stick to the build plate, 3DLAC (Laiseven cosmetics) was used as adhesive on the build plate. Heating block temperature was chosen based on temperature sweep tests and increased to compensate for limited residence time of materials in the heated zone.

2.4 Results and discussion

2.4.1 Glass transition temperatures of protein composites

Fig. 2.2A shows the glass transition temperatures values of zein plasticized with glycerol. The values for pure zein powder were determined to be 158 ± 2 °C, which is close to the value of 164 °C reported by Di Gioia (1999). A small thermal transition was observed at around 96 °C on the thermogram of pure zein (Appendix, DSC section). Zhang et. al (2022) found a T_g of 93 °C for *α-zein* having a 7% moisture content. The small thermal transition we observed is thus most likely due to the presence of *α-zein*.

As expected, the glass transition temperatures of zein-based composites decreased with increasing glycerol content. At higher plasticizer concentrations ($\omega_{pl} \geq 0.125$) instead a discontinuity is observed. At the same time, the glass transitions become wider (see Appendix Fig. A2.9). Both observations are likely to be caused by the limited miscibility between zein and glycerol, which causes phase separation at higher glycerol concentrations. Whilst being a plasticizer, glycerol has limited miscibility with zein (Chaunier et al., 2017b; Rowat et al., 2021). At concentrations higher than its miscibility glycerol rich domains in a zein matrix will be created (Renzetti et al., 2021). Gontard and Ring (1996) reported that increasing levels of plasticizer in wheat gluten films resulted in broadening of the dynamic mechanical thermal analysis (DMTA) tan δ peaks, which was attributed this to the limited miscibility between the protein and the plasticizer. In the same study, good correspondence of T_g obtained by DSC and DMTA was found. Pommet et. al (2003) reported a limited compatibility between plasticizer and protein evidenced by DSC.

We observed the development of an liquid film on the surface of dried zein sheets, providing further evidence for the separation of glycerol from the zein

matrix. Due to strong intermolecular and intramolecular attractions in zein molecules, glycerol may be forced out of the zein matrix during drying.

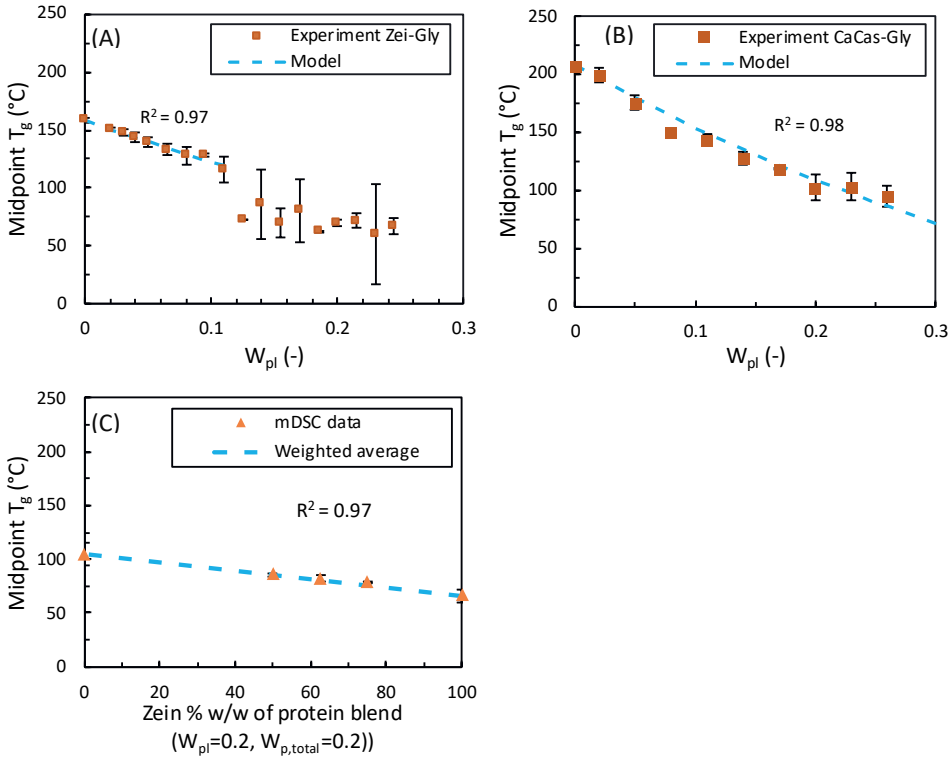


Fig. 2.2 *Midpoint glass transition temperature Tg of samples determined by modulated differential scanning calorimetry: (a) zein (Zei) and (b) calcium caseinate (CaCas) plasticized with different concentrations of glycerol (gly), and (c) Zei/CaCas blends plasticized with 20 % w/w of glycerol. Dashed lines in (a) and (b) indicate fitting results using the Gordon Taylor equation; dashed line in (c) indicates the calculated Tg Zei/CaCas blends based on the mass ratio of zein and CaCas.*

Fig. 2.2B shows the glass transitions of CaCas-based composites as affected by glycerol. The T_g of pure CaCas powder was determined to be 208 ± 3 ℃, very close to the T_g of anhydrous rennet casein at 206 ℃ as reported by Bengoechea et. al (2007). The glass transition temperature decreased fairly linearly with the concentration of glycerol. Based on these results caseinate and glycerol appear well miscible. From sorption isotherms in literature it is evident that the hydrophilicity of calcium caseinate is higher than that of zein

(Rüegg and Moor, 1984; Tillekeratne and Easteal, 2000). Yet, phase separation was observed during storage over a week of CaCas-based samples with $\omega_{pl} \geq 0.35$ (data not shown). At $\omega_{pl} \geq 0.40$ the composites have a T_g below room temperature, and thus are in the rubbery state. This means that these materials fail the material requirements for FDM.

The effects of glycerol on the T_g of zein (up to $\omega_{pl} = 0.125$) and CaCas composites were effectively described by the Gordon-Taylor equation. The fitting parameter k was found to be 0.63 for zein-based ($R^2 = 0.97$) and 0.49 for CaCas-based ($R^2 = 0.98$) composites, respectively. The slightly higher fitting parameter k for the zein-glycerol system could be indicative of a somewhat lower plasticizing effect of glycerol on zein (Kalichevsky et al., 1993). We expect that this is related to the lower compatibility of the hydrophilic glycerol with the hydrophilic regions within zein. Casein is more hydrophilic and therefore has better compatibility with glycerol.

Moreover, blending zein and CaCas could result in composite materials with intermediate properties, and may mitigate the miscibility issues between glycerol and zein. By varying the mass ratio between zein and CaCas, protein composites containing 80% w/w protein and 20% w/w glycerol were obtained. The glass transition temperatures of these blends are the weighted average of the T_g values of the two components (i.e. zein 80%-gly 20% and CaCas 80%-gly 20%) (**Fig. 2.2C**). This linear relation allows possible interpolation of the glass transitions over the whole range of zein/CaCas blends tested in this study and provides evidence the materials are well mixed.

2.4.2 Rheological properties of protein composites

2.4.2.1 Critical strain determined by amplitude strain sweep

The storage modulus G' and loss modulus G" of the protein composites were measured using amplitude strain sweeps. Both G' and G" remained constant until a critical strain was reached. Zein- and CaCas-based composites both showed strain softening above a critical strain, and the measured critical strain increased with plasticizer content (see **Fig. 2.3**). The same kind of strain softening behaviour was also reported for plant proteins plasticized with water, which is a known phenomenon in polymer flow (Van Der Sman et al., 2023; Whitcomb, 2023). It is noteworthy that the critical strain was low (~1 %) at plasticizer contents relevant for use in FDM ($W_{pl} \approx 0.2$, to avoid phase separation associated with higher W_{pl}). This implies that strain softening of the printing material is likely to occur during FDM. The decrease of G', G" and the complex viscosity due to strain softening at higher shear could be beneficial for the FDM printing process because a lower extrusion force will be needed.

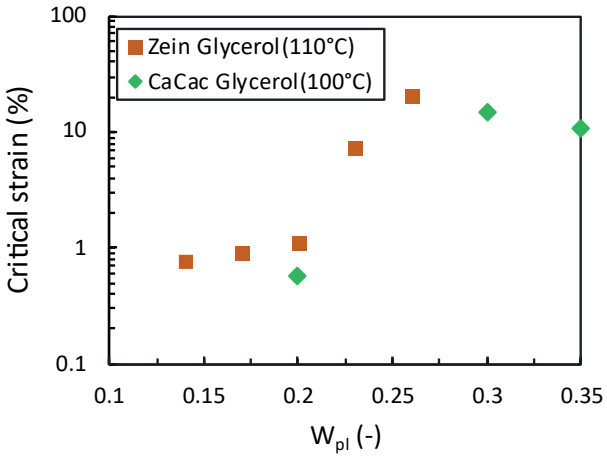


Fig. 2.3 *Critical strain of zein- and CaCas-based composites as a function of glycerol content (Wpl (-)) as determined by amplitude strain sweep tests.*

2.4.2.2 Shear dependency of viscosity

During FDM, polymer materials flow under shear. In this study, we used Eq. 4 to estimate the Rabinowitsch-corrected shear rate for composites flowing through the nozzle of the pellet extruder. With R = $4.0 \cdot 10^{-4}$ m and Q = $3.3 \cdot 10^{-9}$ m^3/s (a representative setting chosen for our printing experiments, see Section 2.4.3), we found a Rabinowitsch-corrected shear rate of 79 s^{-1}, which is in line with literature. Shear rate values of 40-200 s^{-1} for a nozzle with bore size of 0.3 mm (Gilmer et al., 2018) and 30-100 s^{-1} for a nozzle with bore size of 0.76 mm (Ajinjeru et al., 2017) were reported before. Materials used for FDM often show shear dependency of viscosity. Here, we determined the shear viscosity of protein composites under relevant conditions to better understand their behaviour. The shear rate range tested was up to 100 s^{-1} (set according to the estimated Rabinowitsch-corrected shear rate).

The power law model (**Eq. 2.1**) was used to describe the shear viscosity of protein composites formulated in this study (**Fig. 2.4**). The power law model was able to describe the viscosity from 1 s^{-1} to 100 s^{-1} for CaCas-based samples (see **Fig. 2.4A** for results of a representative sample). Nevertheless, only part of the viscosity data of zein-based samples was fitted to the power law model (see **Fig. 2.4B** for results of a representative sample).

Fig. 2.4C shows the consistency index C and power law index n of samples containing different levels of glycerol. For both zein- and CaCas-based samples, consistency index decreased as the concentration of glycerol increased. Interestingly, after an initial drop, the consistency index seems to have reached a plateau value when more plasticizer is added (**Fig. 2.4C**). The addition of plasticizers can reduce intermolecular interaction between polymer chains and increase free volume in the network because they insert

in between polymer molecules and form secondary bonds (e.g. hydrogen bonds) with the polymer chains (Arrieta et al., 2013; Eslami et al., 2023; Wang et al., 2023). This reduction in bond strength between polymer chains lowers the yield stress of a material, which explains the lower consistency index. However, as more plasticizer is added, fewer polymer-polymer interactions remain and the reduction of intermolecular polymer interaction by adding more plasticizer will become less effective.

Furthermore, the power law index n was found to be lower than 1 for all tested samples, indicating shear thinning properties (**Fig. 2.4C**). Shear thinning behaviour of a material is a result of internal structure changing during flow. At rest, the polymer molecules conform to the most thermodynamically favourable structure, which in a network is often a coiled up confirmation to minimize exposure of their hydrophobic/philic groups to the surrounding. Under shear, these coils are stretched out and disentangled whilst hydrogen bonds are broken, allowing the polymer molecules to align with the flow. This reduces the overall resistance of the material to flow, which can be observed as shear-thinning behaviour with decreasing viscosity at higher shear rates. Here, we observed increasing glycerol content resulted in an increase in the shear thinning index, indicating the sample became less shear thinning. Most likely, the addition of plasticizer reduces unfavourable exposure of the side-chains to the environment. Therefore, the alignment effect caused by shear (inducing laminar flow) is also reduced, resulting in a reduction in the power-law index of the protein composites.

It is interesting to compare the shear thinning properties of our protein composites with some common materials used for FDM. Values reported in literature for the consistency index C and power law index n of common 3D printing polymers vary widely, for ABS n = 0.27-0.51 and C = 6.7-12.2 kPa·s^n

and for PLA $C = 2.9$ kPa·s^n and $n = 0.32$-0.68 at printing temperatures (Chen and Smith, 2021; Sanchez et al., 2019). This large spread of fitting parameters could be because different additives are included in the filaments by manufacturers. For a zein composite with 20% glycerol we find C=4.7 kPa·s^n and $n = 0.57$ (-) at 110 °C (**Fig. 2.4B**), which are within the range of values commonly reported for FDM plastics. Therefore we expect it is feasible to use this material for FDM.

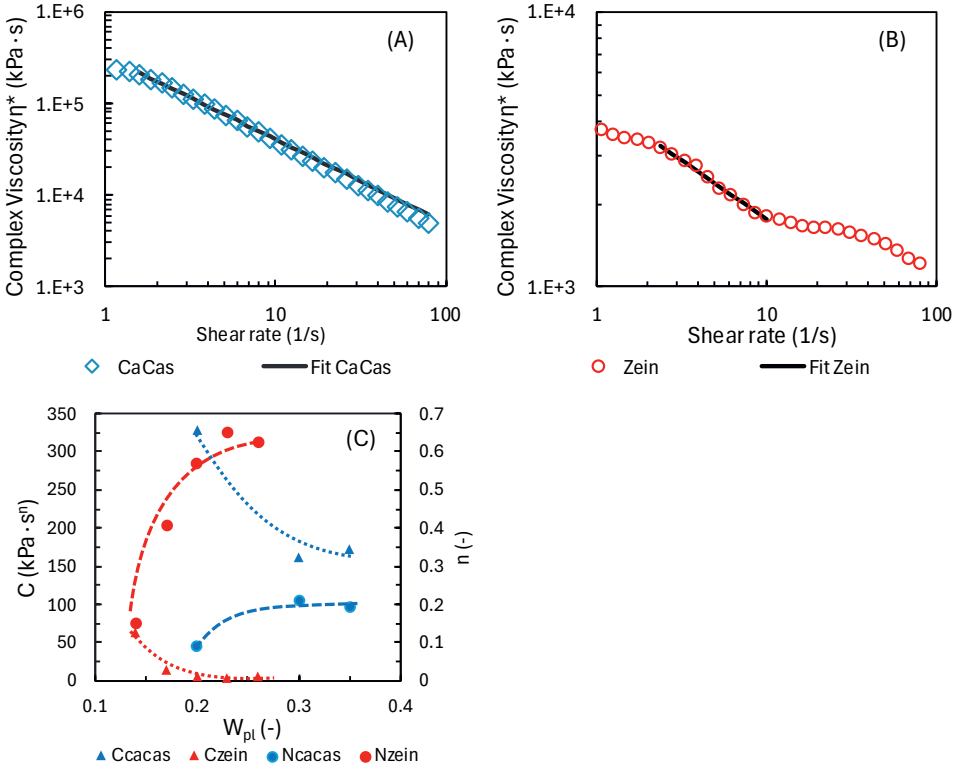


Fig. 2.4 *Complex viscosity as function of shear rate measured by CCR for CaCas (A) and Zein (B) sample each plasticized with 20% glycerol, and their fit using power law. C: Consistency index C and power law index n (parameters of power law fit) as function of glycerol content for zein and CaCas plasticized with glycerol. Dashed lines drawn to guide the eye.*

2.4.2.3 Temperature dependency of viscosity

During FDM, material flow is induced by extruding the printing material at elevated temperatures. The viscosity of a material should be low enough at the printing temperature so the motor can push the material out of the nozzle. Previously, a viscosity value of 0.2 kPa·s has been suggested as a target for material to have good printability and bonding after deposition (Spoerk et al., 2017). The temperature-dependent behaviour was determined for zein- and CaCas-based composites and zein-CaCas blend (**Fig. 2.5**). At a glycerol concentration of 20%, the complex viscosity of all three samples decreased as the temperature increased (**Fig. 2.5A**). Zein composite with 20% glycerol reached a viscosity of 0.2 kPa·s at 135 °C. Furthermore, this sample had G”>G’ over a wide temperature range, which means viscous behaviour is dominant. CaCas- and protein-blend-based composites did not reach a viscosity lower than 1 kPa·s even when heated to 150 °C. Additionally, these samples had G’>G”, meaning solid-like behaviour is dominant under the tested conditions.

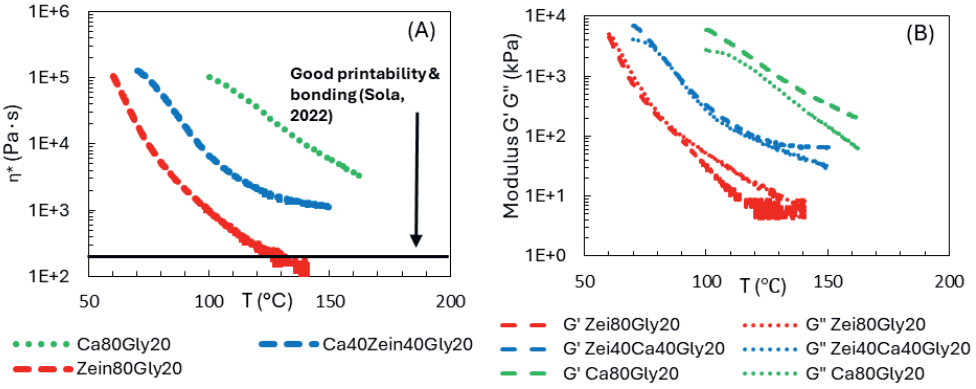


Fig. 2.5 *A: Complex viscosity of Zein80Gly20, Zein40Ca40Gly20 and Ca80Gly20 samples as function of temperature. B: Storage modulus (G’, dashed line) and loss modulus (G”, dotted line) as function of temperature for of Zein80Gly20, Zein40Ca40Gly20 and Ca80Gly20 samples.*

The viscosity of CaCas-based composites can be further reduced by increasing the temperature. However, thermal degradation of CaCas starts at 198 °C (Arrieta et al., 2013). We observed darkening of the colour of CaCas-based composites when the maximum measuring temperature was set to 180 °C or above in the DSC. Similar colour change was also observed during extrusion experiments. Thermogravimetric analysis of protein composites confirmed this observation was caused by thermal degradation of protein (see Supplementary materials). Adding more glycerol, up to 35% w/w, could reduce the viscosity of CaCas-based composites without causing phase separation. Even then, the viscosity of CaCas-based composites did not meet the 0.2 kPa·s target at the maximum processing temperature. This implies that CaCas-based composites were not suitable for FDM. Indeed, in the current work FDM of CaCas was only found feasible when combining it with zein to achieve blend with sufficiently low T_g and viscosity (see **section 2.4.3**).

The temperature-dependent viscosity of concentrated polymers can be described with Williams–Landel–Ferry equation (**Eq. 2.2**). Here, we took the η_{T_g} of each formulation as the measured viscosity at the corresponding T_g determined calorimetrically for the model fitting, instead of using the universal value of ~ 10^{12} Pa·s (see **Fig. 2.2**). The fitting parameters C_1 = 4.02 K and C_2 = 79.3 K in the modified WLF model were obtained for our protein composites (**Fig. 2.6**). These values deviate from the 'universal values' of C_1 = 17.44 and C_2 = 51.6 K reported for synthetic polymers (Williams et al., 1955). The authors of the WLF model advise against using these universal values unless no other data is available. Previous studies also have reported material specific values for C_1 and C_2 (Barra and Mitchell, 2013; Maidannyk and Roos, 2016). It seems the WLF model could potentially be used to predict the viscosity of protein composites containing different amount of glycerol at temperature slightly above T_g (Williams et al., 1955). To translate these

results to high-shear conditions (that are relevant for FDM processes), several authors have captured the effects of shear and temperature on viscosity of polymer using a single equation by applying the Cross-WLF or Bird-Carreau theory (Coogan and Kazmer, 2019; Le et al., 2021; Xia et al., 2018). However, this requires the determination of the zero-shear viscosity of the material, which is out of the scope of this study.

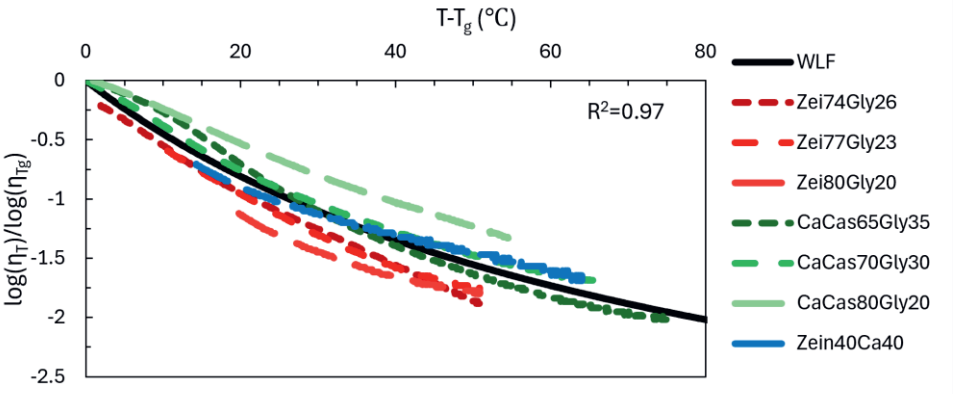


Fig. 2.6 *Temperature-dependent viscosity of different formulations of protein composites as described by a Williams–Landel–Ferry equation (Eq. 2): dashed and dotted lines represent experimental data and black line represented WLF fit*

2.4.3 3D printing of protein composites using pellet extrusion

In this study, protein composites were formulated to match the printability window of commonly used materials for FDM (e.g. PLA and ABS). Specifically, the T_g of zein composite with 12.5% glycerol was similar to that of PLA (58 °C), whereas T_g of CaCas composite containing 20% w/w glycerol was similar to that of ABS (108 °C) (Rowat et al., 2021). To demonstrate the feasibility of using protein composites as materials for FDM, we 3D printed several selected formulations with pellet-fed FDM printer at different printing conditions (see Table 1). The results show that by adjusting the printing speed (i.e. indirectly the shear rate of extrusion), cylinders with good shape fidelity were obtained. The highest shape fidelity was achieved

for a zein composite with 20% glycerol printed at 145 °C and 13 mm/s. CaCas-containing formulations required a higher printing temperature and printing speed to be printed successfully due to its increased viscosity as discussed before.

Table 2.1 Digital images of ring-shaped 3D-printed structures of plasticized proteins using fused deposition modelling and a pellet extruder as the printing nozzle.

Formulation	**Temperature (°C)**		**Printing speed (mm/s)**		
	Heating block	Build plate	13	17	29
Zein80 /Gly20	145	60			
Zein70 /CaCas10 /Gly20	145	70			
			34	41	57
Zein60 /CaCas20 /Gly20	165	70			

* The designed ring-shaped structure has an inner diameter of 14 mm. At a printing speed of 13 mm/s the screw speed equals 2 rpm

At the printing speed of 13 mm/s the shear rate in the nozzle equals 79 s^{-1} (Eq. 4). With the power law (fitting parameters in **Fig. 2.4**), the viscosity at this shear can be calculated at the strain sweep temperature. Utilizing the WLF

relation with the C_1 and C_2 values obtained (**Fig. 2.6**), and the viscosity obtained in the last step, the viscosity at 145 °C and shear rate of 79 s^{-1} can be calculated. Thus we find that the viscosity at the optimised printing settings equals 141 Pa·s, quite close to the viscosity target of 200 Pa·s (Spoerk et al., 2017).

Moreover, a structure with overhangs was successfully 3D-printed (**Fig. 2.7**) which has not been reported in previous work on printing of zein composite (Chaunier et al., 2020; Thadasack et al., 2023). A cone shape with a 45° slope outer wall was printed using zein-based composite. It is generally accepted that FDM plastics such as ABS and PETG can be printed with overhangs up to 45 degrees. The dimensions of the printed object were slightly different from the design at a wall thickness of 2.8 mm and a slope of 36-40° (**Fig. 2.7 a2**). Nevertheless, these results demonstrate the excellent potential of protein composites as feedstock for FDM.

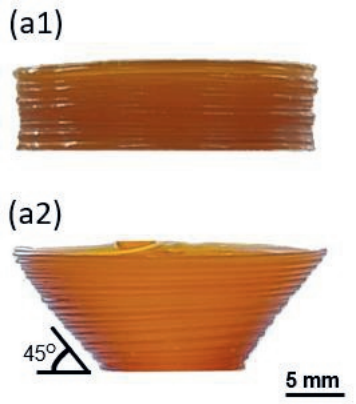


Fig. 2.7 *Photographs of FDM 3D printed structures. A1: hollow cylinder, 14 mm inner diameter, 5 mm height & 2.4 mm thick walls. A2: hollow cylinder with 45° overhang angle design, 100 mm height & 2.4 mm thick wall*

2.4.3.1 Estimation of shear rate and pressure drop

Equations 2.4 - 2.7 can be used to calculate the pressure drop over the nozzle. In the working range of 0-10 RPM (printing conditions in **Table 2.1**) the maximum achievable torque is 1.95 N·m according to the torque curve provided by the manufacturer, lower than the theoretical maximum of 2.7 N·m (**Eq. 2.7**). The maximum system pressure is therefore 0.23 MPa.

For the extrusion of Zein80/Gly20 at optimal printing speed of 13 mm/s (**Table 2.1**) at 145 °C the pressure drop is 0.11 MPa (full calculation in Supplementary Material). As this is lower than the maximum system pressure, the zein composite can be extruded with the desired flow rate. For a CaCas/Gly20 composite at a printing speed of 13 mm/s at 165 °C (higher temperatures induced browning) the pressure drop is 1.9 MPa, higher than the maximum system pressure. It was expected that this material would not extrude, which was confirmed experimentally as the motor would stall during FDM of this composite.

2.4.3.2 Isoviscosity diagram

An isoviscosity diagram summarizes our data for zein-based composites (**Fig. 2.8**). Measurement values for T_g and several viscosities are indicated with dashed lines. In summary, viscosity at T_g is too high for extrusion. With increasing temperature and reduction of solids content, we arrive at the isoviscosity line of η*=5000 Pa·s where extrusion is possible but adhesion and flowability are too poor for FDM. The Dahlquist criterion states that a materials G' should be <0.1 MPa to enable good contact with other surfaces, which could be another evaluation point. With further increase of temperature and reduction of solids content we arrive at the isoviscosity line of η* = 200 Pa·s which is ideal for FDM. Finally, at η* = 100 Pa·s the material becomes too liquid for FDM and no self-supporting structure can be created

after extrusion from the nozzle. This diagram can be transformed to account for shear-thinning effects at shear rates relevant to FDM by utilizing material-specific power-law fitting parameters. In summary, good printing performance of a composite can be adjusted by changing its formulation (e.g. type and concentration of protein and plasticizers) and processing conditions during FDM (e.g. print temperature and extrusion rate).

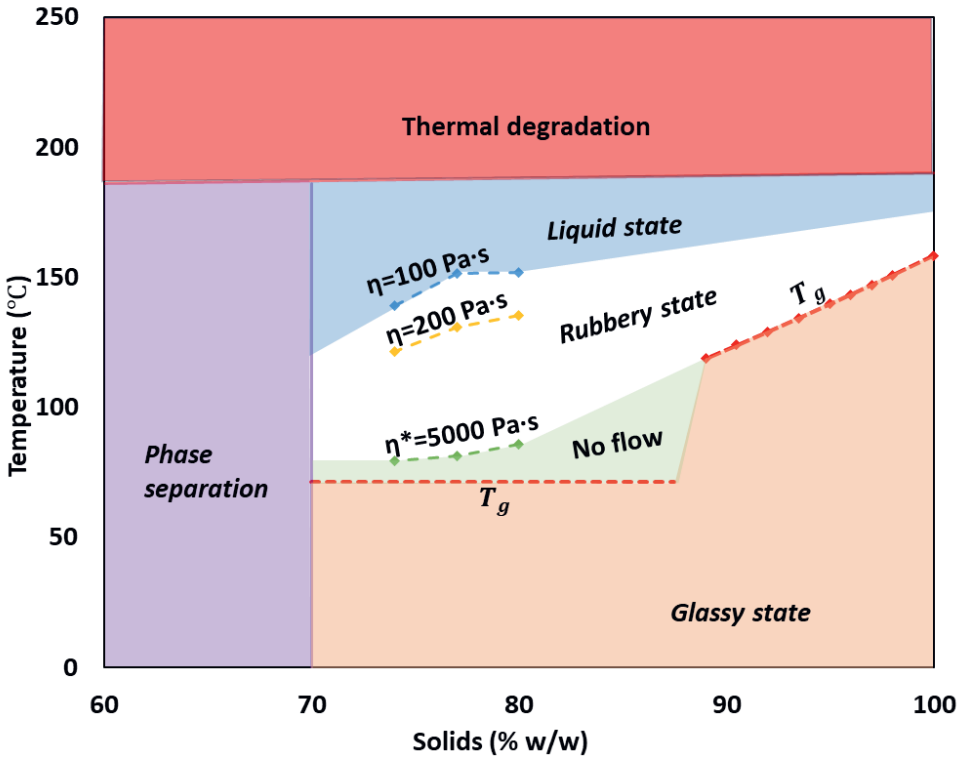


Fig. 2.8 *State diagram for zein-glycerol composites with iso-viscosity lines for the linear viscoelastic regime. Measurement data indicated with square markers.*

2.5 Conclusion

In this study, we successfully formulated protein-glycerol composites which showed similar thermal and rheological properties as conventional polymers used for FDM processes. The printability windows of materials was derived

from their thermorheological properties. Selected formulations were 3D printed using pellet-fed FDM printer, which showed good printability. Complex designs such as a 3D structure with 45 degree overhangs were realized. The development of protein-based composite materials extends the choice of materials for FDM. Such materials could potentially be used for 3D food printing and bioprinting for different applications. Future studies could focus on testing different types of proteins and plasticizers, and further exploring their applications. The pellet printing process could be further optimized by introducing a heated chamber to better control the temperature and thus printing performance of composite materials.

Appendix 2

A2.1 Thermogravimetric analysis

Method: (TGA) was performed using a STA 6000 (Perkin Elmer). Powder and pellet samples (10 ± 0.5 mg) were loaded into reusable cups that had been burned out using an open flame to remove any residue of prior measurements. Sample weight was recorded during heating from 30 to 400 °C at a heating rate of 10 °C/min to find the onset temperature of degradation. Air was used as purge gas at a rate of 30 ml/min and a pressure of 1.8 bar. STA 6000 was calibrated using an indium standard. Degradation onset temperatures were determined as the temperature at which mass degradation started to occur rapidly after full evaporation of solvent.

Results: TGA of zein and CaCas without plasticizer shows two distinct thermal events. After addition of plasticizer an additional thermal event at a temperature between those first two is observed. The first thermal event can be related to the evaporation of solvent from 30 to 130-150 °C.

When comparing zein powder with zein pellet a mass loss of 7 versus 15% is found respectively, indicating that approximately 8% of ethanol is still bound by zein in the pellet after solvent evaporation at room temperature was completed. The middle thermal event is related to thermal degradation and its onset temperature is reduced by glycerol (**Fig. A2.1**). For zein pellet without glycerol we found onset of rapid mass loss at 206 °C which closely matches observations of Selling (2010), who reported onset of rapid mass loss at 225 °C for zein powder. By plotting the derivative of the mass loss we find that the highest rate of mass loss occurs around 320 °C (**Fig. A2.2**), which matches the observations of Selling. When adding 20 or 30% w/w of glycerol we find that the onset temperature of rapid mass loss is reduced to 151 and 141 °C,

respectively. This matches our observations of material blackening during pellet extrusion at similar temperatures.

The middle thermal event for CaCas plasticized with 30% glycerol has an onset temperature of 175 °C, again closely matching the observation of burned extrudate during extrusion processing at 180 °C.

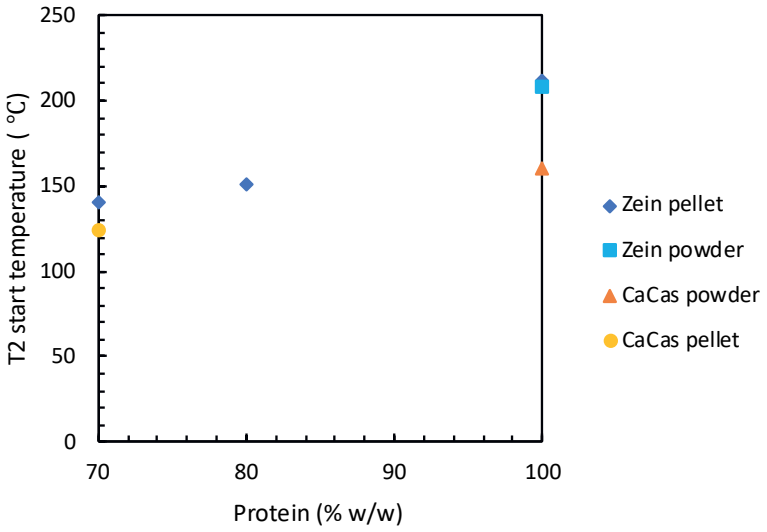


Fig. A2.1 *Degradation onset temperature (End of interval 1, T1) as function of protein content*

Table A2.1 *Data summary of TGA*

Powder/ pellet	Protein	Protein %	End of interval 1, T1 (°C)	Onset T, T2o (°C)	Onset weight (%)
powder	CaCas	100	160	263	91
pellet	CaCas	70	124	175	85
powder	zein	100	208	269	93
pellet	zein	100	206	278	85
pellet	zein	80	151	210	82
pellet	zein	70	141	203	85

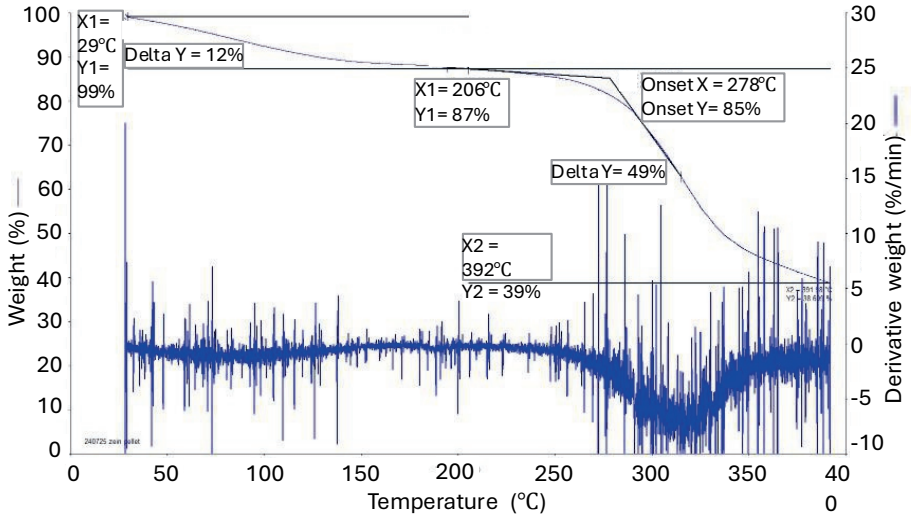


Fig. A2.2 *TGA result for zein pellet. Top graph: mass loss versus temperature. Bottom graph: derivative of mass loss.*

A2.2 Rheology

Method: The strain constant K_γ of the CCR's cone geometry is dependent on the cone angle β for the RPA die: $K_\gamma = \frac{1}{\beta} = \frac{1}{0.125 \text{ radians}}$. Strain is a measure of deformation representing the angular displacement relative to a reference length: $\gamma = \delta \cdot K_\gamma$ with γ the strain (-) and δ the angular displacement (radians). A displacement of the die by $\delta = 1° \approx 0.0175$ rad is therefore equal to a strain of $\gamma = 1/0.125 \cdot 0.0175 = 0.14 = 14\%$. Furthermore, the stress constant K_σ is dependent on the cone radius R according to $K_\sigma = \frac{3}{2\pi R^3}$. Filling in R = 20.626 mm we find that K_σ = 54400 m^{-3}. Thus, a torque of 1 N·m equals a shear stress σ of 54.4 kPa. The resistance to deformation of the measured material is called the complex modulus G*, which is equal to the shear stress divided by the strain. Finally, from the oscillatory measurements complex viscosity can be calculated as $\eta^* = G^*/\omega$ with ω the frequency (in rad/sec). All the calculations are automatically performed by the SQS-Process

software (TA instruments) which is also used to operate the CCR. We assume the Cox-Merz and Rutgers Delaware rules are applicable to our materials, and these results can be translated to (dynamic) shear viscosity:
given by:

$$|\eta^*(\omega)| \cong \eta(\dot{\gamma})|_{\omega=\dot{\gamma}} \qquad \textit{Eq. A 2.1}$$

With η* the complex viscosity and η the steady shear viscosity at equal values of angular frequency ω and shear rate $\dot{\gamma}$ (Cox and Merz, 1958). Finally, according to Newton's law $\sigma = \eta \cdot \dot{\gamma}$ with η the dynamic viscosity in Pa·s and $\dot{\gamma}$ the shear rate in s^{-1}.

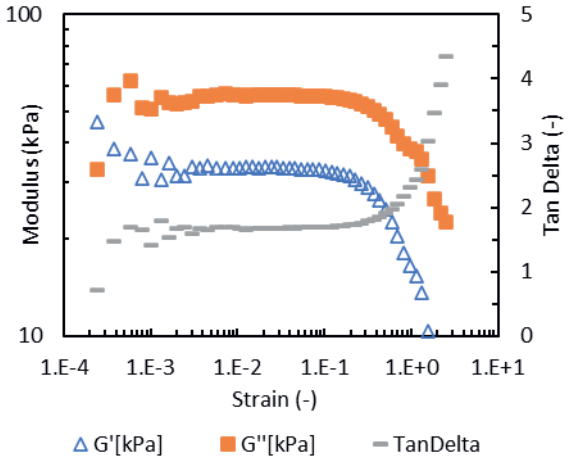


Fig. A2.3 *CCR strain sweep of zein plasticized with 26% glycerol*

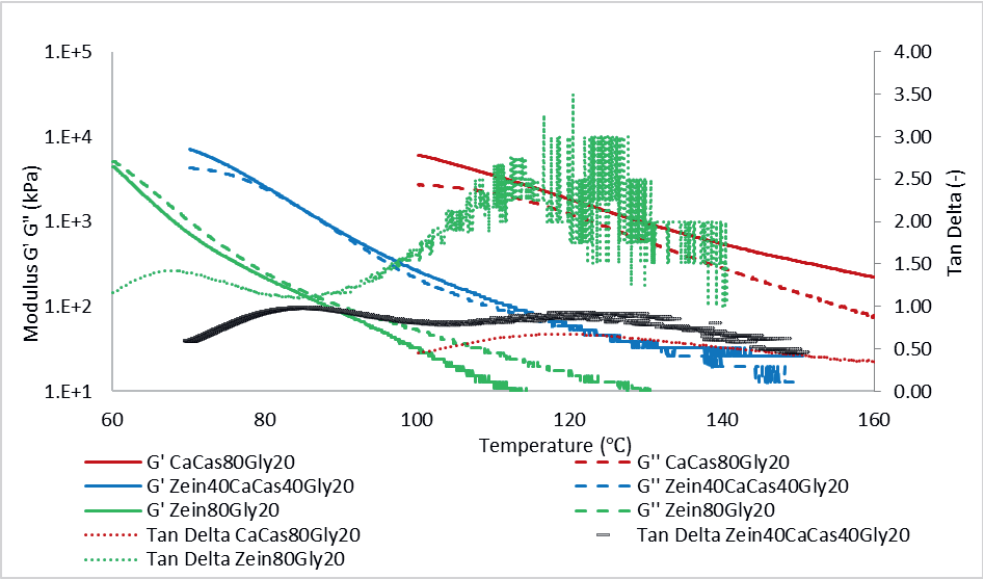


Fig. A2.4 *G', G" and tan delta as function of temperature for composites plasticised with 20% glycerol*

Table A2.2 *Fitting range power law*

Protein	Wpl (-)	Lower bound fit (s^{-1})	Upper bound fit (s^{-1})
Zein	74	6.2	43
	77	3.8	81
	80	2.4	10
	83	3.9	70
	86	43	81
CaCas	65	22	80
	70	22	80
	80	1.5	80

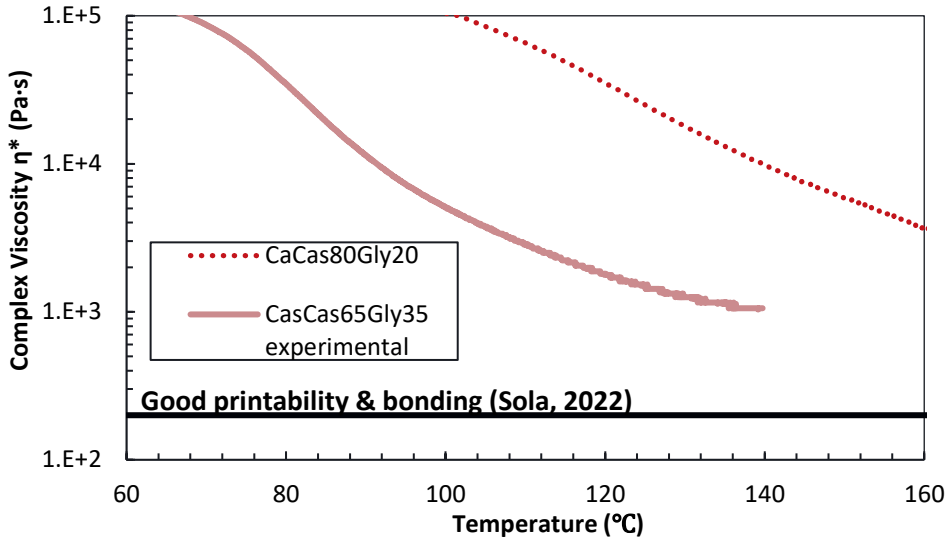


Fig. A2.5 *Complex viscosity of CaCas plasticised with 20% or 35% w/w (maximum) glycerol as function of temperature*

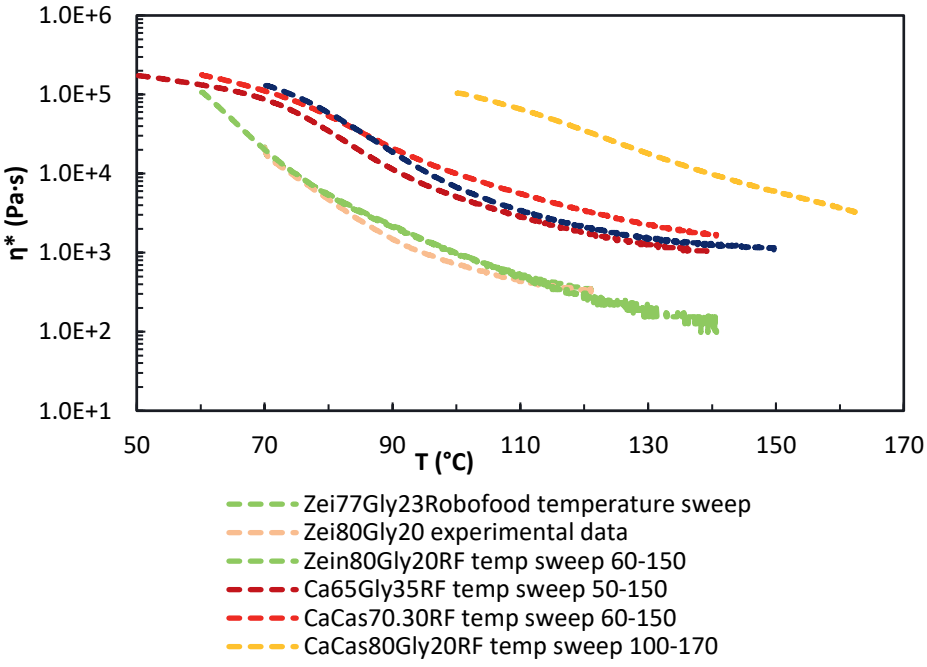
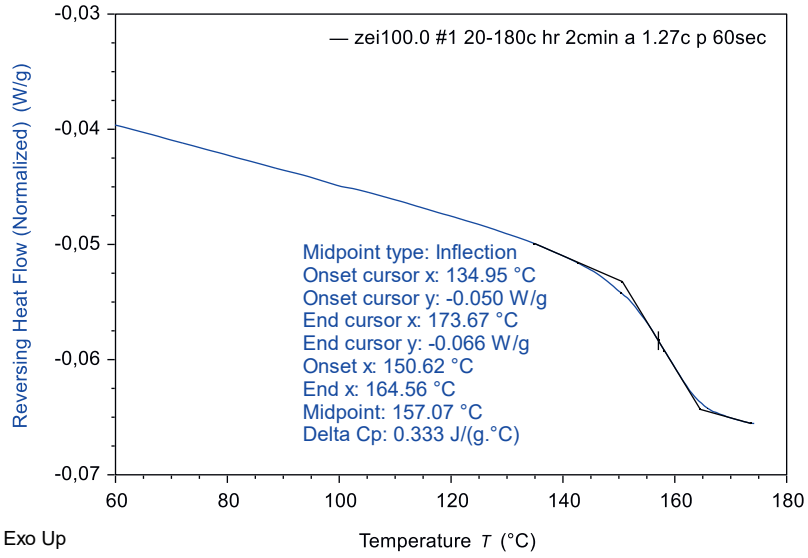
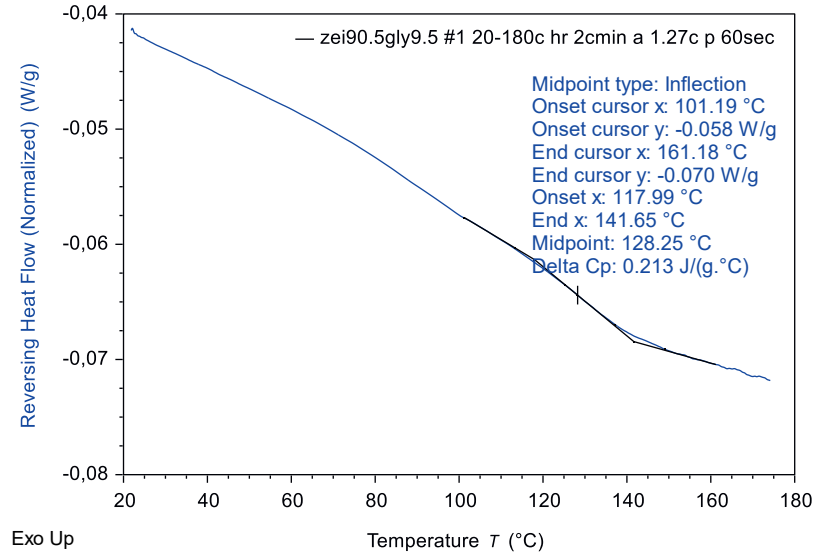


Fig. A2.6 *Complex viscosity as function of temperature for different composites*

Table A2.3 *Slicer profiles*

Print temperature (°C)	135-155
Build plate temperature (°C)	60-70
Part cooling fan speed (%)	100
Minimum layer time (s)	0-15
Linear flow rate (mm/s)	13-60
Steps/mm	147
Extrusion multiplier (%)	350
Screw speed (RPM)	13.4 @ 30 mm/s LFR
Layer height	50% of nozzle bore width





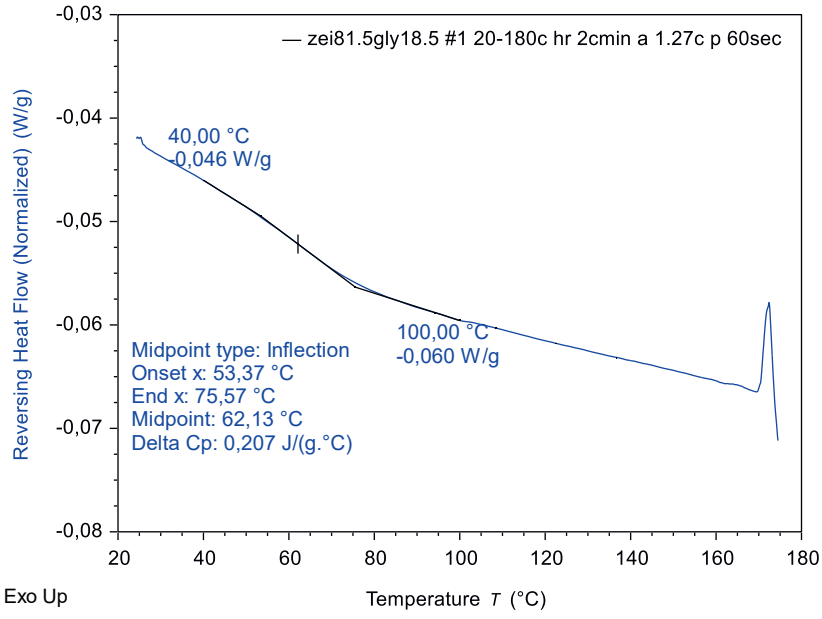


Fig. A2.7 *Modulated DSC thermographs for 100/0, 90.5/9.5 & 81.5/18.5 mixtures of zein/glycerol. Glass transition analysis performed in TRIOS software*

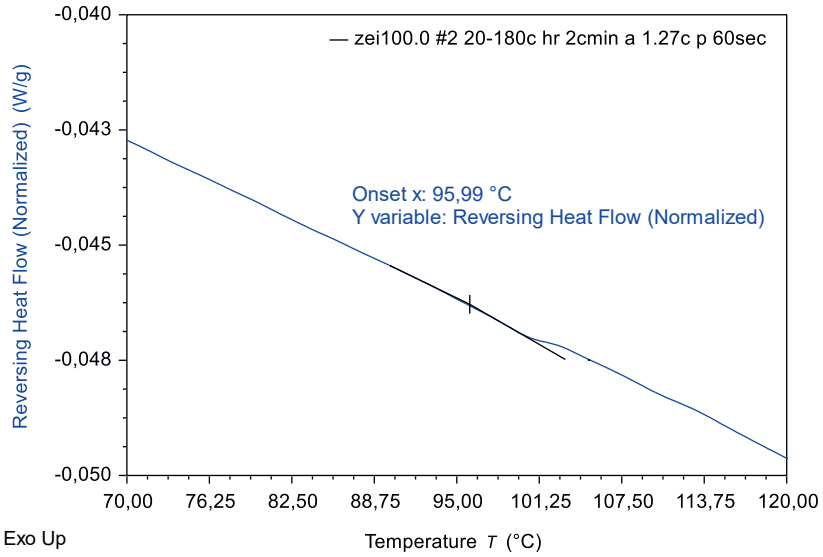


Fig. A 2.8 *Modulated DSC thermograph for pure zein, showing a small transition for alpha-zein.*

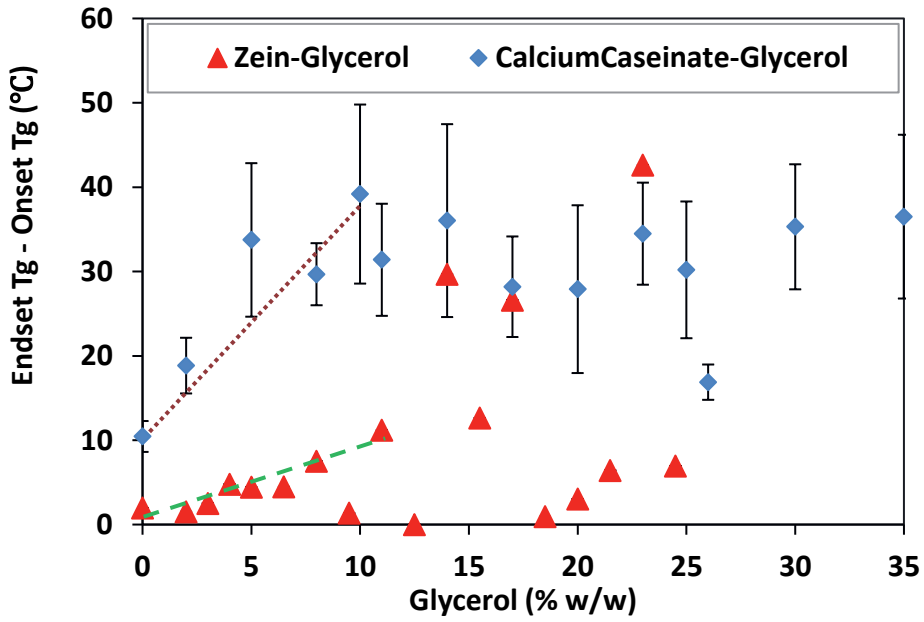


Fig. A2.9 *Width of glass transition peak calculated as endset minus onset temperature, plotted as function of plasticizer concentration. Peak width increases with plasticizer concentration as indicated by dotted line (calcium caseinate) and striped line (zein-glycerol)*

A2.3 Calculations pressure drop

Radii of the drive gear and screw are 0.014 and 0.005m respectively. Nozzle radius is 0.0004m.

Pressure drop zein80/glycerol20 at 145 °C, low shear

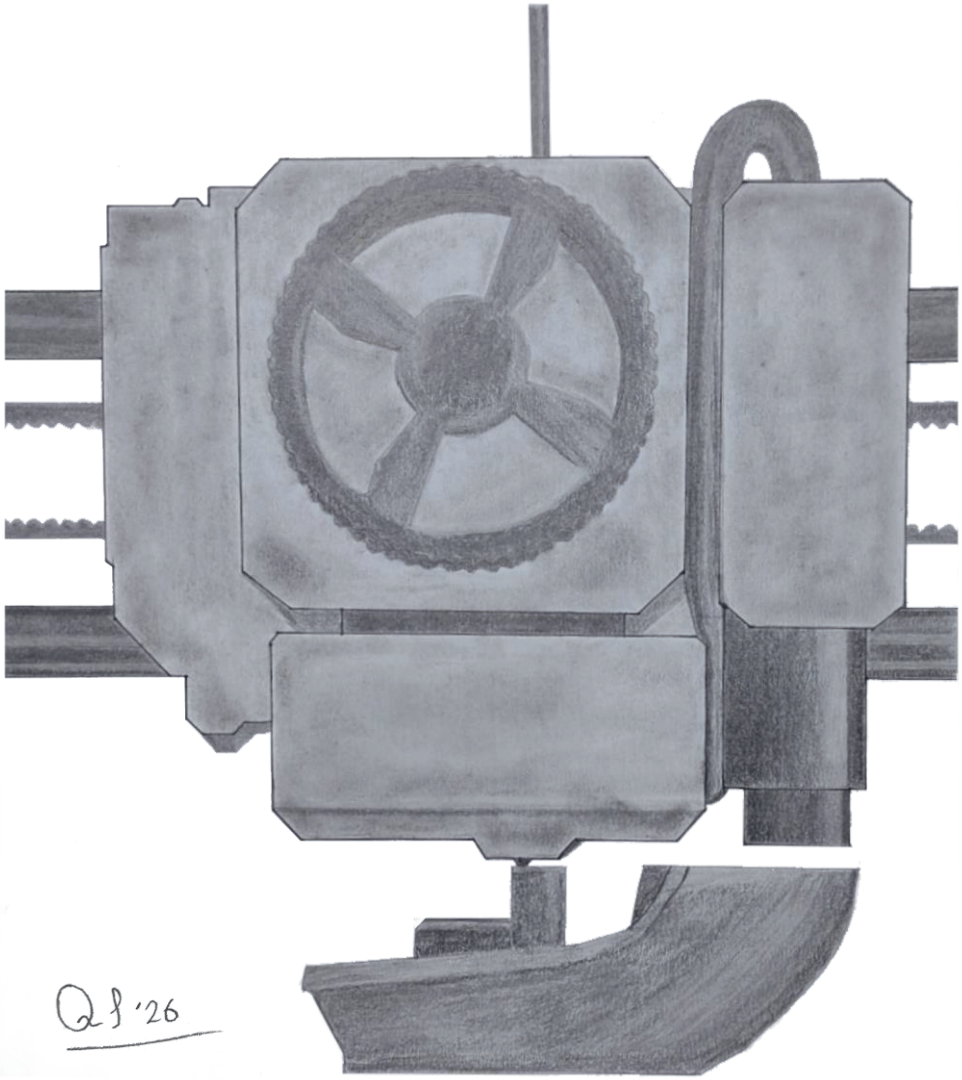
$$\Delta P = \frac{8\eta LQ}{\pi R^4} = \frac{8 \cdot 200\ Pa{\cdot}s \cdot 0.0016\ m \cdot 3.3{\cdot}10^{-9}\ m^3/s}{\pi \cdot (0.0004\ m)^4} = 0.11\ \text{MPa}$$

Pressure drop cacas80/glycerol20 at 160 °C, low shear

$$\Delta P = \frac{8\eta LQ}{\pi R^4} = \frac{8 \cdot 3600\ Pa{\cdot}s \cdot 0.0016\ m \cdot 3.3{\cdot}10^{-9}\ m^3/s}{\pi \cdot (0.0004\ m)^4} = 1.89\ \text{MPa}$$

Maximum system pressure

$\Delta P = \frac{F}{A}$ and $F = \frac{T\ G}{r}$, therefore: $\Delta P = \frac{T \cdot G}{A \cdot r} = \frac{1.95\ N{\cdot}m}{\pi{\cdot}0.014^2 \cdot 0.014\ m} = 0.23\ \text{MPa}$


Q1 '26

Chapter 3

Zein-based Edible Filament: Formulation Development, Fabrication and Fused Deposition Modelling Performance

This chapter has been submitted as Steffens, Q., Te Koppele, L,. Van der Sman, R.G.M., Boom, R. M., Zhang, L. (2026). Zein-based Edible Filament: Formulation Development, Fabrication and Fused Deposition Modelling Performance

Abstract

Fused deposition modelling (FDM), also known as fused filament fabrication, is a popular 3D printing technique that utilizes thermoplastic filaments to fabricate physical objects from digital models. The development of edible biopolymer-based filaments could enable new sustainable applications of FDM. However, development of edible filaments is currently limited by issues such as brittleness and phase separation. In this study, a thermoplastic zein filament was developed for use as feedstock in fused deposition modelling (FDM) systems. Phase compatibility and filament flexibility were optimized through selection of plasticizer blends consisting of glycerol and fatty acids, guided by thermal and rheological analyses. Rheology of the zein-based composites was governed by the glass transition temperature, independent of the specific plasticizer(s) utilized. Oleic acid and glycerol worked synergistically to depress the glass transition temperature, increasing filament flexibility while maintaining phase stability. Edible zein filaments were successfully produced using a compounding device, and upscaling of the production was achieved by using a pilot-scale continuous extruder, demonstrating the feasibility of industrial production. These filaments were used to 3D print standardized dog-bone shaped specimens for mechanical testing. The tensile and flexural strengths and moduli of the edible specimens equalled 13-28% of those of PLA references. In addition, complex geometries were printed using a consumer-grade FDM printer, demonstrating successful FDM printing of fully edible filaments for the first time. This work demonstrates a pathway to formulate and produce edible, thermoplastic filaments that could be used to drive innovation in FDM of foods, pharmaceutical devices and transient robots.

Abbreviations

FDM	Fused Deposition Modelling
G	Glycerol
HA	Hexanoic acid (6:0, $C_6H_{12}O_2$)
SA	Stearic acid (18:0, $C_{18}H_{36}O_2$)
OA	Oleic acid (18:1 Δ9c, $C_{18}H_{34}O_2$)
LA	Lauric acid (12:0, $C_{12}H_{24}O_2$)
FA(s)	Fatty acid(s)
OA/G	Blend of oleic acid and glycerol
mDSC	modulated Differential Scanning Calorimetry
CCR	Closed Cavity Rheometer
UTM	Universal Testing Machine
C*	Critical Strain
T_g	Glass transition temperature [°C]
G'	Storage modulus [Pa]
G"	Loss modulus [Pa]
YM	Young's Modulus [Pa]

3.1 Introduction

Fused deposition modelling (FDM) is an additive manufacturing technique. During FDM, a thermoplastic feedstock is heated, extruded through a nozzle, and deposited layer by layer to fabricate three-dimensional objects from digital models. FDM reduces the marginal cost of fabrication and design iterations, enabling rapid prototyping and production of complex single components without tooling (Dey et al., 2021; Wallin et al., 2018). To 3D print food materials, however, extrusion-based printing is commonly used. Nevertheless, one advantage of food printing using FDM over extrusion-based printing is that no post-processing is required, such as baking, thereby eliminating the risk of deformation of the printed geometry. Therefore, it is of interest to formulate and develop filaments made of food materials for FDM processes.

Thermoplastic protein-based composites are suitable for FDM. Previously, zein was combined with plasticizers (i.e. glycerol) to create composites which can be used as feedstock for FDM (Chaunier et al., 2018). In another work, a pellet-based FDM process was achieved by using zein-glycerol composites (Steffens et al., 2025), to create 3D edible structures. Zein is suitable for this process due to the thermal-rheological behaviour of its viscous polymer melt as well as its sintering ability, which allows for welding between already printed layers and hot material flowing out of the nozzle (Chaunier et al., 2019). The FDM process of zein composites is therefore similar to the FDM process of commonly used plastic polymers, such as ABS and PLA (Chaunier et al., 2019; Das et al., 2021). Furthermore, these protein-based composite materials are interesting because the 3D structures that can be created with them can potentially serve as scaffolding for cell growth, as drug carrier or as a means to create anisotropic structures for texturizing food products such as

meat replacers (Bouman et al., 2015; Mattice and Marangoni, 2020; Tavares-Negrete et al., 2020).

Although pellet-based FDM printing of zein composite has been proven feasible, feedstock in the form of filaments is preferred over pellets. Developing edible filaments that are compatible with commercial 3D printers could allow wider adoption of thermoplastic protein composites in FDM. Additional advantages of filament-based printing over pellet-based printing include improved control of the extrusion rate, reduced toolhead mass, and the possibility to benefit from other technological developments in filament FDM printers such as multi-material printing (Das et al., 2021).

To date, FDM 3D printing of fully edible filaments based on protein has not yet been reported in literature. For a filament to be compatible with standardized FDM printers, its thermal, rheological and mechanical properties need to conform to specific constraints. During filament production, extrudability and spoolability are important challenges (Sola, 2022). Extrudability is defined as the ability to produce a filament of the correct diameter over sufficient length, such that it can be reliably pinched by the feeding mechanism on a FDM printer throughout the printing process. Spoolability refers to the ability of a material to be wound on a reel after extrusion immediately after its diameter has been stabilized through a cooling process. Extrusion processing of protein-based materials has been explored for manufacture of packaging films, which has some similarities with filament extrusion (Eslami et al., 2023; Permadi et al., 2024; Rusli, 2017; Wang et al., 2025). To reduce the brittleness of the extruded material, plasticizers are added to reduce the amount of intra- and intermolecular hydrogen bonds between the polymer chains, leading to greater flexibility (Pommet et al., 2003). This is reflected by a reduction in the glass transition

temperature (T_g) of the extrudate, which is often characterized by differential scanning calorimetry (DSC). A reduction in T_g lowers the required processing temperature and increases the material's flexibility. Finally, changes in composition affect T_g values, which influence the mechanical properties of the material. For example, adding plasticizers increases the strain at break but reduces the maximum tensile stress and stiffness in PLA (Jacobsen and Fritz, 1999).

The type of plasticizer used affects the material properties of protein composites. Most often, hydrophilic compounds are used to plasticize proteins. However, phase separation is a commonly observed issue when larger quantities of plasticizer are utilized when producing a composite material (Chen et al., 2020; Xu et al., 2012). Phase separation in protein-based packaging films can sometimes be resolved through addition of amphiphilic plasticizers, such as fatty acids (Pommet et al., 2003). In zein films, addition of stearic or lauric acid increased its thermal stability, water vapor barrier properties and mechanical properties (Wang et al., 2025). In addition, improvements in mechanical properties of zein films were reported when oleic acid and glycerol were combined as plasticizers, such as higher tensile strength (Xu et al., 2012). Thus, it is hypothesized that edible composite filaments with ideal material properties can be developed by combining glycerol and fatty acids to plasticize zein.

Therefore, the objective of this study was to develop a thermoplastic zein filament by investigating the effects of composition and to demonstrate its 3D printing performance using standard commercial FDM equipment. During formulation development, zein was plasticized with glycerol and fatty acids differing in hydrocarbon chain length as well as degree of saturation, as well as combinations thereof. The efficiency of different plasticizers in these

composite formulations was investigated through determination of the glass and melt transitions using modulated differential scanning calorimetry (mDSC), as well as the determination of viscoelastic properties above the glass transition temperatures (T_g) using a closed-cavity rheometer (CCR). The phase compatibility of the different plasticizers with zein was studied using nuclear magnetic resonance (NMR). The extrudability and spoolability of composites was investigated by filament fabrication using a lab scale compounder. The insights were then used to select one composite formulation for continuous production on a twin-screw extruder and demonstrate the feasibility of industrial upscaling. The filament was subsequently used as feedstock for a commercially available FDM printer without hardware modifications. Dog-bone shaped specimens with dimensions defined by ISO-standards were printed with our edible filament and compared with PLA and PETG references. More complex 3D shapes like spiral springs and the 3D benchy were 3D printed to demonstrate the potential of our edible filament. This work contributes to the further advancement of food and bio-printing by exploring 3D printing of edible filament.

3.2 Materials and Methods

3.2.1 Materials

Zein (Z3625), hexanoic acid (W255900), oleic acid (W281506), stearic acid (W303518) and lauric acid (W261408) were purchased from Sigma-Aldrich (Zwijndrecht, The Netherlands). Glycerol (purity 99.6%) and ethanol (purity 96%) were obtained from VWR Chemicals (The Netherlands).

3.2.2 Formulation development and analysis

During formulation development, insights on material behaviour during filament fabrication and 3D printing were obtained using rheological, thermal and mechanical analysis methods (Fig. 3.1).

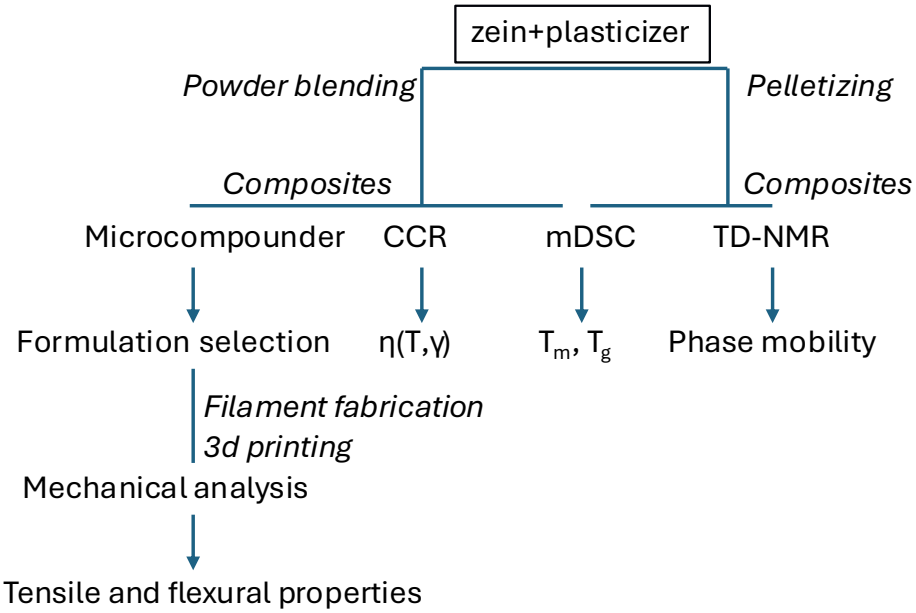


Fig. 3.1 Overview of experimental methods used during formulation development, filament production and assessment of 3D printed objects

3.2.2.1 Zein-plasticizer powder samples

Zein powder was mixed with individual plasticizers at 10, 20, or 30% (w/w) relative to zein. The plasticizers used were glycerol (G), oleic acid (OA), stearic acid (SA), lauric acid (LA), and hexanoic acid (HA). In addition, blends of OA and G were incorporated at total concentrations of 20 or 30% (w/w), using OA:G mass ratios of 3:1, 1:1, or 1:3. Samples were mixed using a spice grinder (Waring Commercial, USA), transferred to containers and rotated overnight on a roller bank at 50 rpm to ensure homogeneity. The zein-plasticizer powder samples were used for mDSC analysis and compounding experiments.

3.2.2.2 Zein-plasticizer pellet samples

Zein-plasticizer composites can also be prepared as pellets. Pellets were prepared by dissolving zein and plasticizer(s) in 2.5 times of their weight of 96% ethanol at 65 °C under continuous stirring at 500 RPM for 2 hours.

Samples containing stearic acid were heated to 70 °C to ensure complete melting of the fatty acid. The resulting solutions were poured onto rimmed silicone sheets, yielding 1-2 mm thick films which were dried at ambient temperature in a fume hood for 96 hours. These zein films were subsequently ground using a spice grinder (Waring Commercial) and passed through a 3 mm mesh sieve to obtain the pellets. Pellets were stored in airtight containers until further analysis by mDSC and NMR.

3.2.2.3 Determining glass transition temperature

The glass transition temperatures of zein-plasticizer composites were determined by modulated Differential Scanning Calorimetry (mDSC) on a DSC250 (TA Instruments, USA). Samples (8.00 ± 0.1 mg) were sealed in non-hermetic aluminium pans prior to analysis. The thermal analysis profile consisted of an initial heating cycle from 20 °C up to 180 °C at 15 °C/min to evaporate any free moisture in the samples and subsequent equilibration at 20 °C. Temperature modulation was then applied with an amplitude of 1.27 °C and a period of 60 seconds. During a second heating cycle the temperature was increased to 180 °C at a rate of 2 °C/min. Above these temperatures rapid thermal degradation of zein occurs (Arrieta et al., 2013; Selling, 2010; Steffens et al., 2025).

The melting point of fatty acids in zein-plasticizer composites was determined as the peak temperature of the melting peak of the thermogram, using the data obtained during the first heating cycle. The exact temperature was calculated using the peak integration (enthalpy) function of TRIOS software (v5.6.0.87, TA instruments).

The glass transition temperature of composites was determined as the inflection point of the shifted part of the thermograph (i.e. a shift in the baseline of the reversing heat flow signal), using the data obtained during the second heating cycle. The exact inflection temperature was calculated using

the glass transition analysis function of TRIOS software (v5.6.0.87, TA instruments), by selecting an analysis range of ± 30 °C around the visually apparent T_g in the thermograph. The T_g of each sample was plotted against the molar ratio of plasticizer and zein. The molar ratio was calculated based on the molecular weight and mass ratio of zein and plasticizers. Commercial corn zein consists of 75-80% α-zein, with smaller fractions of β-, γ- and δ-zein. Literature reports average molecular weights of α-zein of 20-25 kDa, with a weighted average of all zein monomers of 23 kDa. Molecular weights of glycerol, HA, LA, OA, SA were 92.09, 116.16, 200.32, 282.46 and 284.48 g/mol, respectively (Lide, 2006).

3.2.2.4 Temperature-dependent viscosity

Rheological properties of the zein-plasticizer composites were analysed with a Closed Cavity Rheometer (CCR) (RPA Elite, TA instruments). For each measurement, a 4.15 ± 0.05g aliquot of pellets was placed between two layers of polyester film and positioned in the CCR's cavity. The chamber was sealed at a pressure of 4 bar to prevent loss of water vapour during measurement.

The linear viscoelastic regime (LVR) was determined using strain sweeps at a frequency of 10 Hz and temperature of 110 °C. Samples were equilibrated at the measurement temperature for 2 minutes before the measurement started. During the measurement, strain was increased from 0.01 to 130%. Storage modulus (G'), loss (G") modulus and viscosity were measured as function of strain. The end of the linear viscoelastic regime (critical strain, C^*) was calculated as the lowest strain where the G' had decreased 5% below the plateau value.

Temperature sweeps were performed at the lowest critical strain measured amongst all samples, at a frequency of 10 Hz. Samples were heated from a

temperature 25 °C below their T_g up to 180 °C at a heating rate of 5 °C/min while recording changes in G', G" and viscosity.

3.2.2.5 Molecular mobility

The molecular mobility was used as an indicator of plasticization and phase separation. The molecular mobility was investigated by comparing shifts in T_2-peaks of pelletized zein-plasticizer composites identified using Time Domain NMR. TD-NMR measurements were performed using a minispec mq benchtop NMR spectrometer (Bruker, Germany) at a 20 MHz operating frequency. For liquid samples (e.g. glycerol or fatty acids), an FID-CPMG pulse sequence was employed, consisting of a free induction decay (FID) time of 0.1 ms and a Carr-Purcell-Meiboom-Gill (CPMG) pulse train with an echo time of 0.2 ms, comprising 8000 data points. Sixteen scans were recorded with a recycle delay of 8 s. Each CPMG dataset was reduced to 2000 geometrically spaced data points prior to fitting the CPMG decay curves using the CONTIN algorithm.

For dry samples, the FID-CPMG sequence was used, with an FID time of 0.1 ms and a CPMG pulse train with an echo time of 0.2 ms, comprising 1000 data points. Sixteen scans were recorded with a recycle delay of 8 s. CPMG decay curves were fitted using CONTIN. All data were corrected for background signal using a measurement on an empty sample tube.

3.2.2.6 Batch-wise extrusion

The feasibility of filament formation was investigated by extruding zein-plasticizer composites using a Xplore MC40 microcompounder (Xplore Instruments, Netherlands). The mixing chamber of the microcompounder has three heating zones, with the temperatures along the screw direction having been set to T_g + 45-55 °C for the first heating zone, T_g + 50-60 °C for the middle heating zone and T_g + 45-55 °C for the last heating zone. These

temperature settings ensured homogenous melting and mixing of the material. It is noteworthy that the T_g depends on the formulation. At the end of the heating zones, the material can be extruded through a die, or can flow through a backflow channel while the die is closed off. A schematic overview can be found in the 'Microcompounder' section of **Appendix 3**.

The melt compounding process was started by feeding the powder sample (18 ± 1.0 g) into to the extruder barrel and circulating the material at 100 rpm for at least 3 minutes. The materials in the formulation are mixed by the shear stresses exerted by the extruder. Once a constant torque was reported by the inline measurement system, a homogeneous viscosity and melt were obtained. The screw speed was lowered to 20 rpm and the outlet die (⌀ = 1.5 mm) was opened. After extrusion through the die, the filaments were cooled by air on a Cast Film Pro line (Xplore Instruments, Netherlands). Filaments with sufficient flexibility were wound on a spool (⌀ = 85 mm) at the end of the cooling line. The winding speed was continuously adjusted to optimise the stretching force which determines the final diameter of the filament.

The microcompounder operates as a batch process, so once the die opens and recirculation flow stops, the extrusion barrel gradually runs empty. The back pressure at the die therefore reduces as the filament is being extruded. As die swell is influenced by the pressure drop between the inside and outside of the die, this makes it very challenging to obtain a consistent diameter over the full length of the extrudate in batch processing (Rauwendaal, 2014).

3.2.3 Filament production and characterization

3.2.3.1 Production of filament using continuous extrusion

Based on the results at the formulation development stage, one composite formulation (OA7.5/G22.5) was selected for filament production using a

twin-screw extruder (ZSE 18, Leistritz AG, Germany). Zein powder, glycerol and fatty acid were fed separately into the extruder via dedicated powder and liquid dosing pumps. The modular screw configuration included kneading zones positioned downstream of the glycerol and fatty acid feeding points to ensure homogenization. Details on the screw configuration can be found in the Supplementary Material in Section 'Screw configuration continuous extrusion'. Feed rates were adjusted to achieve a throughput of 1.5 kg filament/h. The extrudate was discharged through a circular die (⌀ = 2.5 mm), passed through a water bath for 20 cm for initial cooling and subsequently guided by rollers along a 3 m passive air-cooling section towards a filament winder. Approximately 30 cm upstream of the winder, the filament diameter was monitored using digital callipers. The winder speed was adjusted to increase or decrease pulling force on the filament to maintain the desired filament diameter of 1.75 ± 0.1 mm.

3.2.3.2 Visual observation of filament under microscope

An optical microscope was used to assess the filament homogeneity and phase separation. Cross-sectional images of the filaments were captured with a 35x magnification objective using Z-stack acquisition. Images were processed using SmartZoom 5 software (ZEISS, Germany).

3.2.3.3 Density analysis of filament

The density of the filament samples was determined using a gas pycnometer (Ultrapyc 5000, Anton Paar, Austria), which measures sample volume based on Boyle's law ($P_1V_1 = P_2V_2$). The instrument was calibrated prior to use according to the manufacturer's instructions. After loading the sample into the measurement chamber, the system temperature was allowed to stabilize at 20 ± 0.02 °C. A one-minute purge with nitrogen gas was applied to prepare the sample for measurement. Analyses were conducted using nitrogen as the

displacement gas at a target pressure of 20 ± 0.004 psi. Measurement values were recorded once the difference between consecutive determinations was less than 0.005%. Each sample was measured in quintuplicate, and the mean density value was reported.

3.2.4 3D printing and mechanical testing

3.2.4.1 3D printing

Standardized dog-bone shaped specimens (ISO 527-2 Type 1BA geometry, see **Fig. 3.2A and B**) for mechanical testing were 3D printed from zein-based filament as well as commercial PLA and PETG filaments. Fused deposition modelling printers equipped with 0.8 mm nozzles were used, specifically a Sovol SV06 printer (Sovol 3D, China) for zein-plasticizer composite filament, and a Bambulab P1S printer (BambuLab, China) for PLA and PETG.

Digital models for 3D printing were designed using Solidworks 2024 (Dassault Systèmes, France). The models were sliced into gcode (a set of instructions containing the toolpath and other information for 3D printers) using OrcaSlicer v2.3.0 (OrcaSlicer.com). Filament print settings were manually calibrated using OrcaSlicer's build-in calibration tools, in the following order: temperature, extrusion multiplier and maximum volumetric flow rate. Results of this calibration and detailed printing parameters are provided in the 'FDM print settings' section of the Supplementary Materials.

The thickness and width of the 3D printed dog-bone shaped specimens were measured at the start, middle and end of the rectangular section using a digital calliper (500-161-30 CD-15AX, Mitutoyo Manufacturing Co. Tld., Japan). The average width and thickness were used to calculate the initial cross-sectional area per sample. The samples were conditioned at 50% RH and 20 °C for at least 7 days prior to testing of tensile and flexural properties.

In addition to the dog-bone shaped samples, 3D structures with more complex designs (spiral spring and 3D benchy, **Fig. 3.9**) were printed to demonstrate the potential applications of the zein filament developed in this study in FDM. Compared to the dog-bone shape, FDM of the spiral spring represents a greater challenge in layer stacking and required several design iterations to optimize the balance between spring shape and ability to store elastic energy by winding: lines had to be sufficiently thick to allow elastic energy storage, but not so thick that the flexibility of the spiral is lost. The 3D benchy is the most popular FDM calibration model, and can be used to assess overhang quality, bridging quality and retraction.

3.2.4.2 Tensile properties

A universal testing machine (UTM) (68TM-5, Instron, Massachusetts, USA) equipped with a 2000 N load cell was used for all testing. A non-contact extensometer was used to determine the strain from the actual deformation of the specimen gauge length. Circular markers (⌀ = 3 mm) were airbrushed onto the specimen surface using acrylic-polyurethane primer (Vallejo Surface Primer 700600, Vallejo, Spain) using a custom template to ensure a center-to-center marker spacing of 25 mm.

Young's modulus, fracture strain and fracture stress in the direction parallel to the FDM printing orientation were obtained by performing uniaxial tensile tests according to the ISO 527-2:2019 protocol. The UTM was equipped with pneumatic grips (2 kN, 2712-042) with integrated control valves to maintain a constant pressure of 6 bars during testing. Dog-bone shaped specimens were clamped in the UTM with an initial clamp distance of 60 mm and a preload of 0.05 N was applied. Strain was measured using an AVE-2 digital extensometer. A uniaxial tensile test was performed with a testing speed of 4% strain/min until fracture occurred.

Force-displacement curves were recorded with Bluehill Universal software (Instron, Massachusetts, USA). The true stress σ_{True} was calculated as

$$\sigma_{True} = \frac{F(t)}{A(t)} \quad \text{Eq. 3.1}$$

With *F(t)* the force (n) and *A(t)* the instantaneous cross-sectional area (m^2). The cross-sectional area depends on the instantaneous elongation and is given by

$$A(t) = \frac{h_0}{h(t)} A_0 \quad \text{Eq. 3.2}$$

With h_0 the initial gauge length (m), *h(t)* the instantaneous gauge length (m) and A_0 the initial cross-sectional area of the sample (m^2). The true strain ε_{True} (-) was calculated as

$$\varepsilon_{True} = \ln\left(\frac{h(t)}{h_0}\right) \quad \text{Eq. 3.3}$$

Young's modulus was calculated as the slope of the stress-strain curve in the linear elastic region between 0.05 and 0.5% of strain. The fracture strain and stress were determined at the peak stress of the true strain-stress curve. It was assumed that the volume of the sample remained constant during the measurement.

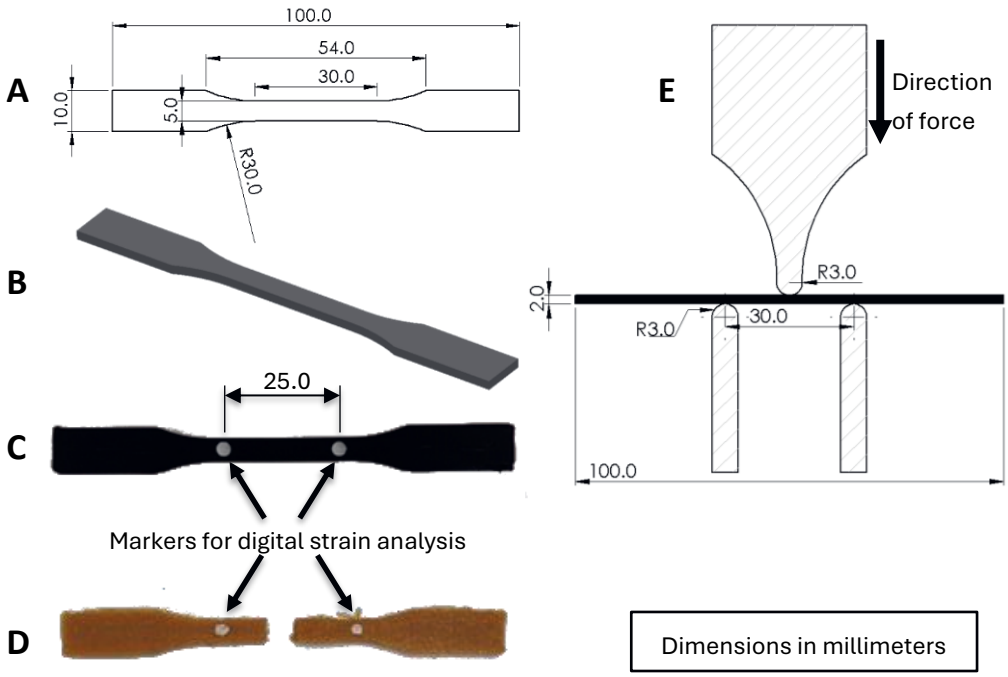


Fig. 3.2 Visualization of mechanical tests. A: technical drawing of sample type 1BA outlined in ISO 572-2 for tensile testing. B: 3D render of sample type 1BA. C: photo of 3D printed PETG sample. D: photo of 3D printed zein-composite sample after tensile testing; E: schematic overview of three-point bending flexural test according to ISO178:2019 method A with the sample indicated in black.

3.2.4.3 Flexural properties

Surface defects and microcracks in brittle materials are easily propagated during uniaxial extension testing and can result in early fracture. During three-point bending flexural tests such material defects are less influential, thus fracture properties of brittle materials (like objects printed using zein filament) can be measured more reproducibly.

The flexural modulus was determined by performing three-point bending tests with an UTM according to ISO 178:2019 method A (**Fig. 3.2E**). The three-point bend fixture consisted of a loading, upper anvil with a 3.0 mm radius and a support beam with 3.0 mm radius anvils with a span (L) of 30 mm. Rectangular specimens (100x5x2 mm) were used and force was applied at the midpoint of the supported beam using a crosshead speed of 2 mm/min. A preload of 0.05 N was used. Deflection was determined by crosshead displacement and corrected for system compliance. The flexure test was terminated when the load cell measured a force drop of 100 N or a flexural strain of 5% was reached. The flexural strain, stress and modulus were calculated using **equations 3.4, 3.5 and 3.6** provided in ISO178:2019.

$$\sigma_{Flex} = \frac{3FL}{2bh^2} \qquad \textit{Eq. 3.4}$$

$$\varepsilon_{Flex} = \frac{6sh}{L^2} \qquad \textit{Eq. 3.5}$$

$$E_f = \frac{\sigma_{Flex,2} - \sigma_{Flex,1}}{\varepsilon_{Flex,2} - \varepsilon_{Flex,1}} \qquad \textit{Eq. 3.6}$$

With F the force applied by the load cell (n), L the span (mm), b the specimen width (mm), h the specimen height and s the deflection (mm). Flexural modulus was calculated as the slope of the linear section of the stress-strain curve between 0.05 and 0.25% of flexural strain ($\varepsilon_{Flex,1}$ and $\varepsilon_{Flex,2}$ respectively).

3.2.5 Statistical analysis

Statistical analysis was performed using the statsmodels package (v0.14.5) in Python (v3.13, Python Software Foundation, USA). The number of repetitions (n) is reported with the results. Significant differences between

sample types were determined by one-way analysis of variance (ANOVA), followed by pairwise comparison of means using Tukey's honestly significant difference test with $\alpha < 0.05$.

3.3 Results and Discussion

3.3.1 Formulation development

3.3.1.1 Thermal properties - suppression of glass transition temperature by fatty acids

Extruded zein is brittle after cooling down to room temperature, but addition of plasticizers increases the ductility and flexibility of polymers, and lowers their glass transition temperature and melt viscosity (Ebnesajjad, 2016). The glass transition of an amorphous polymer entails a transition from a brittle glass to a soft and elastic material (Gontard and Ring, 1996). The glass transition temperature of zein was modified through addition of glycerol and fatty acids (see **Fig. 3.3**). A homologous series of fatty acids was used to investigate the effect of the alkyl chain length, including hexanoic acid (6:0, $C_6H_{12}O_2$), lauric acid (12:0, $C_{12}H_{24}O_2$) and stearic acid (18:0, $C_{18}H_{36}O_2$). To investigate the effect of an unsaturated bond oleic acid was used (18:1 Δ9c, $C_{18}H_{34}O_2$). Hexanoic acid fully crystallised before ethanol evaporation completed during the drying step of pellet making. It was therefore excluded from further investigation.

The efficacy per mole of fatty acid towards reducing the T_g is highest for lauric acid, followed by oleic acid and lastly stearic acid (**Fig. 3.3**). In contrast with hydrophilic glycerol, fatty acids are amphiphilic and can engage with zein in nonpolar interactions in addition to hydrogen bonding. The length and degree of saturation of the hydrocarbon chain do not affect the amount of hydrogen bonds the fatty acid can engage in with zein (Di Gioia and Guilbert, 1999). However, FA chain length affects hydrophobicity, and LA's greater

efficacy compared to SA thus indicates that it has more possibilities for thermodynamically favourable interactions with zein along its length (Di Gioia and Guilbert, 1999).

The effect of SA on T_g depression per mole is slightly less than OA. Although their hydrocarbon chains are of equal length, the slightly reduced efficacy could be explained by the fact that SA is fully saturated. The *cis* double bond in OA introduces an irregularity in the carbon chain, which strongly reduces its viscosity and melting point compared to a saturated, straight-chain fatty acid (Knothe and Steidley, 2005). Therefore we expect that OA can have more apolar interactions with zein polymer molecules compared to SA, resulting in more effective T_g depression.

3.3.1.2 Thermal properties - plasticization effect of glycerol/FA blends

In our previous work we demonstrated that at lower molar ratios of glycerol to zein, the T_g of zein-glycerol composites follows Gordon-Taylor kinetics (Steffens et al., 2025). However, phase separation did occur in zein-glycerol composites with more than 12.5% w/w of straight glycerol, equal to a molar ratio of 35.6 (**Fig. 3.3A**). The experimentally determined T_g of the samples containing a larger amount of glycerol did not follow the trend predicted by Gordon-Taylor kinetics, implying that the addition of more glycerol to the composite does not effectively depress T_g anymore (Steffens et al., 2025).

In the current work, OA/G blends at 1:3, 1:1 and 3:1 ratios were used to plasticize zein, to study the effect of combining hydrophilic and amphiphilic plasticizers (**Fig. 3.3B**). OA was selected for blending with glycerol over other FAs as it does not crystallize out of the zein matrix during storage of filament at room temperature due to its low melting point.

At all three blending ratios of oleic acid to glycerol, the experimentally determined glass transition follows a downward trend with increasing plasticizer levels. We extrapolated the Gordon-Taylor model for zein-glycerol composites to molar ratios over 35.6 (**Fig. 3.3B**). Even above this critical concentration, where phase separation was observed prior for zein-glycerol composites, the OA/G blends yield a reduction in T_g with increasing molar ratios of plasticizer to zein. Also, the decrease of T_g in samples containing OA/G blends (**Fig. 3.3B**) was larger compared to samples containing either OA or glycerol alone (**Fig. 3.3A**). This indicates that blending plasticizers both provides a synergistic effect on the T_g reduction and allows the incorporation of higher quantities of plasticizer. The same synergistic plasticization effect was previously reported for zein films (Xu et al., 2012). Increasing the oleic acid content of extruded zein sheets reduced their T_g, which resulted in lower tensile strength and more elongation at break (Wang and Padua, 2003).

Summarizing, a combination of the hydrophilic plasticizer glycerol and the amphiphilic oleic acid provides a clear benefit over plasticization with glycerol or OA alone. Thus, OA/G blends are interesting for further investigation to increase filament flexibility and spoolability.

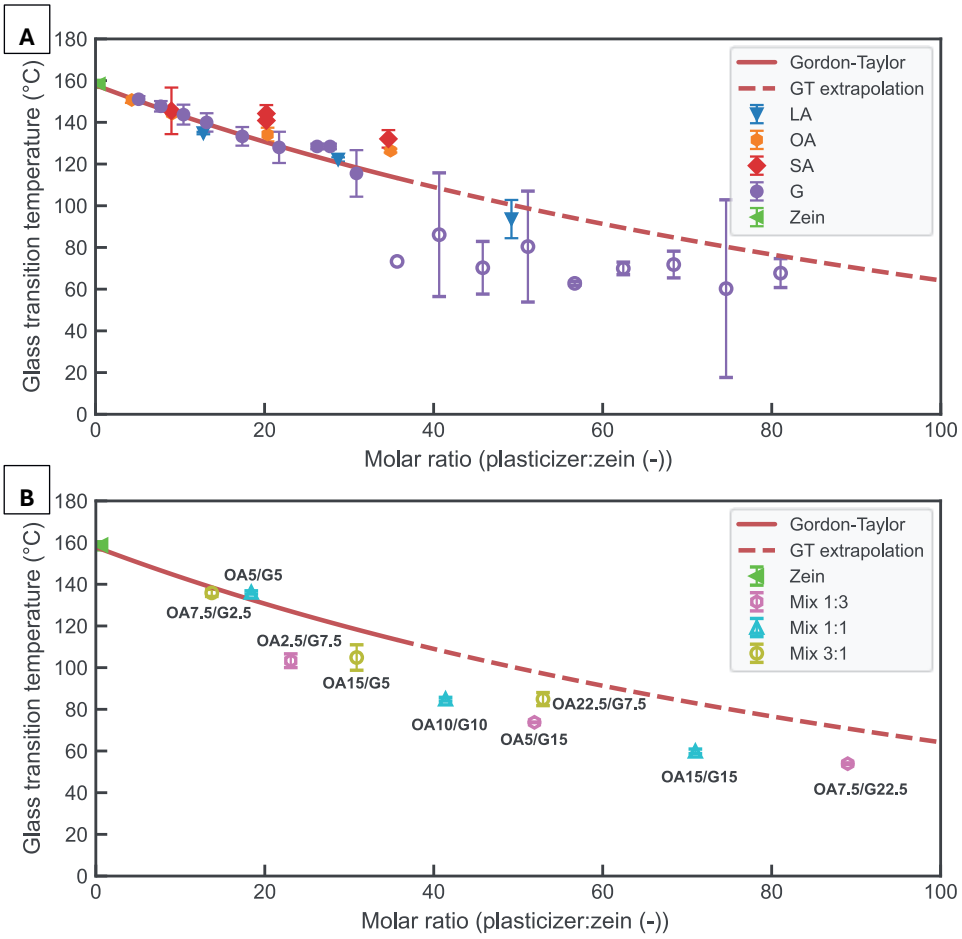


Fig. 3.3 Midpoint glass transition temperature (T_g) of pelletized zein and zein-plasticizer composites as determined by mDSC. A: Zein and zein composites with lauric acid, oleic acid, stearic acid and glycerol. B: Zein and zein composites with glycerol-oleic acid mixed at mass ratios of 1:3, 1:1 and 3:1. Data for zein-glycerol composites and Gordon-Taylor parameters for zein-glycerol composites are obtained from our previous work (Steffens et al., 2025). Experimentally measured T_g values for samples containing glycerol are shown as closed (no phase separation) and open symbols (phase separated); the continuous line represents a trendline interpolated from experimental data with the Gordon-Taylor model and the dashed line represents extrapolated data from the same model.

3.3.1.3 Comparing thermogram of pelletized and powder-blend zein composite

Two ways of forming zein composites were proposed in the current work: 1) powder blending and 2) solubilisation followed by drying and pelletizing. It

was expected that the pelletizing method would result in a more homogenous distribution of plasticizers in the polymer matrices, however, it is more time and resource intensive. The thermograms of powdered and pelletized samples of zein with lauric acid or stearic acid (LA20 and SA20) were compared to study differences between the two forming methods. The powder blends show distinct melting peaks at 45.1 ± 0.3 °C and 70.6 ± 1.4 °C (see section 'DSC melting peaks' in **Appendix 3**). This matches well with literature values of 43.8 °C and 69.3 °C for the melting points of LA and SA, respectively (Lide, 2006) and suggests heterogeneous distribution of the FAs in the powder samples (Pommet et al., 2003). The melting peaks for pelletized zein with lauric acid and stearic acid (n = 2) are 12.8 and 6.0 times smaller, suggesting increased zein-FA interaction and improved plasticization **(Table 3.1)**. It also matches our observation of improved plasticization of pellets compared to powder blends in our previous work (Steffens et al., 2025). As OA has a peak melting temperature of 12.8 °C and samples were conditioned at room temperature, no melting peaks were observed in the thermograms of zein with oleic acid in the present work (Knothe and Dunn, 2009).

Table 3.1 *Thermal properties of powder versus pelletized samples of zein-lauric acid and zein-stearic acid composites*

	Melting enthalpy (J/g)	Melt peak temperature (°C)
LA20 powder	30.0 ± 1.2	45.0 ± 0.3
LA20 pellet	2.3 ± 0.2	52.0 ± 0.6
SA20 powder	37.0 ± 8.3	70.9 ± 0.1
SA20 pellet	6.1 ± 0.1	68.4 ± 0.5

Although the solvent casting process utilized to produce the pellets resulted in increased zein-FA interaction, it is an expensive process that is difficult to

scale up for industrial production (Wang and Padua, 2003). Previous literature indicates that the kneading action by the screws inside extruders also increases zein-FA interaction which could lead to higher homogeneity of the composite (Wang and Padua, 2003). Therefore, we focused on (micro)compounding to investigate the formation of zein filament as function of the type and concentrations of plasticizers (see Section 3.3.2). Melt compounding is the preferred way of producing zein filament, since the compounding (mixing) and extruding processes can be completed in a single step and upscaling is straightforward.

3.3.1.4 Rheological properties: temperature-dependent viscosity

The rheological behaviour of zein composites was investigated to identify which formulations have an optimal viscosity for extrusion. First, strain sweeps were performed to identify the linear viscoelastic regime and critical strain of various composites. The lowest critical strain value among all samples was found to be 1.95% (see Supplementary Materials, section 'Critical Strain), thus the effect of temperature on viscosity was investigated using temperature sweeps at 1.95% strain.

The reduction in glass transition temperature of zein by each unique blend of glycerol-fatty acid mixtures correlates well with the observed reduction in complex viscosity during temperature sweeps at a temperature range of T_g to T_g + 90 °C, representative for extrusion processing temperatures (**Fig. 3.4**). One exception is observed for OA5/G15, which had a similar viscosity profile to OA10/G10, despite the difference in their glass transition temperatures (see section 'Viscosity' in Supplementary Materials). Glass transition temperature of zein was most effectively lowered by blends of glycerol and oleic acid, and the lowest viscosity at a fixed temperature is obtained for sample OA7.5/G22.5 (**Fig. 3.4A**).

Optimal mechanical properties are achieved in FDM with good bonding between deposited strands. Optimal intra- and interlayer fusion of PLA filaments was reported for melt viscosities of 200 Pa·s or lower, due to ideal cross-flow and minimal air-gaps (Spoerk et al., 2017). Although slightly different strain and frequency were used to determine the complex viscosity during temperature sweep in the study by Spoerk et. al compared to ours (3% and 15 Hz, compared to 2% and 10 Hz, respectively), the viscosity value of 200 Pa·s was taken as a referent value in this study to compare the rheological behaviour across different formulations. This viscosity threshold could be achieved with multiple zein composites (**Fig. 3.4A**). However, zein may crosslink at temperatures of 120 °C or higher and tensile properties of the resulting films or filaments can deteriorate at longer residence times at temperatures exceeding 140 °C (Selling, 2010). Composite OA7.5/G22.5 was the only formulation that reached a viscosity lower than 200 Pa·s at a temperature below 140 °C, allowing longer residence times during extrusion for filament fabrication and FDM processes. Therefore, FDM of OA7.5/G22.5 with nozzle temperatures of 120-130 °C was not expected to be influenced by time-dependent effects on viscosity (i.e. crosslinking of zein) because the zein composite would not be exposed to temperatures over 120 °C long enough to cause crosslinking.

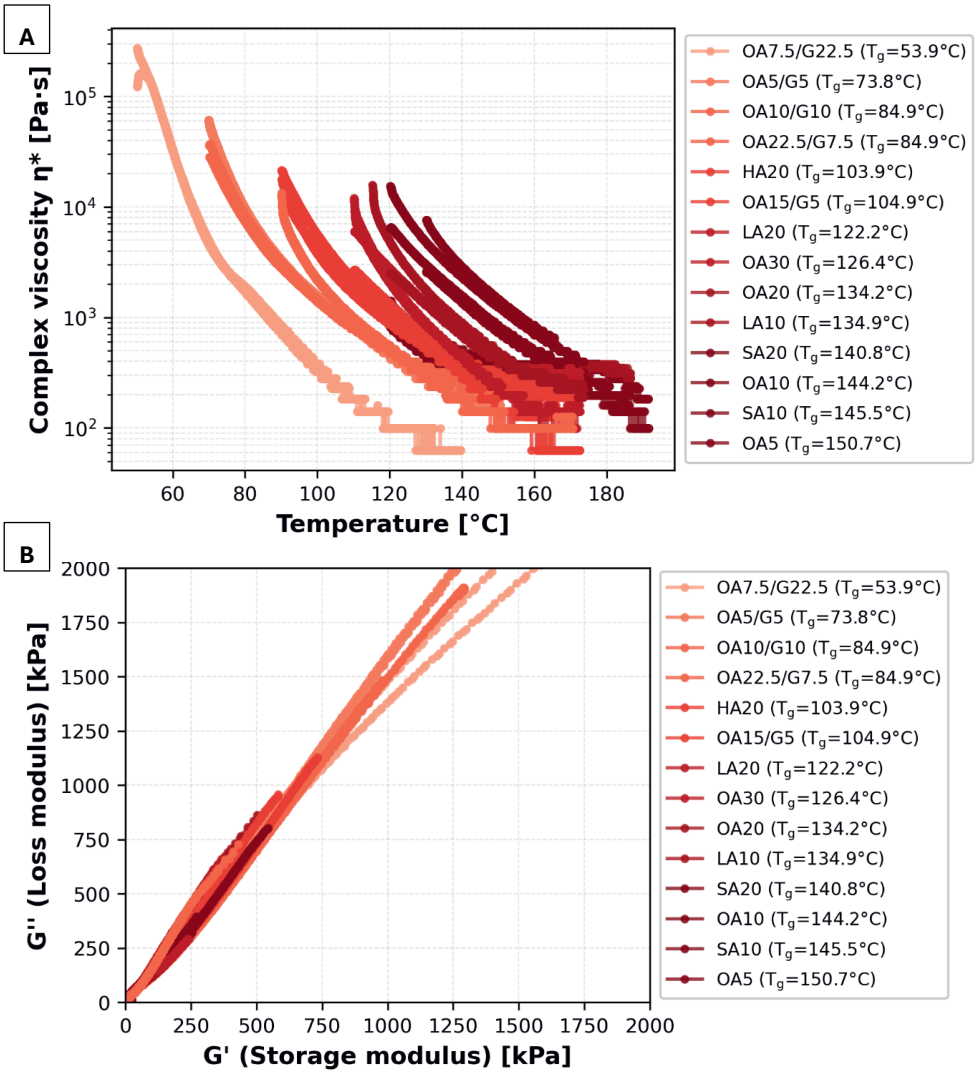


Fig. 3.4 A: Complex viscosity (η*) as function of temperature for zein-fatty acid and zein-fatty acid-glycerol composites B: Cole-Cole plot of those composites. The saturation and darkness of the red colours with which the data was plotted corresponds to the increasing of T_g values of the composites.

We observed that the ratio between the loss and storage moduli collapsed onto a master curve in a Cole-Cole plot, although some deviations are visible for G" exceeding 1500 kPa (Fig. 3.4B) (Friedrich and Braun, 1992). These deviations could be related to the experimental conditions during rheological

analysis. The exact T_g values are also slightly dependent on the DSC protocol utilized. Furthermore it is often acknowledged that T_g values as identified by DSC may deviate slightly from those identified using DMTA or NMR (Kalichevsky et al., 1992; Rahman et al., 2007). The existence of a master curve implies that specific rheological profiles can be achieved for zein composites irrespective of the specific plasticizer used, as their rheology is governed by T_g.

3.3.1.5 Phase mobility

To further investigate the phase mobility in zein composites with glycerol and/or fatty acids, NMR was employed to identify T_2 relaxation times of pelletized composites. Representative T_2 spectra of zein-glycerol composites are shown in **Fig. 3.5**. The shortest peak time in T_2 spectra is indicative of the mobility of the largest polymer, in this case zein. With increasing glycerol content of the zein-glycerol composites, the T_2 relaxation time corresponding to the main peak (signal with the largest amplitude) gradually shifts to longer times, widens and decreases in amplitude (**Fig. 3.5**). This indicates that glycerol is being absorbed by the zein matrix, making the matrix more mobile. Pure glycerol shows a T_2 peak at 30 ms, which is observed in zein-glycerol composites as a tertiary peak. However, the area under the curve of this peak in the composites is smaller than the weighted average of the 100% zein and 100% glycerol spectra. This indicates that glycerol is partially absorbed by the zein matrix. At glycerol levels over 11% tertiary peaks increase in height and width, which is indicative of population transfer. This aligns with the critical phase separation concentration (≥12.5% w/w) observed for zein pellets (Steffens et al., 2025).

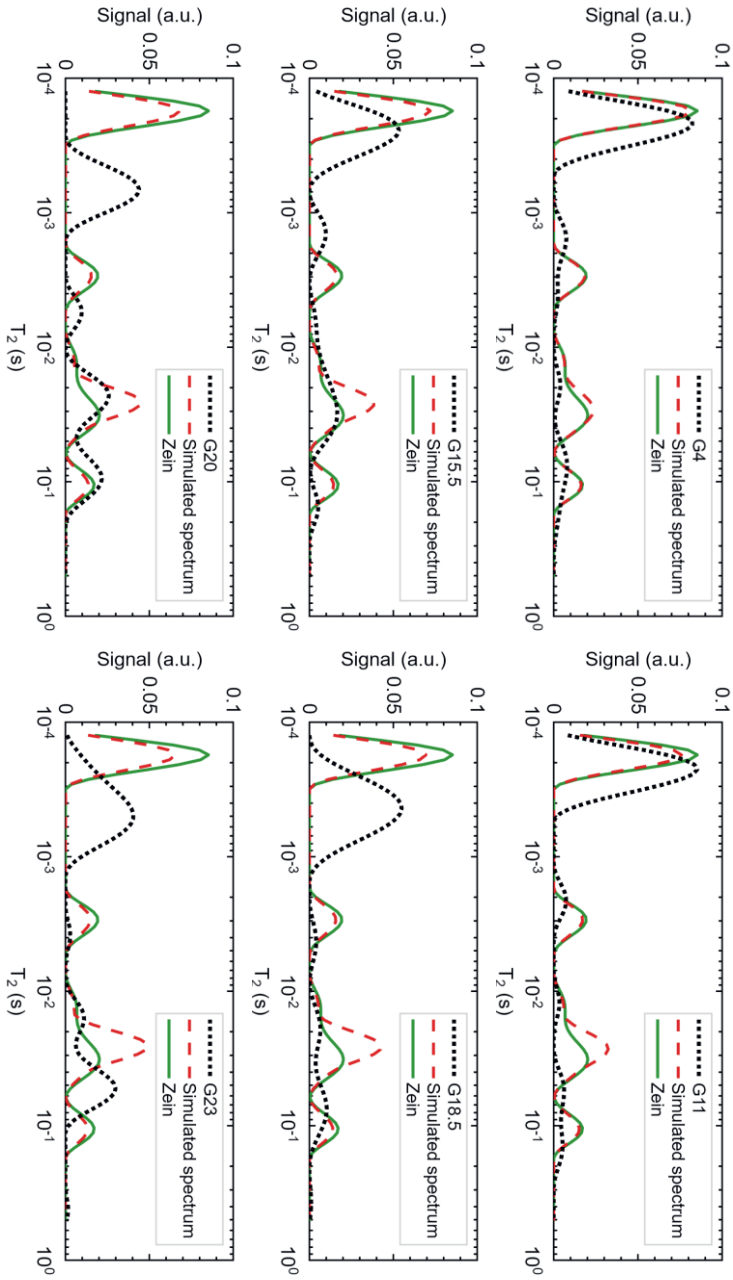


Fig. 3.5 *T_2-NMR spectra of zein plasticized with increasing levels of glycerol. Green graphs represent a 100% zein baseline, black graphs represent measurement data and red graphs represents a weighted average of the 100% zein and 100% glycerol baseline measurements*

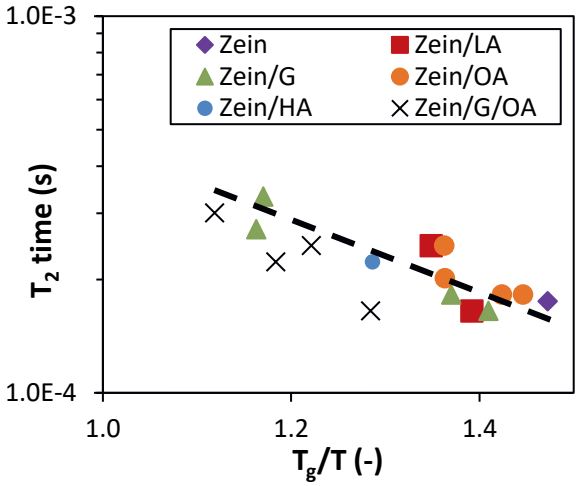


Fig. 3.6 *Time of first T2-peak of pelletized zein and zein composites as function of Tg/T. The dashed line is drawn to guide the eye. Due to the existence of a glassy state in the composites, an asymptote is observed at Tg/T=1*

T_g/T is known to control the plasticizing behaviour by small carbohydrates as well as rheological properties of plant protein systems, and T_2 relaxation times have been linked to intermolecular hydrogen bonding density (Purcell et al., 2025; Siemons et al., 2022; van der Sman et al., 2026, 2023). A correlation between T_g/T and the shortest T_2 peak time is apparent when reviewing all zein-FA composites (**Fig. 3.6**). Here T represents the NMR measurement temperature of 20 °C. This correlation is not indicative of phase separation, but it can be concluded that as T_g/T becomes smaller, the T_2 peak times become longer and thus the polymer is more mobile. This indicates that the majority of the plasticizer is strongly bound to zein. Wang et al. confirmed that hydrogen bonds are formed between FAs and zein in films containing zein using FTIR, and suggested that intermolecular hydrogen bonds increase as FA concentration is increased (2025). In conclusion, a combination of

glycerol and fatty acids is most promising for filament production as it is effective in increasing zein mobility.

3.3.2 Filament production

3.3.2.1 Pilot scale

Compounding trials were performed using a micro-compounder, to investigate how the formulation affects the properties of edible filaments in terms of appearance, consistency in diameter, roundness of the cross-section, die swell and flexibility (i.e. spoolability). The micro-compounder has a backflow channel, which allowed measurement of the viscosity of the material during mixing. Compounding of zein composites was continued until a stable viscosity was reached (i.e. indicative of a homogeneous blend). Based on the results discussed in section 3.3.1, selected formulations were tested during compounding trials (**Table 3.2**).

Being able to wind the filament around a spool is a core requirement for FDM. Filaments SA20, LA20, OA20, OA15/G5 and OA10/G10 were too brittle to wind around a spool (**Fig. 3.7** and **Table 3.2**). The surface of these filaments was also rough, with clear grooves in the longitudinal direction, a consequence of the stiffness of the filament. In contrast, filaments G20 and OA22.5/G7.5 were flexible enough for winding and had smooth surfaces.

On close observation, some air bubbles could be observed in all filaments (e.g. lighter areas in **Fig. 3.7D**). This is due to the absence of a dedicated (vacuum) degassing zone on the compounding device. A large pressure drop at the exit die, indicated by a large amount of die swell (**Table 3.2**) increases the size of these air bubbles. Air bubbles were less visually apparent in materials containing fatty acids due to their opaqueness, but still present. Opaqueness, or increased light scattering, indicates a compacter, less plasticized zein network. The degree of opaqueness can be related to the

hydrophobicity of the fatty acids, as these may cluster together and give rise to inhomogeneities (Wang et al., 2025).

To yield optimal 3D printing performance on standard FDM printers, filaments must also have a round cross section and a consistent diameter of 1.75 mm. Several factors may cause the cross section to become more eccentric, such as differential shrinkage due to shear-induced molecular orientation (Sola, 2022). Therefore, the cross-section of the filaments was inspected for roundness, which revealed that some samples suffered from partial exudation of the fatty acid plasticizer (see section 'Visual appearance filaments' in **Appendix 3**).

Despite the disadvantages of batch processing mentioned above, it was possible to assess which filaments showed the least fluctuations in diameter during the extrusion process and most closely matched the 1.75 mm diameter target of industrial filament production (Consistent Diameter and Average Diameter columns in **Table 3.2**). At 20% w/w plasticizer, the formulation with 20% w/w glycerol as plasticizer came closest to the target diameter and was flexible enough to wind around a spool. Out of the extrudates with 30% w/w plasticizer, the OA7.5/Gly22.5 composite performed the best on spoolability and target diameter while the consistency of the filament diameter was acceptable. The OA7.5/Gly22.5 composite formulation was therefore selected for upscaling.

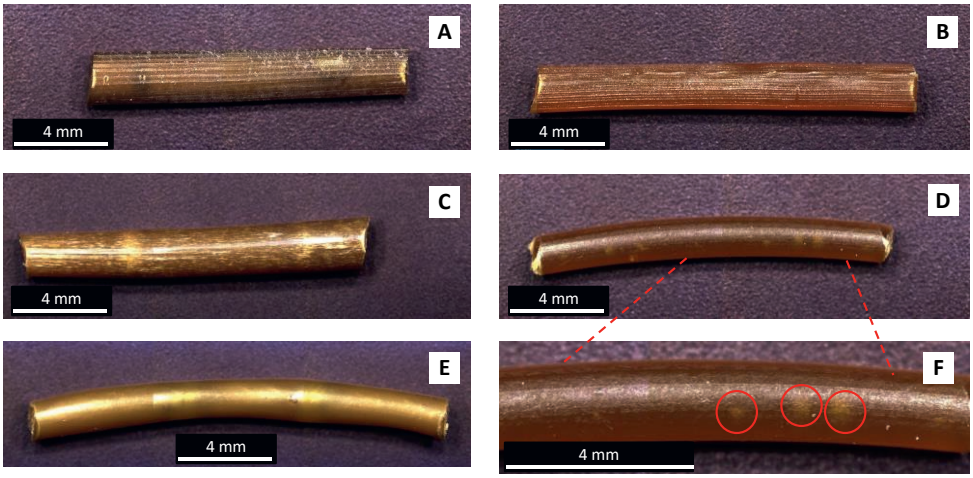


Fig. 3.7 Microscopic images (35x) of filaments of SA20 (A), LA20 (B), OA20 (C), G20 (D, F) and OA22.5/G7.5 (E). Scalebar represents 4 mm. Air bubbles trapped inside the filament are encircled in red in F.

Table 3.2 Observations on the diameter, die swell and spoolability of filaments obtained during extrusion.: '+++' indicates that the characteristic was very strongly observed, '++' strongly observed, '+' moderately observed, or '-' not observed.

	Sample	Diameter range (mm)	Average diameter (Δ from target) (mm)	Consistent diameter	Round cross-section*	Die swell	Spoolability
80% zein	SA20	1.47 – 3.84	2.09 (Δ0.34)	+++	+++	+++	-
	LA20	1.17 – 2.95	2.23 (Δ0.48)	+	+++	++	-
	OA20	1.72 – 2.51	1.98 (Δ0.23)	+++	+++	+++	-
	G20	1.37 – 2.21	1.87 (Δ0.12)	++	++	++	+++
	OA15/G5	1.23 – 2.12	1.82 (Δ0.07)	++	+++	++	-
	OA10/G10	1.30 – 2.73	1.79 (Δ0.04)	+++	++	++	-
	OA5/Gly15	1.10 – 2.68	1.59 (Δ0.16)	++	++	++	++
70% zein	OA22.5/G7.5	0.17 – 2.19	1.43 (Δ0.32)	+++	++	+	++
	OA15/G15	1.09 – 3.09	1.59 (Δ0.16)	++	+	+	+++
	OA7.5/G22.5	1.60 – 2.51	1.79 (Δ0.04)	++	+	+	+++

* See 'Visual appearance filaments' section in Appendix 3 for scoring reference images

3.3.2.2 Continuous extrusion

Upscaling of the filament production was required to produce sufficient filament for 3D printing experiments. The extrusion process could be further optimized at this scale. Instead of a batch process, continuous extrusion was employed, improving the consistency of the pressure drop at the extrusion die. The modular design of the extrusion screw was adjusted to include backflow mixing zones. A dedicated degassing zone was utilized, to reduce the possibility of trapping air bubbles in the filaments. Finally, the filaments

were cooled in a water bath, which provides faster thermal transfer than forced air cooling.

The OA7.5/G22.5 filaments produced during continuous extrusion did not contain air bubbles, homogeneity was improved and the surfaces were smoother compared to filaments produced during batch extrusion. Furthermore, the fluctuations around the target diameter were reduced and the filament roundness was improved (absence of oval shaped sections). The filament density was measured to be 1.24 g/cm^3, which is very similar to commercial PLA and PETG filaments used in this study at 1.24 g/cm^3 and 1.28 g/cm^3 respectively.

To the authors best knowledge, this is the first time that the feasibility of edible filament production for FDM at larger scale has been proven .

3.3.3 3D printing and mechanical properties

3.3.3.1 Fused Deposition Modelling

3D printing was performed using a commercial FDM printer. Process and filament settings for FDM 3D printing were optimized using OrcaSlicer's build-in manual calibration tools. In short, bed temperature was increased in steps of 5 °C until a test print could be completed without detaching from the print bed during the FDM process. The initial nozzle temperature range was determined by observing the minimal nozzle temperature to achieve consistent flow, and the highest temperature that did not cause clogging or burning of the filament. The extrusion flow rate was adjusted to prevent over- and underextrusion through calibration of the extrusion multiplier (EM), which is a multiplier of the extrusion flow rate. EM was calibrated by printing squares with a range of extrusion multiplier values and subsequently selecting the EM setting at which individual lines were well connected but not overlapping. The maximum flow rate was tested by increasing the volumetric

print speed while printing straight lines until gaps in the printed lines were observed. Overall, a bed temperature of 60 °C, nozzle temperature of 140 °C, extrusion multiplier of 1.00, and maximum flow rate of 9 mm^3/s were determined. Cooling fans were used during all print runs. The detailed process and filament settings are provided in the 'FDM print' section of **Appendix 3**. The optimized settings were utilized to print samples for mechanical testing (see **Fig. 3.2D**). We demonstrated the feasibility to print more complex structures such as spiral spring and a 3D benchy (i.e. a popular 3D printing benchmark model) (**Fig. 3.9**). To the authors best knowledge, this is the first time that FDM with edible filaments has been achieved. To further improve the print quality of structures that contain overhangs, optimization for bridging or retraction could be performed in future.

3.3.3.2 Tensile and flexural properties of 3D printed parts

Characterisation of the tensile and flexural properties benefits the computer-aided design process as the mechanical properties of a finalized part can be predicted at the design stage, enabling simulations of real-world application scenarios. The current study compared the mechanical properties of samples printed using our edible filament and two commercial filaments (PLA and PETG).

Tensile testing of dog-bone shaped specimens yielded Young's moduli of 2733 ± 121 MPa for PLA and 2027 ± 75 MPa for PETG (**Fig. 3.8A**), which are in close agreement with values reported by the manufacturer of 2580 ± 220 MPa and 1810 ± 190 MPa, respectively. The low standard deviation of our measurements indicates the good reproducibility of the printing process. Young's modulus of dog-bone shaped specimens printed with zein filament (OA7.5/G22.5) was 555 ± 107 MPa (**Fig. 3.8A**). The relatively high standard deviation of the zein filament is related to the larger variation in filament

diameter compared to commercial filaments (± 0.1 and ± 0.02 mm, respectively). Lower filament diameters cause underextrusion, which reduces the intra- and interlayer welding strengths.

A strong correlation is observed between Young's moduli and the flexural moduli, affirming that both methods reflect the true material properties (**Fig. 3.8A-D**). PLA is the stiffest material, followed by PETG and finally OA7.5/G22.5.

OA7.5/G22.5 specimens fractured at a flexural strain of 1.0 ± 0.1% whereas PLA and PETG specimens did not fracture prior to reaching the predefined experimental limit of 5% strain (**Fig. 3.8B,C**). Although PLA is stiffer than PETG, the flexural stress plateaued at similar values during the three-point bending test, namely 63.5 ± 3.4 and 61.1 ± 2.5 MPa, respectively (**Fig. 3.8C**). The strain at break (extensibility) is larger for PETG than PLA specimens, which is in line with literature and manufacturer data. The maximum tensile stress that was achieved before fracture with the edible dog-bone shaped specimens was approximately 13% of that for PLA references (**Fig. 3.8E**). It is important to note that the suitability of FDM materials is highly dependent on the desired application, thus the lower stiffness and fracture stress of OA7.5/G22.5 filament compared to PLA and PETG are not negative aspects per se. The FDM process allows for several strategies to increase the strength and stiffness of printed samples, such as annealing to improve polymer sintering between extruded strands, tweaking of the extrusion multiplier to increase contact area between strands and tuning of printing temperature to improve cross-flow and minimize air gaps (Mackay, 2018; Spoerk et al., 2017).

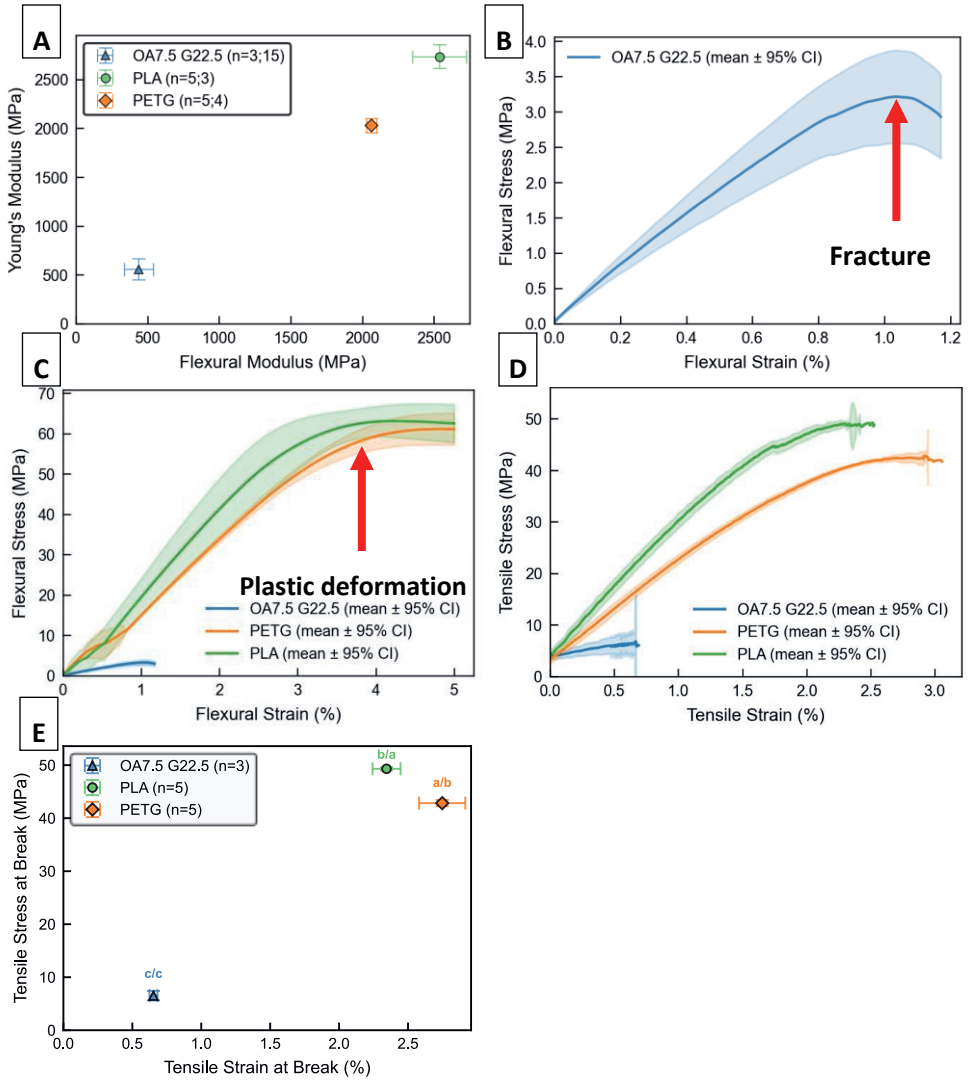


Fig. 3.8 *Mechanical testing results of 3D printed dog-bone shaped specimen. A: Young's modulus (from tensile testing) compared to flexural modulus (from 3-point bending testing) for OA7.5 G22.5, PLA and PETG. Numbers between brackets indicate number of samples measured in tensile and bending test respectively. B: mean ± 95% confidence interval plot of flexural strain-stress curves of three-point bending of OA7.5/G22.5 C: as B but comparing OA7.5/G22.5, PLA and PETG dog-bone shaped specimens D: mean ± 95% confidence interval plot of tensile stress-strain curves of OA7.5/G22.5, PETG and PLA. E: Fracture stress and strain of OA7.5/G22.5, PLA and PETG. Sample groups with a shared letter are statistically similar based on Tukey HSD test, with letters assigned based on rank, representing tensile strain/tensile stress respectively.*

3.3.3.3 Printing complex geometry

To demonstrate the feasibility of producing mechanical components with OA7.5/G22.5 filament, spiral springs were produced (**Fig. 3.9A-C**). The shape fidelity of the printed samples was high and flexing/winding was possible up to a rotation of 140 degrees prior to fracture, demonstrating the ability of the spring to be wound up and store elastic energy for release at a later time. To compare the printing quality of OA7.5/G22.5 filament to other materials, the 3D benchy was printed as well. This model contains many design elements that are difficult to print and as such is a 3D printing 'torture test', often utilized as the golden standard for assessing 3D print quality (**Fig. 3.9D-F**). With the OA7.5/G22.5 filament, the low-slope surfaces, overhangs and horizontal holes could be successfully printed. Retraction performance became a limiting factor for completing the print at the upper part of the boathouse, probably due to insufficient calibration. This can most likely be resolved through further tuning of printer settings and hardware. The current results prove that mechanical components and complex features can be printed successfully, which is an excellent result for edible filament at this time.

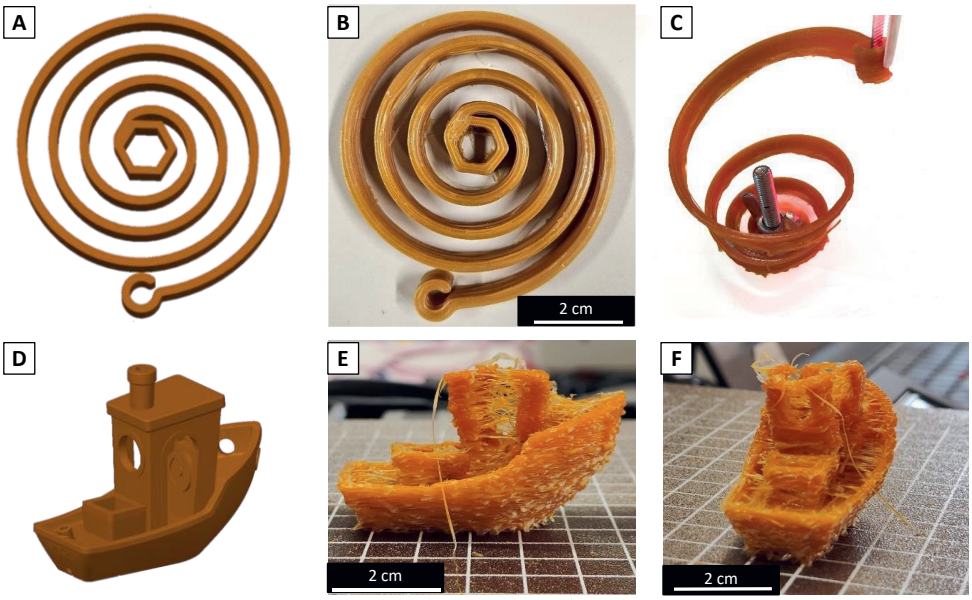


Fig. 3.9 *3D rendered images and digital photos of prints with complex geometry. A: Render of spiral spring B: Spiral spring printed with zein filament formulation OA7.5/G22.5 C: Demonstration of flexibility of spiral spring by pulling it using a tweezer D: Render of 3D benchy E,F: 3D benchy printed with zein filament formulation OA7.5/G22.5*

3.4 Conclusion

Developing protein-based materials for FDM 3D printing can broaden its applications. However, protein-based filament feedstocks often suffer from brittleness and phase separation, which limits their adoptability in FDM. This study investigated the formulation, larger-scale production and FDM printing of edible zein-based filaments. The filament development was guided by thermal, rheological and phase mobility analyses, which provided insights for optimizing zein-plasticizer composites for improved material properties and processability. The rheological behaviour of zein composites was governed by their glass transition temperature. Oleic acid and glycerol worked synergistically to lower the zein composite glass transition temperature to limit filament brittleness while maintaining high phase compatibility. Zein-based filaments were utilized to print complex designs using a commercial

FDM 3D printer without any modifications. The modulus and tensile strength of structures printed with edible filaments were lower than the ones printed with PLA and PETG references. For the first time, FDM with edible filament was achieved. The results of this work contribute to improving the applicability of protein-based materials in FDM. Future studies may focus on optimizing printing parameters (e.g. retraction performance) to further improve print quality of edible filaments and exploring the applications of edible filament in 3D food/bio-printing.

Appendix 3

A3.1 Viscosity

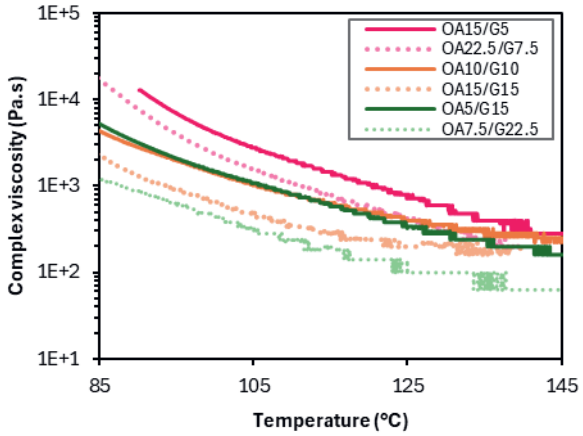


Fig. A3.1 Effect of temperature on the complex viscosity of zein-oleic acid-glycerol composites with 20% plasticizer (continuous lines) or 30% plasticizer (dashed lines). Different blending ratios of OA to G are represented by different colours

A3.2 Microcompounder

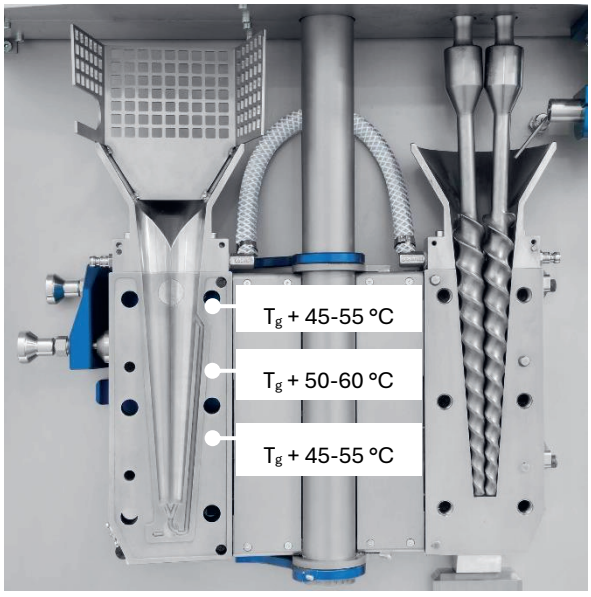


Fig. A3.2 Xplore microcompounder with three heating zones

A3.3 Melting enthalpy

Thermograms obtained from DSC analysis of zein plasticized with lauric acid or stearic acid

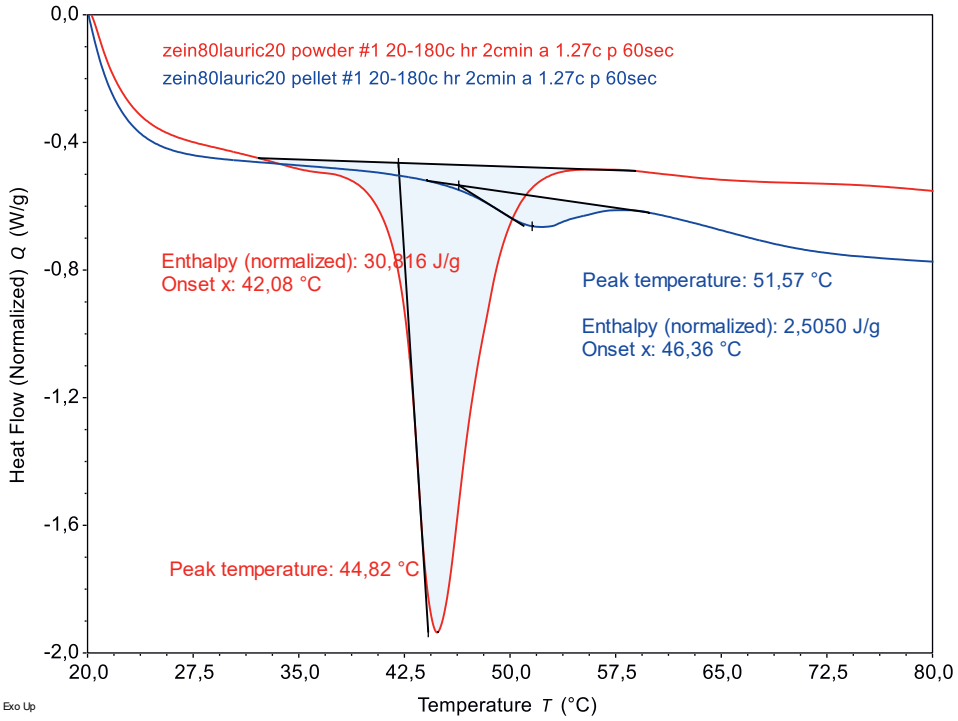


Fig. A3.3 *Representative thermogram of first heating ramp for powder (red) and pellet (blue) zein sample with 20% w/w lauric acid*

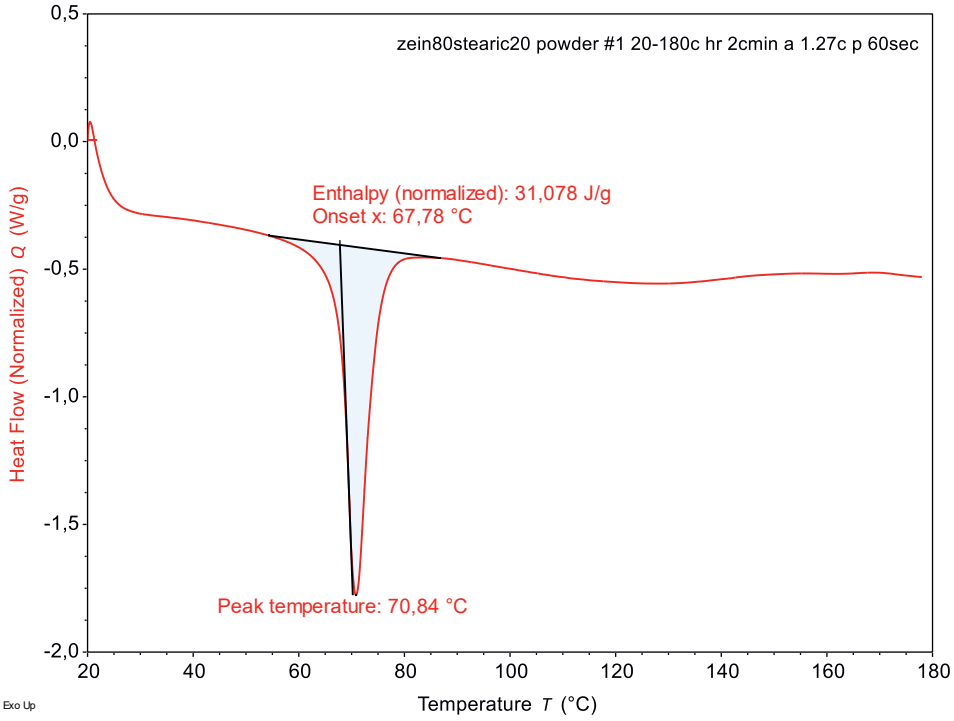


Fig. A3.4 *Representative thermogram of first heating ramp for powder sample with 20% w/w stearic acid*

A3.4 Critical strain

Critical strain as determined by CCR using strain sweeps at a frequency of 10 Hz and temperature of 110 °C for different pellet formulations

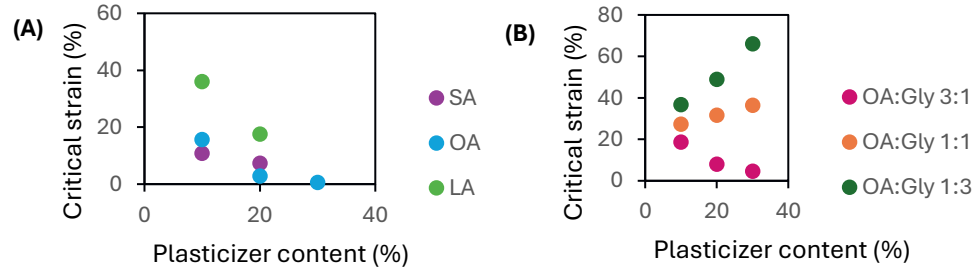


Fig. A 3.5 *Critical strain [%] determined for zein formulation at increasing plasticizer concentration [%] of SA, OA, LA (A) and OA:Gly blends at 3:1, 1:1 and 1:3 ratio (B).*

A3.5 Visual appearance filaments

Visual appearance of filaments produced using microcompounder after 1 week of storage.

Table A3.1 *Roundness scoring reference images. +++ indicates near perfect roundness, ++ a small deviation from perfect roundness and + a large deviation from perfect roundness. From left to right, samples OA7.5/G22.5, G20 and OA15/G5, with deviation from roundness indicated in pink.*

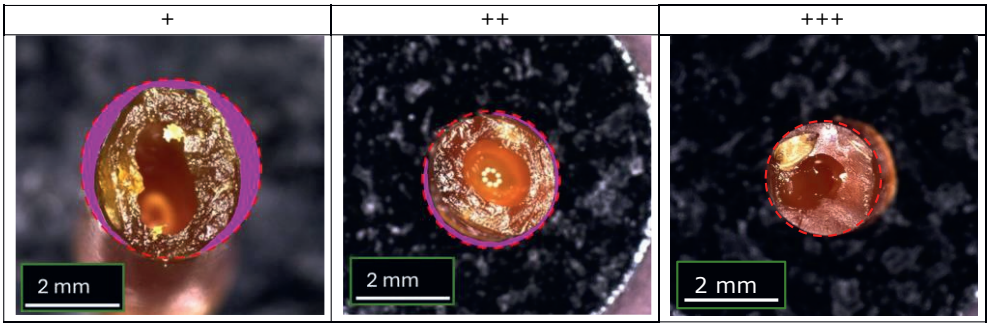
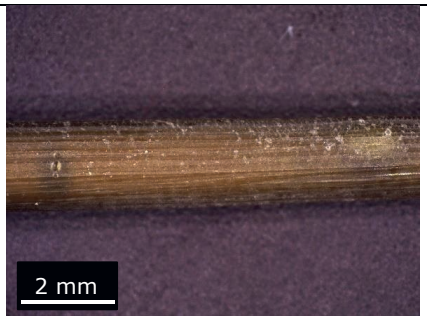
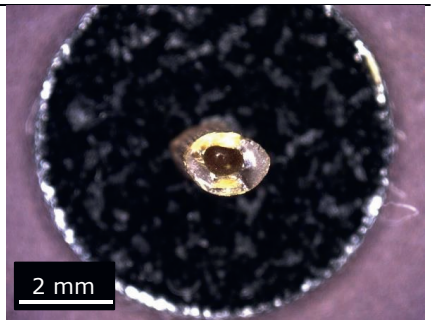
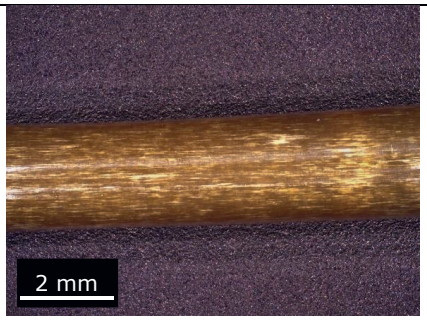
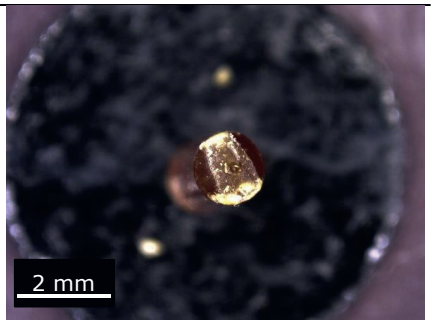


Table A3.2 *Smartzoom microscope images (35x) of filaments containing 20% (w/w) SA, OA, LA or G produced using microcompounder*

Sample	Outer surface	Cross section
SA20		
OA20		

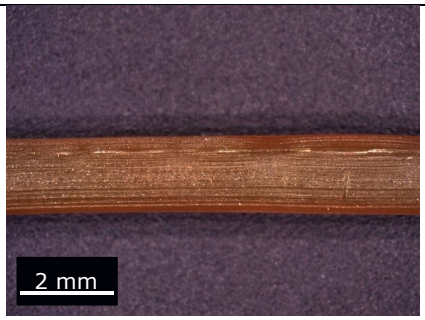
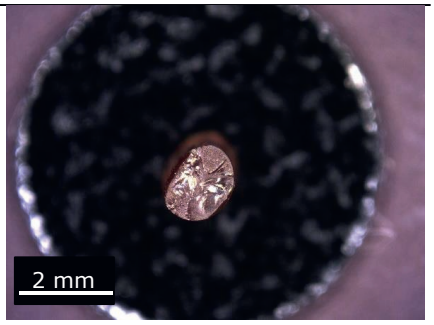
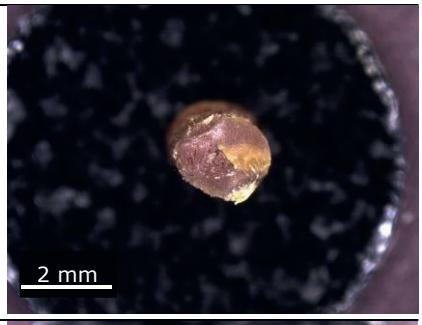
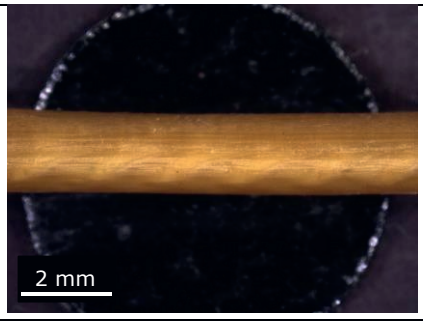
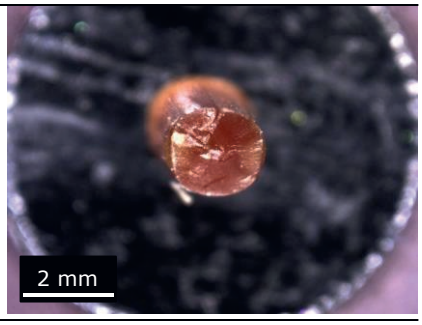
LA20		
G20		

Table A3.3 *Smartzoom microscope images (35x) of filaments containing 20% (w/w) of a OA:G blend (3:1, 1:1 and 1:3 ratio)*

Sample	Outer surface	Side profile
OA5/ G15		
OA10/ G10		

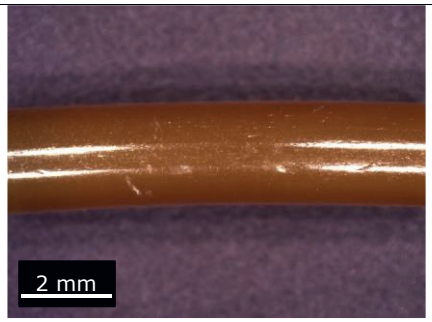
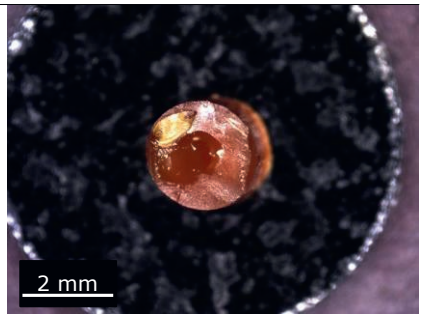
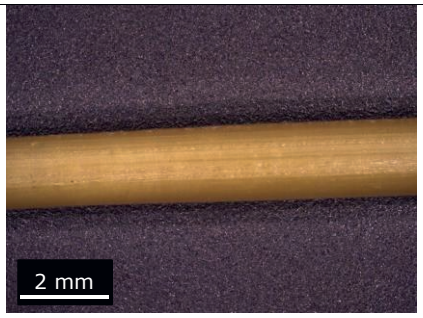
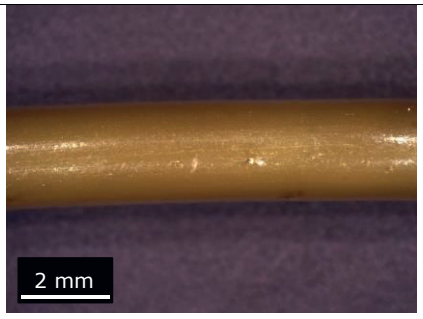
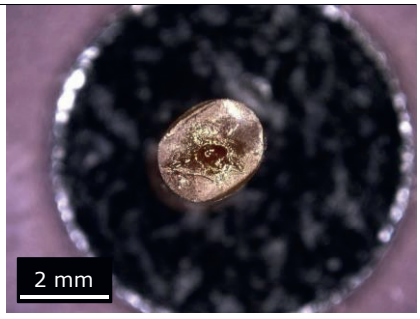
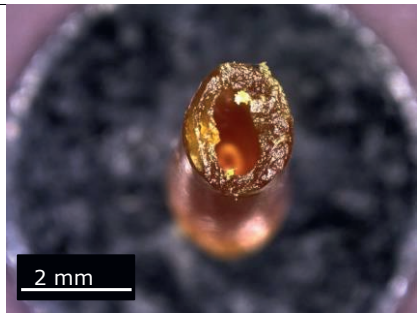
OA15 /G5		

Table A3.4 *Smartzoom microscope images (35x) of filaments containing 30% (w/w) of a OA:G blend (3:1, 1:1 and 1:3 ratio)*

Sample	Surface	Cross section
OA22.5 /G7.5		
OA15 /G15		
OA7.5 /G22.5		

A3.6 FDM print settings

Orcaslicer V2.3.0 was used to generate gcode. Default printer profiles (0.8 mm nozzle) for the sovol SV06 and bambulab P1S were imported from the repositories of Sovol and Bambulab respectively. Zein and PLA samples were printed on textured PEI build plates, whereas PETG samples were printed on a Bambulab engineering plate. Full slicer settings can be found within the provided .3mf file.

Table A3.5 *Process settings in OrcaSlicer for 3d printing*

Setting	Value
First layer height	0.4 mm
Layer height	0.24 mm
Line width	0.82 mm
Seam position	Nearest
Precise Z height	Enabled
Wall generator	Arachne
Wall print order	Outer/inner
Wall loops	5
Spare infill density	100%
Solid infill direction	0°
Rotate solid infill direction	Disabled
Flow rate zein	9 mm^3/s
Flow rate PLA	21 mm^3/s
Flow rate PETG-HF	21 mm^3/s

Table A3.6 *OA7.5/G22.5 filament calibration results with 0.8 mm nozzle*

Setting	Value
Print temperature	140 (limits: 140-160 °C)
Flow ratio	1.00
Max volumetric speed	9 mm^3/s
Printbed temperature	60 °C
Pressure advance	Disabled

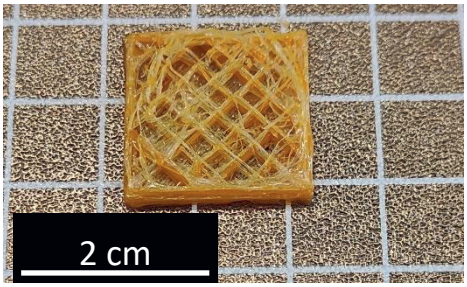


Fig. A3.6 *3d printed zein cube, showing infill lines with 0.8 mm nozzle. Squares on build plate represent 1x1 cm*

A3.7 Screw configuration continuous extrusion

During continuous extrusion the screw design was configured to optimise mixing action according to the layout below

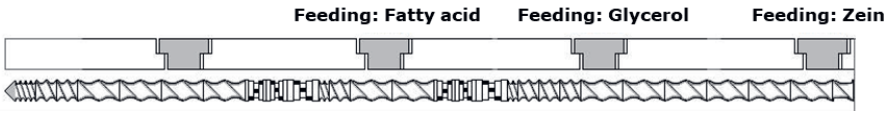
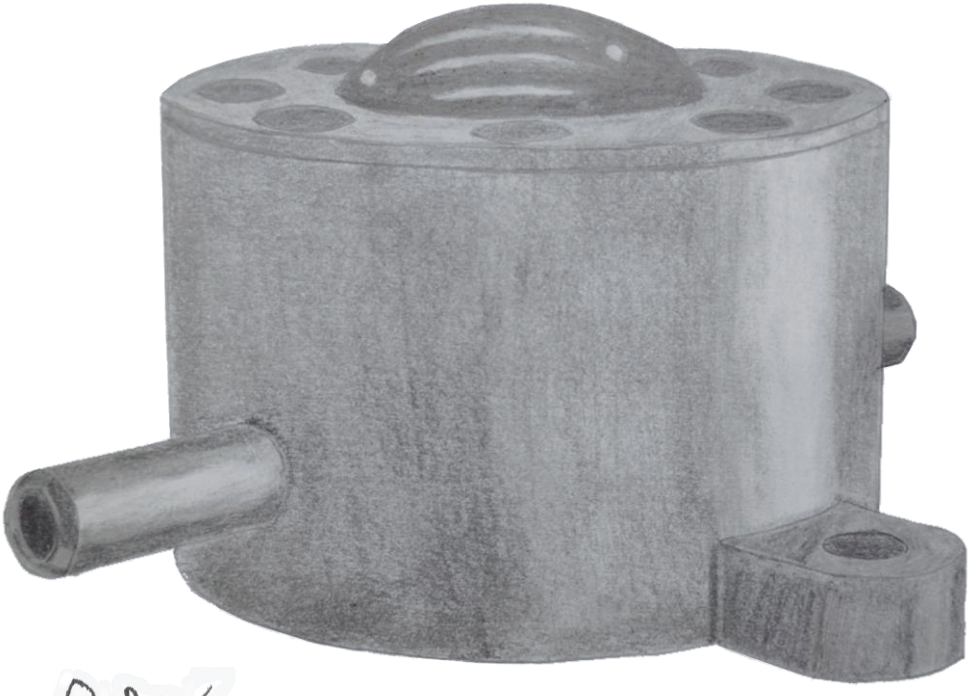


Fig. A3.7 Schematic overview of feeding zones and screw design during filament extrusion with Leistritz ZSE 18



Fig. A3.8 *One of the spools of filament produced on the continuous extrusion line*



Q 8 '26

Chapter 4

Mechanical characterization of elastic edible films with single, crosslinked and interpenetrating biopolymer networks using combined uniaxial and biaxial analysis

This chapter has been published as Steffens, Q., Gan Yu-Jing, D,. Schuppert, M,. Van der Sman, R.G.M., Boom, R. M., Zhang, L. (2026). Mechanical characterization of elastic edible films with single, crosslinked and interpenetrating biopolymer networks using combined uniaxial and biaxial analysis. *Current Research in Food Science*, 12, 101381. https://doi.org/10.1016/j.crfs.2026.101381

Abstract

Stretchable and compliant films can be prepared from edible biopolymers such as hydrocolloids and proteins. Their mechanical performance under stress affects their potential applications. This chapter investigates the uniaxial and biaxial extensional properties of various edible hydrogel films plasticized to various degrees. Hydrogel films consisting of single biopolymer networks (SN), crosslinked networks (CN) and interpenetrating networks (IPN) were prepared using gelatine, gelatine-caseinate and alginate-agar, respectively, with different concentrations of glycerol. Their extensional properties were characterized with computer-vision-based biaxial extension testing and compared to standard uniaxial tensile testing. The IPN films exhibited strain-hardening and the highest stiffness and tensile strength. Adding plasticizer reduced the stiffness of all film types and also reduced the tensile strength in SN and CN films. The influence of the plasticizer on the tensile strength of IPNs is governed by the architectures of the first and second networks. While standard, uniaxial extension of IPN films showed no relation between glycerol content and fracture properties, our biaxial methods showed that plasticization by glycerol reduced both fracture strain and stress. Our results highlighted the necessity of combining uniaxial and biaxial tensile tests to evaluate film properties for practical applications relying on different types of stress load. The insight obtained may be used to design edible films with improved extensional performance, and our biaxial method could potentially be used as a screening tool for evaluating tensile properties in novel materials.

Nomenclature

a, b	Half-major and half-minor axis length of ellipse (m)
A, A_0	Instantaneous and initial cross-sectional area (m^2)
F	Force (n)
h, h_0	Instantaneous and initial gauge length (m)
h_b	Bulge height from the film clamp to the apex of the bulge (m)
K	Strength coefficient (Pa)
n	Strain hardening exponent (-)
p	Pressure (Pa)
R_1, R_2	Radius of curvature (m)
S, S_0	Instantaneous and initial film thickness (m)
$\varepsilon_1, \varepsilon_2$	True strains in principal directions 1 and 2 (-)
ε_3	True thickness strain (-)
σ_1, σ_2	True principal stresses in principal directions 1 and 2 (Pa)
σ_B	Equi-biaxial true stress (Pa)
a, b	Half-major and half-minor axis length of ellipse (m)
A, A_0	Instantaneous and initial cross-sectional area (m^2)

4.1 Introduction

Growing concerns from consumers and governments about sustainability and safety of plastics films based on petroleum-derived polymers have caused increasing interest in the development of polymer films based on edible materials (Khalesi et al., 2020; Leceta et al., 2014; Yin et al., 2024). Although edible films have excellent biodegradability and biocompatibility, their mechanical performance requires further improvement (Hartmann et al., 2021; Nath et al., 2022; Walker et al., 2017; Wittaya, 2012). Adoption of edible films in food and pharmaceutical packaging, tissue engineering, and soft robotics, requires a better assessment of their elasticity and tensile strength.

Mechanical properties of edible films, such as elasticity and tensile strength, are affected by the type of polymer network and can be modulated by plasticization. Edible single network (SN) films contain a single film-forming biopolymer, such as a protein or a hydrocolloid. Single-network biopolymers generally exhibit limited stretchability, with gelatine being a notable exception due to reversible crosslinking by triple helices that can dissipate stresses during stretching (Baumgartner et al., 2020; Edward and Golecki, 2023; Shintake et al., 2017). Crosslinked network (CN) films contain at least two film-forming polymers with a single, intermolecularly (often covalently) crosslinked network that improves the film elasticity and robustness (Guo et al., 2014; Khalesi et al., 2020). Interpenetrating polymer network (IPN) films also contain at least two polymers, but these are sequentially crosslinked to form two distinct polymer networks that are molecularly intertwined but not covalently bonded, resulting in enhanced strength and flexibility by combining a rigid network with a soft, sacrificial one (Bootsma et al., 2017; Jeong et al., 2020; Lin et al., 2019; Suo et al., 2018). The polymer networks can be formed by hydrocolloids, which contain many hydroxyl groups and

often are polyelectrolytes as well (e.g. alginate), fibrous proteins such as gelatine, and globular proteins such as casein (Baumgartner et al., 2020; Edward and Golecki, 2023; Janes and Dai, 2012; Khwaldia et al., 2004).

The mechanical properties of films can be further modified by incorporation of plasticisers. Plasticisers enhance the chain mobility, which increases the maximum strain at break but often also reduces the tensile strength and Young's modulus (Gao et al., 2017; Lawton, 2004; Yoo and Krochta, 2011). Glycerol is particularly effective but may compromise the gel stability (L. Li et al., 2018). Plasticisers may also improve the compatibility between multiple polymers, enhancing the physical stability of DN and IPN films (Brindle and Krochta, 2008; L. Li et al., 2018). Thus, there are many variables affecting the mechanical properties of edible films and optimizing mechanical properties for specific applications is therefore not trivial. Quantitative evaluation of mechanical properties may help to accelerate the formulation development.

To evaluate the effect of the network structure and plasticizer content on the tensile properties of edible thin films, characterization of the extensional properties can be performed by applying a load to a sample and measuring its stress-strain response in tensile tests. Small deformation properties such as Young's modulus and large deformation properties such as tensile strength and elongation at break can be obtained from standardized uniaxial tensile tests (Kozempel and Tomasula, 2004; Yoo and Krochta, 2011). However, in practical applications, polymer films generally undergo biaxial deformation. For example, packaging films typically are wrapped/spread over and around a product and in that process are extended biaxially. Despite this, a comprehensive comparison between the influence of plasticizer content and

network type on the uniaxial versus biaxial tensile properties of edible films has not yet been reported.

Biaxial deformation can be characterized using a bulge test, which involves fixating a circular film over a cylindrical pressure chamber and deforming the film by applying a pressure difference over the film. This pressure differential causes biaxial deformation, which in turn can be quantified using an optical measurement system, and related to the momentary pressure difference. Thus, a force-deformation curve can be obtained, which can be converted to a stress-strain curve and compared to uniaxial testing. Since the stress distribution over a thin film is fundamentally different for uniaxial and biaxial deformation, the force-deformation curves are different as well, and since applications typically involve biaxial deformation, it is important to investigate this difference. Biaxial loading also allows the use of larger strain ranges before material failure (Ebrahimi and Lotfabad, 2022; Hallfeldt et al., 2014). Combining uniaxial with biaxial tensile tests is thus beneficial as this provides a more complete characterization of film properties.

Therefore, this study investigates the tensile properties of edible films using uniaxial and biaxial tensile tests, on a range of different films, by varying the type of polymeric network and the degree of plasticization. Edible films based on gelatine, gelatine-caseinate, and alginate-agar represent the three network types, SN, CN, and IPN, and were each formulated with a range of plasticizer levels. Standardized uniaxial tensile test were performed to determine the small and large extensional properties using a universal testing machine. A standardized biaxial tensile tester known as the alveograph is used in the food industry to measure empirical dough properties as indicators of flour quality (Dufour et al., 2024; Jødal and Larsen, 2021). However, alveographs do not provide full stress-strain curves. Therefore, a bulge-test based method was

developed to characterize the biaxial tensile properties of the films. This computer-vision based method includes a novel image processing and analysis workflow to convert pressure-deformation data to full stress-strain curves. Finally, the large deformation properties obtained using uniaxial and biaxial tests were compared to provide comprehensive insight on the tensile properties of edible films. The approach described in this study may serve as the basis for future investigations aiming to inform the design of edible polymer films with mechanical properties optimised for packaging, tissue engineering and soft robotics.

4.2 Materials & Methods

4.2.1 Materials

Agar, calcium chloride dihydrate (purity >99%), citric acid (purity ≥ 97%) and sodium alginate were purchased from Sigma-Aldrich (Zwijndrecht, the Netherlands). Gelatine (bloom value 116) and glycerol (purity 99.6%) were obtained from VWR Chemicals (The Netherlands). Microbial transglutaminase (Activa WM, nominal activity 100U/g) was purchased from Ajinomoto (Nesle, France). Sodium caseinate (dry matter content of 48.5% w/w) was provided by FrieslandCampina (Wageningen, The Netherlands). Food colouring (Wilton) and glucose syrup (Brand New Cake) were purchased from online retailers.

Table 4.1 *Formulations of edible films: single network (SN), crosslinked network (CN), and interpenetrating network (IPN)*

	SN: Gelatine			**CN: Gelatine-Caseinate**			**IPN: Alginate-Agar ****			
Component (%/w/w) *	***G23***	***G29***	***G34***	***GC5***	***GC10***	***GC15***	***AA5***	***AA10***	***AA15***	***AA20***
Deionized water	34	28	23	72	77	82	76	81	86	91
Glycerol	23	29	34	5	10	15	5	10	15	20
Glucose syrup	25			-			-			
Gelatine	14			1.6			-			
Citric acid	3.6			-			-			
Caseinate	-			10			-			
Microbial transglutaminase	-			0.9			-			
Alginate	-			-			0.9			
Agar	-			-			3.0			

* weight percentage of each component in the film forming solutions (i.e. before drying/casting of the film)

** $CaCl_2$ solution was used to crosslink alginate

4.2.2 Edible film preparation

Edible films with three types of network structures were prepared by preparing film forming solutions, drying and conditioning.

Solutions to prepare single-network (SN) gelatine films were formulated as reported by Baumgartner (2020). Three samples were prepared using 23, 29 and 34% (w/w) glycerol as plasticizer and were abbreviated as G23, G29, and G34, respectively (Table 4.1). First, citric acid (3.6% w/w), glucose syrup (25% w/w), and glycerol were dissolved in deionized water at 70 °C under continuous stirring at 400 RPM for at least 1 hour. Afterwards, the solution was cooled to 25 °C. Second, gelatine was added while the solutions were stirred at 50 RPM for at least 1 hour. The solution was then heated to 70 °C

at 400 RPM and immediately deaerated in a vacuum mixer (ARV-310P, Thinky, Japan) at 2350 rpm, 350 mbar for 2 min.

Solutions to prepare crosslinked-network (CN) edible films were formulated using conjugates of gelatine and sodium caseinate as described by Chambi and Grosso (2006). Three sample were prepared using 5, 10, and 15% (w/w) glycerol as plasticizer, which were abbreviated as GC5, GC10, and GC15, respectively (**Table 4.1**). Gelatine (1.6% w/w) was hydrated in deionized water at room temperature for at least 1 hour. Subsequently, sodium caseinate (10% w/w) and glycerol were added while the mixture was stirred at 400 RPM and 60 °C for an hour. Microbial transglutaminase (0.88% w/w) was added to crosslink for 15 min and deactivated by heating to 85 °C. A sample solution of GC10 without transglutaminase was prepared as a control to verify whether the crosslinking was successful in other samples.

The solutions to prepare SN and CN edible films were stained with a black dye, subsequently poured into petri dishes coated with sunflower oil as release agent and dried in a fume hood for 24 hours.

Solutions to prepare interpenetrating-network (IPN) films were formulated using composites of sodium alginate and agar as described by Li et. al (2018). Four levels of glycerol (5, 10, 15, and 20% w/w) were used as plasticizer. Four sample were prepared using 5, 10, 15 and 20% (w/w) glycerol as plasticizer, which were abbreviated as AA5, AA10, AA15 and AA20, respectively (**Table 4.1**). Sodium alginate (0.9% w/w), agar (3% w/w), a black dye and glycerol were dissolved in deionized water at 95 °C under continuous stirring at 400 RPM for at least 1 hour (**Table 4.1**). The solutions were poured directly into a petri dish coated with sunflower oil and dried for 24 hours inside a fume hood. Next, 1M $CaCl_2$ solution was poured onto the dried films to crosslink the sodium alginate for 4 hours. After the treatment,

the films were taken out of the petri dishes and any excessive liquid were removed with paper towel. A sample solution of AA10 for which $CaCl_2$ steeping was omitted was prepared as a control to verify whether IPN formation was successful in other samples.

Prior to mechanical testing, all films were conditioned at 20 °C and 50% relative humidity until the mass loss between subsequent measurements at 24 hours intervals was less than 1%.

4.2.3 Uniaxial tensile testing

Dog bone shaped samples (n = 5 per sample) as defined by ISO 527-2 shape 1BA were cut from conditioned films using a hydraulic press (**Fig. 4.1**). The sample thickness and width were measured at the end and middle of the rectangular section of the samples using a digital calliper to calculate the cross-sectional area of the sample (Mitutoyo Manufacturing Co. Tld., Japan). Uniaxial tensile tests were performed using a Zwick Z010 tensile tester according to ISO 527-2 protocol. The tester was equipped with pneumatic grips (type 8195) with integrated control valves to maintain constant pressure during testing. A load cell of 100N was used and the initial clamp distance was set to 55 mm. The strain was measured using a clip-on extensometer that contacted the sample at two points 25 mm apart. The testing speed was 100 mm/min, with the exception of the IPN samples where the testing speed was reduced to 10 mm/min due to the high tensile strength of the samples.

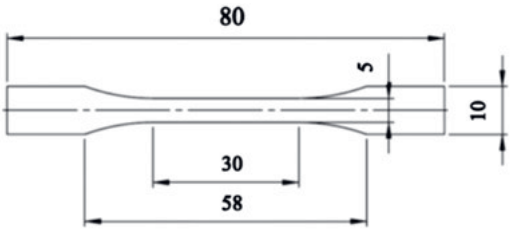


Fig. 4.1. *Dimensions (in mm) of samples used for uniaxial tensile testing.*

The force and displacement were recorded with the testXpert software (Zwick Roell, Venlo, The Netherlands). True stress σ_{True} (Pa) was calculated under the assumption of incompressibility as

$$\sigma_{True} = \frac{F}{A} \qquad \textit{Eq. 4.1}$$

With F the force (n) and A the area (m^2). The cross-sectional area is dependent on the instantaneous elongation and is given by

$$A = \frac{h_0}{h} A_0 \qquad \textit{Eq. 4.2}$$

With h_0 the initial gauge length (mm), h the current gauge length and A_0 the initial cross-sectional area of the sample (mm^2). The true strain ε_{True} (-) was calculated as

$$\varepsilon_{True} = \ln\left(\frac{h}{h_0}\right) \qquad \textit{Eq. 4.3}$$

Young's modulus was calculated as the slope of the stress-strain curve in the linear elastic region between 0.05 and 0.5% of strain (for statistical details, refer to 'Young's modulus' section of the Supplementary Materials). Strain

and stress at break were determined at the peak stress of the true strain-stress curve.

The true strain and stress during plastic deformation were fitted to the Hollomon Law:

$$\sigma_{True} = K\ \varepsilon_{True}^{n} \qquad \textit{Eq. 4.4}$$

With K the strength coefficient (Pa) and n (-) the strain hardening exponent (Ebrahimi and Lotfabad, 2022; Li et al., 2019).

4.2.4 Biaxial bulge testing

4.2.4.1 Bulge test principles and deriving true stress-strain curves

Biaxial deformation is a different phenomenon relative to uniaxial deformation, and thus it is useful to investigate this, next to uniaxial deformation. Bulge testing is however also advantageous over uniaxial testing as it allows the characterization of materials exhibiting significant plastic deformation, since higher strain levels can be achieved before fracture occurs and the method is less sensitive to necking (Dudderar et al., 1977; Ebrahimi and Lotfabad, 2022; Güner et al., 2009; Kaya et al., 2008). However, reports of bulge tests on (edible) soft films are scarce, despite their relevance to applications in for example packaging, tissue engineering, and soft robotics (Huang et al., 2007).

In bulge testing a flat film of a sample is fixated onto a die having a circular orifice and clamped around the perimeter using a sample holder (**Fig. 4.2**). An elevated pressure p is gradually applied to one side of the sample, causing it to bulge to the other side. As the test conditions are nearly frictionless, the true stress at the apex of the bulge can subsequently be calculated from the applied pressure, the local radius of curvature and the thickness of the sample

(raw data are provided in the ‘Film thickness’ section of the Supplementary Materials).

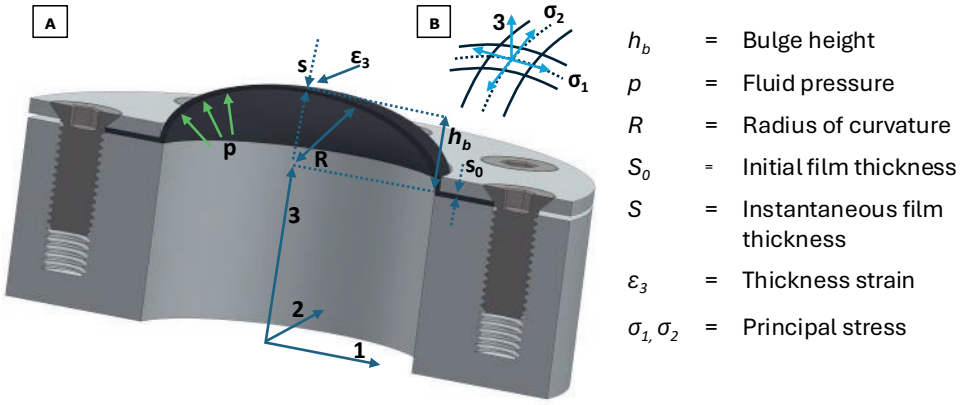


Fig. 4.2 *A) Schematic representation of a section of a deformed sample clamped in the bulge test setup B) Direction of principal stresses* σ_1 *and* σ_2 *at the apex of the bulged film*

The local radius of curvature can be derived from images captured with a sideways camera as function of time (Hallfeldt et al., 2014; Mulder et al., 2015; Stachowicz and Rzeszowska, 2003). However, in-situ measurement of the local thickness of films at their apex during bulge testing is not trivial. Different relations for deriving the local thickness at the film apex as function of local deformation have been proposed (Min et al., 2017). These are based on geometric constraints or on empirical observation, e.g. by freezing bulged samples (Charalambides et al., 2002; Ebrahimi and Lotfabad, 2022; Kruglov et al., 2002; Lazarescu et al., 2011; Stachowicz and Rzeszowska, 2003).

To derive the local thickness of the apex it is often assumed that the deformation is uniform over the bulge, in which case the bulge shape can be approximated by a sphere (Charalambides et al., 2002; Hallfeldt et al., 2014; Hill, 1950). However, at the perimeter, the film is constrained by a clamp, and as such can only deform uniaxially in the direction orthogonal to the

perimeter. At the apex of the bulge, the film is stressed purely biaxially and is thus stretched thinner than at the rim. Therefore its not expected that the bulge will be purely spherical; an extra degree of freedom is required during fitting of the bulge shape to accommodate for these constraints. During bulge testing of metals, a superior fit was provided with a spheroid (an axisymmetric ellipse) compared to a sphere (an axisymmetric circle), which provides an extra degree of freedom (Ebrahimi and Lotfabad, 2022; Kaya et al., 2008; Mulder et al., 2015). Due to the axial symmetry, the principal curvatures R_1 and R_2 (**Fig. 4.2**) at the apex are equal and the film deforms equibiaxially, and thus the stress in both principal directions around the apex must be equal: $\sigma_1 = \sigma_2 = \sigma_B$ (Hallfeldt et al., 2014; Mulder et al., 2015). Min et. al showed that even if R_2/R_1 is larger than ~0.5 the stress ratio σ_2/σ_1 is still larger than 0.99, as long as the radius of principal curvature is >50 times larger than the film thickness (2017). For this equibiaxial stress state at the apex, the force equilibrium equation for thin shells equals (Mulder et al., 2015; Stachowicz and Rzeszowska, 2003):

$$\sigma_b = \frac{pR}{2s} \qquad \textit{Eq. 4.5}$$

With σ_b the biaxial true stress (Pa), p (Pa) is the pressure, R the curvature radius (m), and s the thickness of the film (m). The radius of curvature at the bulge apex is given by:

$$R_1 = \frac{b^2}{a} \qquad \textit{Eq. 4.6}$$

With b the semi-minor axis length (m) and a the semi-major axis length (m) as determined from the ellipse fit during the bulge test (**Fig. 4.3B**).

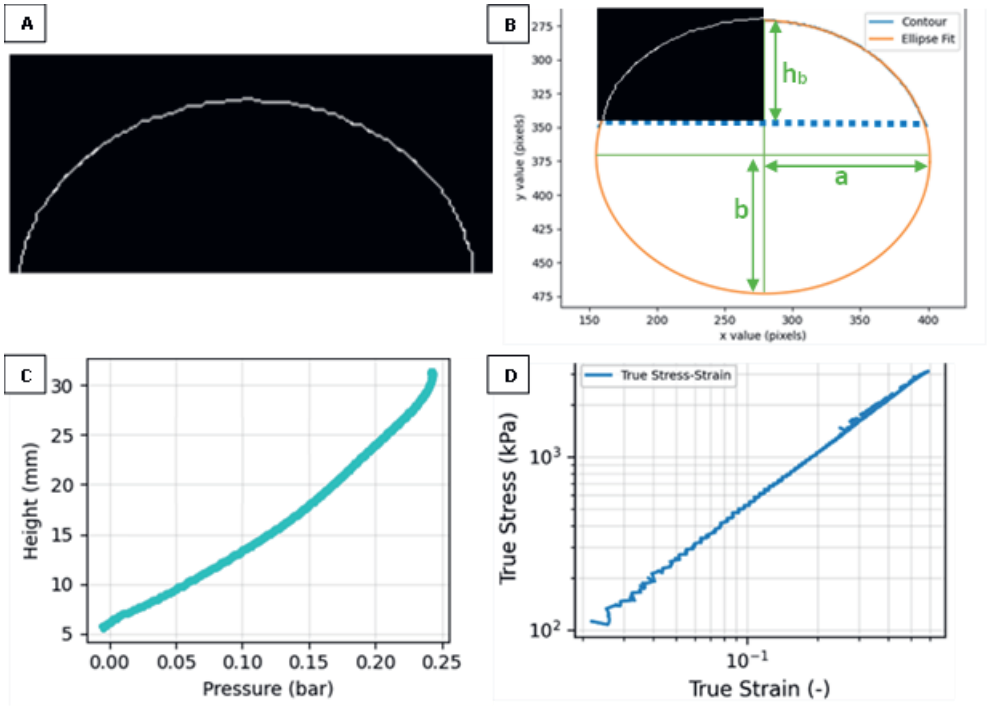


Fig. 4.3 *A) Bulge outline frame after application of filtering steps; B) Ellipse fit generated during image processing, with the left half of the frame from A overlaid as visual guide. The bulge outline is represented by a blue line, the fitted ellipse by an orange line and the film clamp by a dashed blue line. The green arrows indicate the major axis 2a, the minor axis 2b and the height h_b from the film clamp to the apex of the bulge; C) Pressure-height curve of a representative sample; D) True stress-strain curve of the same representative sample.*

Because of volume preservation, the true through-thickness strain ε_3 equals (Hallfeldt et al., 2014):

$$\varepsilon_3 = \ln\left(\frac{s}{s_0}\right) = -(\varepsilon_1 + \varepsilon_2) \qquad \textit{Eq. 4.7}$$

With ε_3 the true strain (-) and s_0 the thickness of the film in unstressed state. Thus we can calculate the instantaneous film thickness as (Charalambides et al., 2002; Min et al., 2017):

$$s = s_0 e^{-(\varepsilon_1+\varepsilon_2)} = s_0 e^{-2\varepsilon_b} \quad \textit{Eq. 4.8}$$

By combining equations 4.5 and 4.8, a relation between the biaxial strain and stress is obtained:

$$\sigma_b = \frac{pR}{2s_0} e^{2\varepsilon_b} \quad \textit{Eq. 4.9}$$

Mulder et. al (2013) proposed that the strain hardening exponent from the Hollomon law (equation 4.4, $\sigma_{True} = K \cdot \varepsilon_{True}^n$), obtained by uniaxial testing, may be used to calculate ε_b. We borrowed inspiration from this idea. The von-Mises equivalent true strain $\bar{\varepsilon}$ can be used to predict the stress under biaxial loading conditions from uniaxial tensile test data. With $\varepsilon_1 = \varepsilon_2 = \varepsilon$ and $\varepsilon_3 = -2\varepsilon$ the von-Mises strain equivalent true strain $\bar{\varepsilon}$ becomes (Rees, 1995):

$$\bar{\varepsilon} = \sqrt{\frac{2}{3}[(\varepsilon_1 - \varepsilon_2)^2 + (\varepsilon_2 - \varepsilon_3)^2 + (\varepsilon_3 - \varepsilon_1)^2]} \quad \textit{Eq. 4.10}$$

$$= \sqrt{\frac{2}{3}(18\varepsilon_2)} = 2\sqrt{3}\varepsilon$$

For the von-Mises equivalent stress $\bar{\sigma}$ we can again use $\sigma_1 = \sigma_2 = \sigma$. The plane stress $\sigma_3 \approx 0$, so the von-Mises equivalent stress becomes:

$$\bar{\sigma} = \sqrt{\sigma^2} = \sigma \quad \textit{Eq. 4.11}$$

Therefore

$$\sigma = \bar{\sigma} = \mathrm{K}\,\bar{\varepsilon}^n = K(2\sqrt{3})^n \quad \textit{Eq. 4.12}$$

To determine the strain at which the applied membrane stress equals the material's flow stress we can equate equations 4.9 and 4.12 to obtain:

$$\frac{pR}{2s_0}e^{2\varepsilon} = K(2\sqrt{3})^n \qquad \textit{Eq. 4.13}$$

4.2.4.2 Bulge test setup and data acquisition

Biaxial bulge tests were performed using an in-house developed experimental setup based on the pneumatic bulge test principle. At least 2 samples were tested per film type. Film samples were cut into circular specimens (37 mm diameter) and mounted onto the pressure chamber using a clamping ring fastened with 8 screws (**Fig. 4.2**). During preliminary experiments, samples were marked with concentric circles to monitor possible slippage. Torque applied to clamping screws was increased between successive trials until slippage was no longer observed at an applied torque of 0.4 Nm per screw. This torque was subsequently applied during all experiments and it was assumed that the films did not slip during the biaxial bulge test. During testing, the air pressure of chamber was continuously increased at a rate of 0.04 bar/s until the sample burst, taking 2-4 minutes depending on sample type. This slow testing velocity was chosen to prevent strain-rate dependent deviations between measurements. The pressure was monitored via a set of an inlet pressure controller (Bronkhorst, IN-PRESS P-5X2CI+F-0XXAI) and an outlet pressure controller (Bronkhorst, IN-PRESS F-0XXAI+P-5X2CI). The pressure was digitally controlled and recorded by the Bronkhorst software suite (FlowDDE, FlowView). Videos of bulge test were simultaneously recorded at 25 frames per second using a Sony FDR-AX53 4K video camera.

4.2.4.3 Data pre-processing and synchronization

During video processing, computer vision algorithms from the OpenCV library were utilised to extract the contour of the bulge. A pixel-to-millimetre conversion factor was established using a still image of a ruler placed on the same plane as the bulge.

To extract the bulge contour, each frame was first converted to greyscale and subjected to a mild Gaussian blur with a kernel size of 5 by 5 pixels to attenuate sharp edge transitions. A binarization filter was then applied with a saturation threshold with a default value of 80, which was adjusted such that the bulge shape was well defined in all frames. These intermediate binary images were subsequently processed using morphological dilation followed by skeletonization, ensuring that the bulge outline was represented as a continuous, single-pixel-wide line (**Fig. 4.3A**). The detected bulge outline was fitted to an ellipse (**Fig. 4.3B**) using a least-squares fit.

$$RMSE = \frac{\sum_{i=1}^{N}(d_i)^2}{N} \qquad \textit{Eq. 4.14}$$

With N the number of data points used to fit each frame, and d_i the shortest distance from the i-th data point to the fitted ellipse (Min et al., 2017).

The parameters derived from the fitting procedure include the coordinates of the ellipse centre, the bulge height h_b relative to the fixation point, and the lengths of the semi-major and semi-minor axes a and b (**Fig. 4.3B**). The bulge outline was processed frame by frame to extract the deformation over time. The deformation data were synchronised with the pressure data (**Fig. 4.3C**) and saved for subsequent calculations. Data was processed using a custom-written python script using the OpenCV, skimage and numpy packages (Supplementary Material).

4.2.4.4 Data analysis

Prior to tensile testing, the sample thickness (s_0) was measured at three evenly distributed locations over the film surface using a digital calliper (Mitutoyo Manufacturing Co. Tld., Japan). Since the film thickness during bulging could not be determined experimentally, a residual function was derived from **equation 4.13**:

$$f(\varepsilon) = \frac{pR}{2s_0} e^{2\varepsilon} - K(2\sqrt{3})^n \qquad \text{Eq. 4.15}$$

This residual function was solved numerically to find the strain at which the applied membrane stress equals the material's flow stress. This equilibrium strain was then used to calculate the film thickness and stress at the apex using **equations 4.8 and 4.5** respectively. The numerical solver employed adaptive bracketing followed by Brent's root-finding method. By repeating this analysis for each frame, true strain-true stress curves were obtained (**Fig. 4.3D**).

4.2.4.5 Statistical analysis

Statistical analysis was performed using the numpy (v2.2.4) and scipy (v1.15.2) packages in Python (v3.13, Python Software Foundation, USA).

4.3 Results & Discussion

4.3.1 Formation of crosslinked and interpenetrating networks

To confirm the effectiveness of transglutaminase-induced crosslinking in GC samples, a GC10-reference sample was prepared for which the crosslinking step was omitted. This sample had poor mechanical properties compared to the GC10 sample, confirming that the crosslinking step improved the mechanical integrity (data not shown). Similarly, a AA10-reference sample was prepared in which the formation of the IPN through steeping in $CaCl_2$

was omitted. The AA10 sample had significantly improved mechanical properties and thus it is evident that an IPN is indeed formed. No directionality was observed in the IPN samples when studied under a polarizing optical microscope (Zeiss AxioScope 5, Germany).

4.3.2 Uniaxial tensile properties

4.3.2.1 Elasticity

When a stress is applied to a material, it initially deforms elastically. Elastic deformation is reversible and characterized by a linear relationship between applied stress and observed strain. A material's elasticity is quantified by its elastic modulus, or Young's modulus, which is defined as the slope of the stress-strain curve within the elastic regime.

SN films had the lowest Young's modulus among the tested films, ranging from 85 to 180 kPa (**Fig. 4.4A**). Baumgartner et al. (2020) investigated SN gelatine hydrogels similar to those prepared for this study and reported Young's modulus values of 30-300 kPa, depending on the gelatine content. Young's moduli of other SN films made with gelatine, agarose or non-edible polymers were in the range of 12-500 kPa (Hur et al., 2014; Smith et al., 2024; Sun et al., 2024; Suo et al., 2018). SN films made with gelatine are physically crosslinked by triple helical junction zones, with hydrogen bonding, ionic bonds and hydrophobic interactions between polymer chains but lacking stronger bonds such as covalent bonds (Poveda-Reyes et al., 2015; L. Zhang et al., 2019). In general, polymers in SN are weakly associated and thus do not provide much resistance to elongation (Clark, 1996). This is evident in the small Young's moduli of the SN films.

Due to their poor mechanical integrity, the GC15 films could not be analysed. Young's moduli of other CN films were an order of magnitude higher than those of SN films, ranging from 260 to 2400 kPa (**Fig. 4.4B**). For CN films

based on non-edible polymers, Young's moduli between 122 and 5310 kPa have been reported, which matches well with our observations (Lin et al., 2015; Liu et al., 2018; Zheng et al., 2020; Zhu et al., 2018). As polymer chains are covalently crosslinked in CN films, more resistance to uniaxial elongation is expected compared to SN films. In our CN films, covalent bonds between proteins, peptides and primary amines were introduced through the transglutaminase-catalysed formation of ϵ-(γ-glutamyl)-lysine crosslinks within and in between gelatine and casein proteins via an acyl transfer reaction (Chambi and Grosso, 2006; Yildirim and Hettiarachchy, 1998).

The Young's moduli of IPN films were an order of magnitude higher than CN films, ranging between 11600 and 39000 kPa (**Fig. 4.4C**). The literature does not report on any edible IPN films, but a broad range of Young's modulus values for non-edible IPN films has been reported, ranging from 1171 kPa to 19000 kPa (Myung et al., 2007; Panteli and Patrickios, 2019; Zhou et al., 2020). In IPN films, two independent polymer networks are intertwined which increases the overall resistance to stretching compared to SN and CN films (Niu et al., 2019; Panteli and Patrickios, 2019; Suo et al., 2018). The crosslink density of the primary network governs the available free volume and the strain dissipation capacity for the secondary network (Lin et al., 2019; Suo et al., 2018), which explains why a wide range of Young's moduli is reported in literature.

Despite the differences in Young's modulus at low plasticizer content of SN, CN and IPN films, increasing plasticizer content always led to a strong reduction in Young's modulus across all film types, making films more flexible and less stiff (**Fig. 4.4**). This finding is consistent with reported reductions in Young's modulus for plasticized films composed of zein, alginate, pea protein and various synthetic plastics (Choi and Han, 2001; Gao

et al., 2017; Lawton, 2004; Sears and Darby, 1982). Liu et al. and Carvalho reported a negative linear correlation between Young's modulus and the glycerol content of gelatine films (de Carvalho and Grosso, 2004; Liu et al., 2017). Both studies reported a similar effect after inducing crosslinking using transglutaminase, thus matching our observation for SN and CN films. A decrease in Young's modulus as result of plasticizer addition has also been reported for IPNs based on acrylic elastomers (Zhang et al., 2010).

The effects of plasticizers on polymer networks can be attributed to their ability to form hydrogen bonds with polymer chains, replacing intermolecular bonds between polymer chains and increasing the available free volume in the polymer network (Eslami et al., 2023). In the elastic region, over which the Young's modulus is calculated, only reversible deformation occurs. The effect of cross-linkages or interpenetrating networks on deformation behaviour is therefore limited in the elastic region, which explains why the influence of plasticizer content is the same for SN, CN and IPN networks.

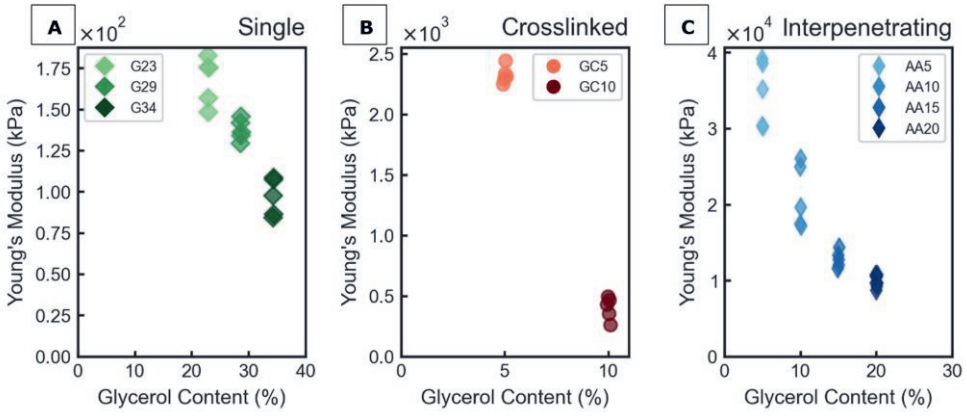


Fig. 4.4 *Young's modulus as function of glycerol content for single network films (A), crosslinked network films (B) and interpenetrating network films (C) obtained from uniaxial tensile tests: results of technical replicates are shown*

4.3.2.2 Tensile strength

Once a material is stressed beyond its linear elastic regime, it will cross its yield point and enter the plastic regime. Stress applied in the plastic regime changes the microstructure of the material, causing irreversible deformation that persists after removal of the load. Upon further tensile deformation a material will eventually fracture. The strain and stress at the point at this breaking point define a materials tensile strength.

The uniaxial tensile tests revealed the fracture behaviour of the SN, CN and IPN films. The true stress at break ranged from 47-1300 for SN films, to 95-2200 for CN films and 4400-8100 kPa for IPN films, depending on plasticizer content (*Fig. 4.5*). For gelatine and polyacrylamide SN films, true stress at break values of 18-406 kPa were reported which aligns with our observations (Myung et al., 2007; Suo et al., 2018). For CN films, true stress at break values of 4500-25000 kPa have been reported, which is much higher than for the GC5 and GC10 films (Chambi and Grosso, 2006; Lin et al., 2015; Zhao et al., 2024). Finally, IPN films are reported to have stress at break values of 5000-40000 kPa, with the lower end of that range matching our observations (Hwang et al., 2024; Xu et al., 2021; Yan et al., 2017; Yang et al., 2017; Zhou et al., 2020).

IPN films can withstand much higher stresses before failing compared to SN and CN films. As IPNs consist of a primary polymer network that is covalently crosslinked and a secondary polymer network that is ionically (i.e., physically) crosslinked, stresses on IPN films are distributed over two networks. Stresses can be dissipated by fission of the ionic crosslinks, while the covalent crosslinks remain intact (Bootsma et al., 2017; Sun et al., 2012). At larger deformations, this also prevents cracks from propagating into large ruptures (Chen et al., 2014).

Plasticisation of SN and CN films with glycerol resulted in decreased fracture strain and stress (**Fig. 4.5A and Fig. 4.5B**). In contrast, the fracture strain of the alginate-agar IPN film remained unaffected by glycerol addition, and its fracture stress was only reduced between 5% and 10% w/w glycerol content, with no further change observed upon additional plasticiser incorporation (**Fig. 4.5C**). A reduction in fracture stress with increasing plasticizer content has been reported for zein, alginate film and pea protein films, but contrary to our observations this is most often accompanied by an increase in fracture strain (Chambi and Grosso, 2006; Choi and Han, 2001; Gao et al., 2017; Lai and Padua, 1997; Lawton, 2004).

A reduction in the strain at break with increasing plasticizer content could be caused by segregation of the plasticizer during the drying of the films or incompatibility of the plasticizer and polymer (Gao et al., 2017; Rusli, 2017). Gelatine, agar and alginate have good compatibility with glycerol at relatively lower plasticizer concentrations (Basu et al., 2022; Bhatia et al., 2024; Rusli, 2017). However, when the plasticizer concentration becomes very high, it is likely that phase segregation occurs during drying of cast films. Phase segregation creates regions in the film filled only or mostly by plasticizer, forming pores from which cracks may propagate when the film is stressed (Gao et al., 2017). This could explain the observed reduction in strain at break with increasing levels of plasticizer in SN films in this study (**Fig. 4.5**). Furthermore, measured strain at break for CN films was reduced with higher glycerol content. Both GC5 and GC10 possess poor mechanical strength compared to literature reports for CN films, while GC15 was too fragile to test for its mechanical properties. It has been reported in literature that casein has low compatibility with glycerol and may phase-separate during drying, resulting in distinct regions composed rich in glycerol (Chambi and Grosso, 2006). Such regions can create pores in the film, weakening its mechanical

strength. We even observed formation of some small droplets on the surface of GC15 films after drying, which is indicative of phase separation. Finally, Rusli et. al investigated SN films with 1-3% agar and 5-15% glycerol and found that the glycerol concentration did not significantly affect fracture strain or fracture stress during uniaxial extension. A similar trend can be observed for the agar-alginate IPN (Fig. 4.5). The fracture behaviour of the IPN under uniaxial extension therefore appears to be governed by the stiff agar network, with minimal contribution from the more ductile alginate network.

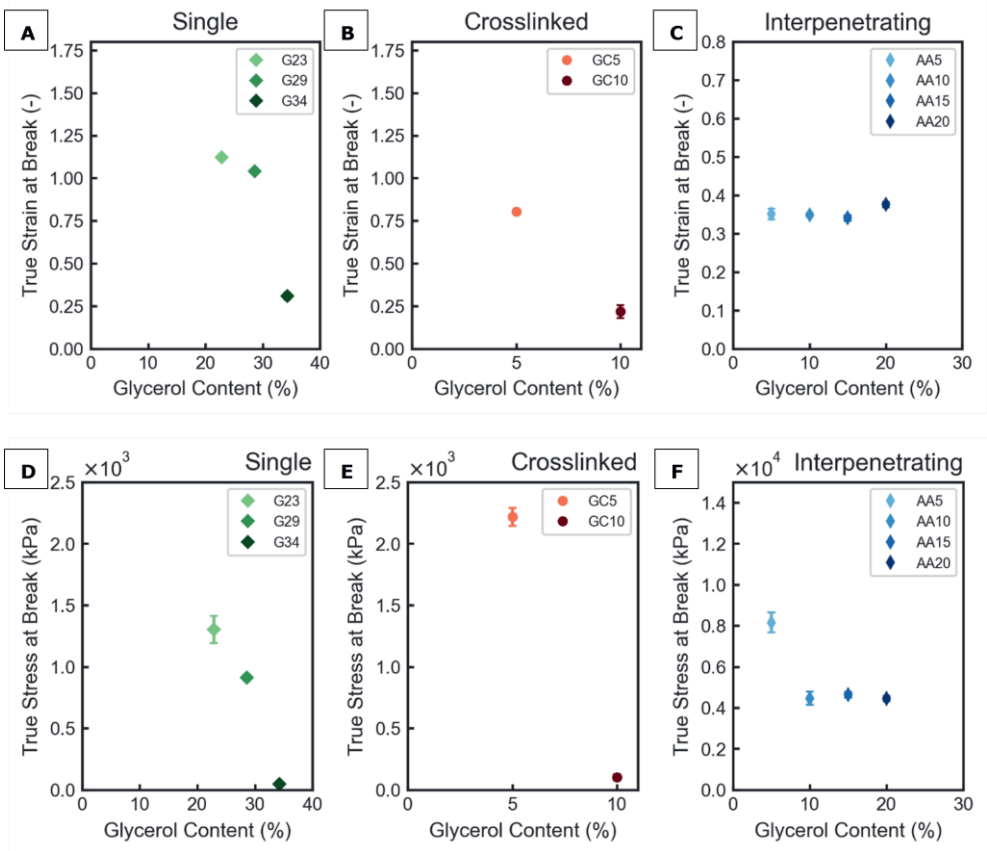


Fig. 4.5 *Film strength determined by uniaxial tensile tests: True strain at break as function of glycerol content for gelatine films (A), gelatine-caseinate films (B) and agar-alginate films (C); True stress at*

break as function of glycerol content for gelatine films (D), gelatine-caseinate films (E) and agar-alginate films (F); test results of at least 5 technical replicates are presented as mean ± SD (standard deviation).

4.3.2.3 Strain hardening

Strain hardening (n) is a measure of the (nonlinear) often irreversible increase in stress required to sustain tensile deformation. The stress-strain curves of all film types showed clear evidence of plastic deformation at higher strain levels, and thus strain hardening behaviour was expected for all film types. Consistent with this, the plastic region of the stress-strain curves was well captured by the Hollomon law (**equation 4.4**), yielding coefficients of determination of $R^2 \geq 0.98$ for all samples.

Increasing the plasticizer content of SN films resulted in a reduction of the strain hardening exponent (**Table 4.2**). Plasticizers increase the chain mobility and facilitate distribution of the deformation over a larger fraction of all chains, enhancing the compliance to stretching.

For IPN films a slight increase of the strain hardening coefficient was observed with increasing plasticizer content (**Table 4.2**). The strain hardening coefficient of acetylated chitosan hydrogels crosslinked with genipin was reported to depend on the balance between weak physical entanglements and strong covalent crosslinks, which could be modulated through the gelation temperature (Mio et al., 2022). We expect that our plasticizers have a similar modulating effect. In our IPN film, the first network is a stiff agar network, whereas the second network is a ductile alginate network. We hypothesize that addition of plasticizer mainly influences the second, more ductile network which affects its energy dissipating capacity. This could have resulted in the observed increased strain hardening coefficient of the IPN with the increase of glycerol concentrations.

Table 4.2 *Strain hardening parameters of single network (SN), crosslinked network (CN), and interpenetrating network (IPN) films with different plasticizer levels*

Film type	K (MPa)	n (-)
SN: Gelatine		
G23	0.138 ± 0.01	1.43 ± 0.08
G29	0.144 ± 0.00	1.25 ± 0.03
G34	0.034 ± 0.00	0.27 ± 0.04
CN: Gelatine-Caseinate		
GC5	0.854 ± 0.02	0.39 ± 0.01
GC10	0.311 ± 0.03	0.70 ± 0.05
IPN: Alginate-agar		
AA5	9.23 ± 0.55	0.57 ± 0.02
AA10	4.97 ± 0.69	0.53 ± 0.03
AA15	5.70 ± 0.14	0.61 ± 0.00
AA20	5.08 ± 0.20	0.66 ± 0.01

4.3.3 Biaxial tensile properties

4.3.3.1 Bulge shape fitting

For biaxial extensional testing, the bulge test as described before was used. During preliminary testing the approximation of the bulge outline with a circle and ellipse were compared using a representative SN film (G34). Fitting with a circle introduced a systematic error which increases as the bulge becomes larger with increasing pressure (as the deformation of the film becomes larger, **Fig. 4.6A**). The ratio of the major to minor axis of the fitted ellipse never approaches 1 (**Fig. 4.6B**), a ratio which indicates a circle as the major and minor axis of a circle are of equal length, thus $\frac{a}{b} = 1$. Fitting the bulge outline with an ellipse provided a much lower RMSE over the full pressure range (**equation 4.14**). This is in agreement with Mulder (2015) who reported that a spheroid (an axisymmetric ellipse) provides a superior fit to a

sphere (an axisymmetric circle) for bulge testing of metals. Accordingly, we used an ellipse shape to fit the bulge surface in this work.

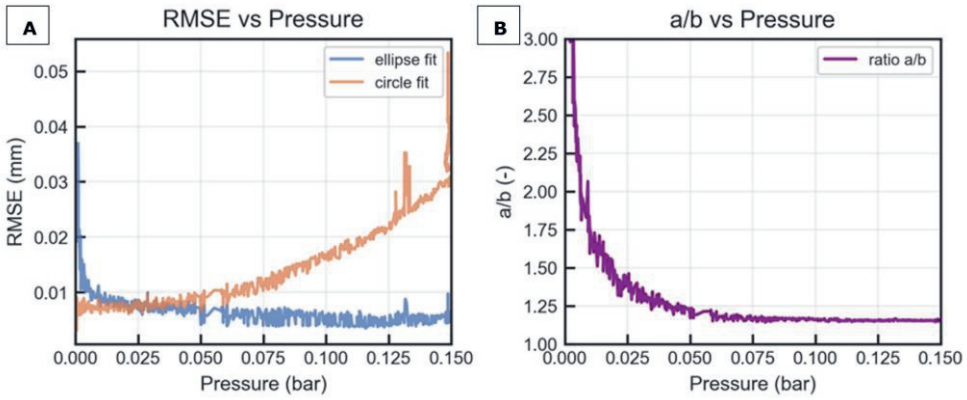


Fig. 4.6 *A) Absolute root mean square error (RMSE) of a circle and ellipse fitted to the bulge edge as function of pressure for sample G34; B) the ratio of the length of the major axis-a over the minor axis-b for an ellipse fitted to the bulge edge as function of pressure for sample G34.*

4.3.3.2 Biaxial tensile strength and comparison with uniaxial tensile strength

The biaxial tensile tests revealed the biaxial fracture behaviour of the SN, CN and IPN films as affected by glycerol (**Fig. 4.7**). The true stress at break determined by biaxial tensile tests ranged from 23-210, to 81-345 and 1800-6400 kPa for SN, CN films and IPN films, respectively, depending on plasticizer content (**Fig. 4.7**). Full true strain-true stress curves can be found in the section 'Biaxial strain stress curves' of the Supplementary Materials. Interestingly, unlike the uniaxial test result which indicated that the plasticizer content did not affect the true strain and stress at break for IPN films (**Fig. 4.5C** and **Fig. 4.5F**), the biaxial test results clearly indicate that the true biaxial strain and stress at break decrease with plasticizer content (**Fig. 4.7C** and **Fig. 4.7F**). This decrease in biaxial fracture strain and stress may be explained by the increased mobility of the chains due to the plasticizer, resulting in creep and ultimately allowing failure of the film under stress.

Although same film samples were used for biaxial and uniaxial tensile tests, distinct results were shown. This highlights the necessity of performing both tests to obtain more representative information on how the films would perform when used in different applications where uniaxial/biaxial stresses are relevant.

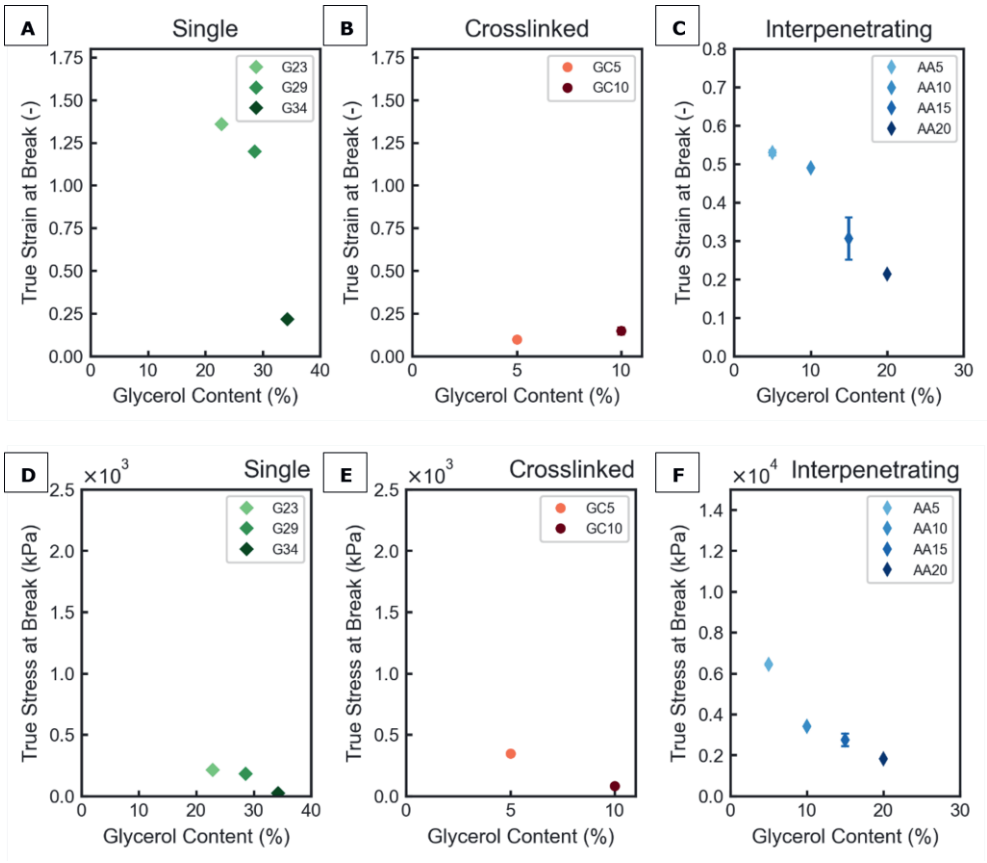


Fig. 4.7 *Film strength determined by biaxial tensile tests: True strain at break as function of glycerol content for gelatine films (A), gelatine-caseinate films (B) and agar-alginate films (C). True stress at break as function of glycerol content for gelatine films (D), gelatine-caseinate films (E) and agar-alginate films (F); test results of at least technical replicates were shown as mean ± SD (standard deviation).*

In general, true strain and stress at break values obtained via this biaxial test were of a similar order of magnitude to those determined through uniaxial

tensile testing (Fig. 4.8), supporting the validity of the test results. Interestingly, a much lower fracture strain was observed for the GC5 film during biaxial test, as compared to the uniaxial test result (Fig. 4.8). During handling, it was noticed that the GC5 films were somewhat brittle. When the film was fixated onto the setup, small surface defects were probably caused by manipulation of the film. These defects could easily propagate, causing sudden and large ruptures during inflation, which is also reflected in the lower fracture stress of this sample during biaxial test (Fig. 4.7E), as compared to the uniaxial test (Fig. 4.5E).

Additionally, the computer-vision-based bulge test enables the repeated stretching of films using an oscillatory pressure function, which could be used to test fatigue properties of thin films. While an in-depth investigation of this was out of scope for the current study, preliminary results can be found in the section 'Fatigue testing using biaxial tensile test setup' of the Supplementary Materials.

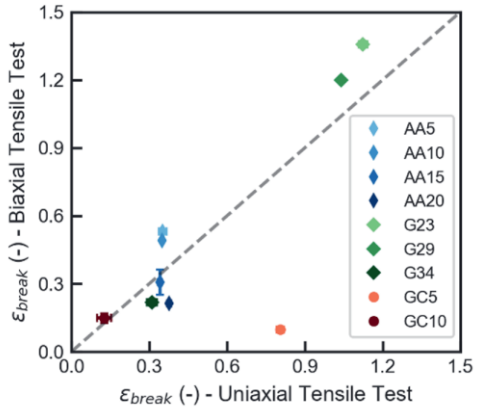


Fig. 4.8 *True strain at break εbreak for SN films (G), CN films (GC) and IPN films (AA) compared between uniaxial tensile test and biaxial tensile test.*

4.4 Conclusion

The mechanical properties of different types of edible biopolymer films as affected by their plasticizer content were investigated. Single-network (SN), crosslinked-network (CN) and interpenetrating-network (IPN) films consisting of gelatine, and the combinations gelatine-caseinate and alginate-agar, respectively, were characterized by combining a standard uniaxial tensile test and an in-house developed biaxial bulge test.

Glycerol as plasticizer increased the film elasticity for all film types but reduced their stress at break. Contrary to literature, glycerol addition was found to reduce the strain at break, which could be related to segregation of plasticizer during the drying of the films. While uniaxial deformation showed no effects of the plasticizer content on the strain and stress at break with IPN films, biaxial testing revealed reductions in tensile strength. We attribute this to a reduction of the energy dissipating capacity of the secondary network in the interpenetrating-network film during biaxial extension. Although the interpenetrating networks create strong films with better properties than their single network counterparts, future studies should focus on improving their biaxial extensibility and assessing the effects of successive load cycles on tensile properties.

The starkly differing results between uniaxial and biaxial deformation for IPN films indicate that it is important to choose a deformation assessment that is relevant to the application. Moreover, this indicates that different network types respond differently to uniaxial and biaxial deformation, which is likely related to the mechanisms by which they dissipate stresses. In many practical applications, deformation of films is biaxial, and hence it is important to use a biaxial test method. Since data extraction with our custom biaxial tensile

test is simple and fast, it thus represents an improvement in both methodology and in convenience compared to existing biaxial tensile tests.

Appendix 4

A4.1 Python code

Python version 3.13 was used with the packages listed in Table A4.1

Table A4.1 *Python packages used*

Package	Version
circle-fit	0.2.1
contourpy	1.3.1
cycler	0.12.1
et_xmlfile	2.0.0
fonttools	4.57.0
imageio	2.37.0
joblib	1.4.2
kiwisolver	1.4.8
lazy_loader	0.4
matplotlib	3.10.1
networkx	3.4.2
numpy	2.2.4
opencv-python	4.11.0.86
openpyxl	3.1.5
packaging	2.4.2
pandas	2.2.3
pillow	11.2.1
pip	25.0.1
pyparsing	3.2.3
pyserial	3.5
python-dateutil	2.9.0.post0
pytz	2025.2
regex	2024.11.6
scikit-image	0.25.2
scikit-learn	1.6.1
scipy	1.15.2
seaborn	0.13.2
six	1.17.0
threadpoolctl	3.6.0
tifffile	2025.3.30
tzdata	2025.2
xlrd	2.0.1

A4.2 Film thickness

Table A4.2 *Average film thickness per sample type*

Sample type	S_0 (mm)
AA5	0.146 ± 0.002
AA10	0.149 ± 0.014
AA15	0.256 ± 0.015
AA20	0.590 ± 0.056
G23	2.173 ± 0.074
G29	2.168 ± 0.215
G34	1.654 ± 0.399
GC5	0.362 ± 0.016
GC10	0.347 ± 0.007

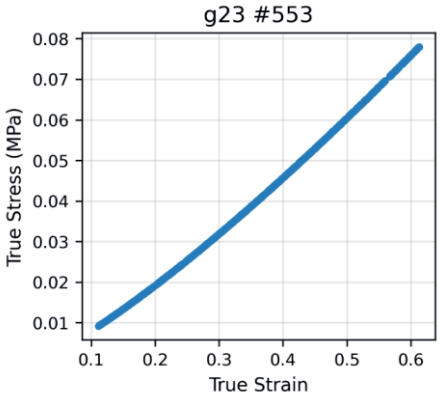
A4.2 Young's modulus

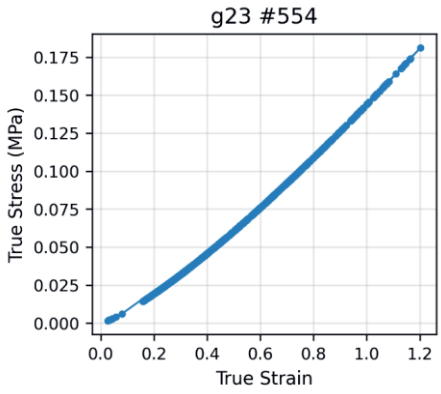
Table A4.3 *Statistics related to Young's moduli obtained from uniaxial tensile testing*

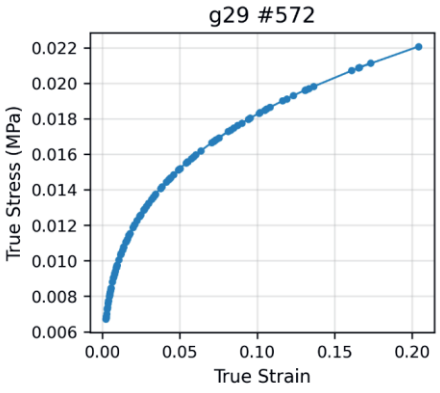
Sample type	Average R^2	Average Young's Modulus (kPa)	Std. Dev. (kPa)
AA5	0.9836	34731	4301
AA10	0.9735	21067	4180
AA15	0.9416	12832	1079
AA20	0.9595	9963	723.5
G23	0.9892	167.8	14.50
G29	0.9905	139.3	43.52
G34	0.9762	83.97	28.89
GC5	0.8835	2325	73.18
GC10	0.9649	400.92	94.46

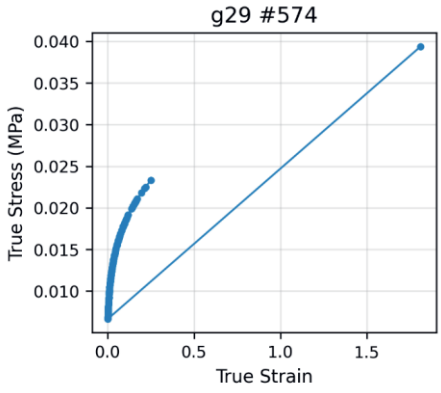
A4.3 Biaxial stress strain curves

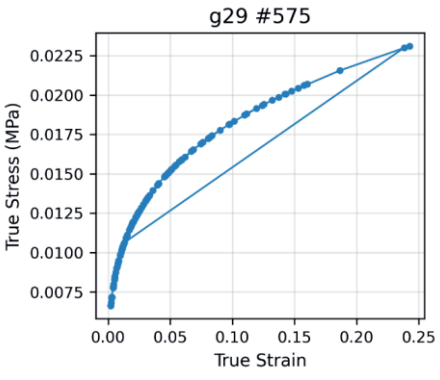
Strain stress curves obtained by bulge testing.

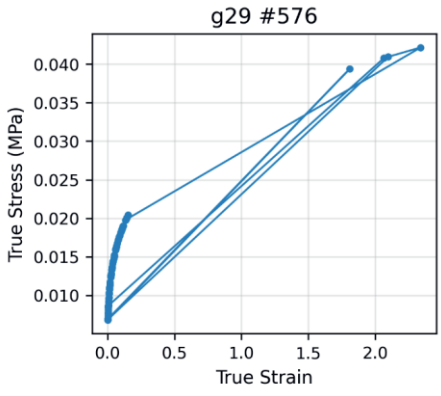


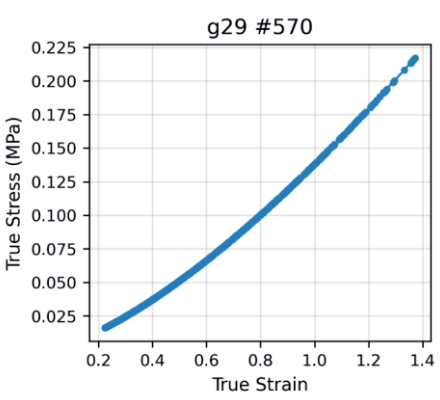


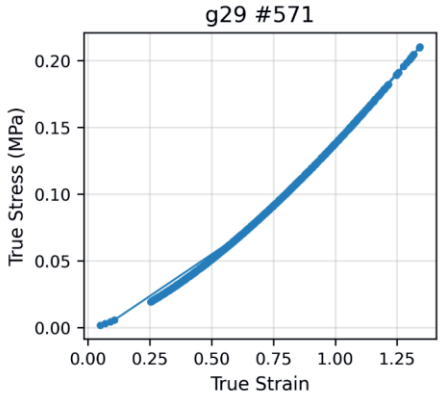


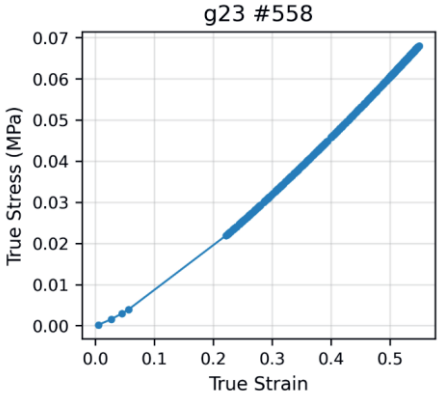


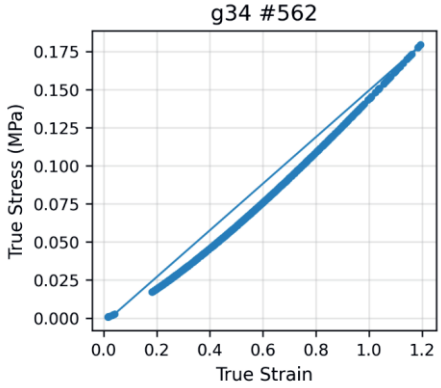


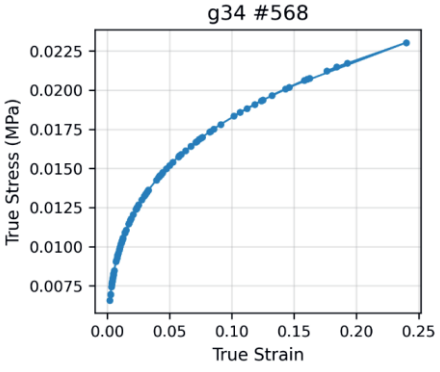


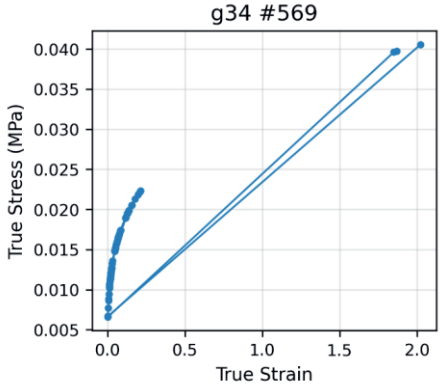

g29 #570
True Stress (MPa)
True Strain
0.225
0.200
0.175
0.150
0.125
0.100
0.075
0.050
0.025
0.2
0.4
0.6
0.8
1.0
1.2
1.4

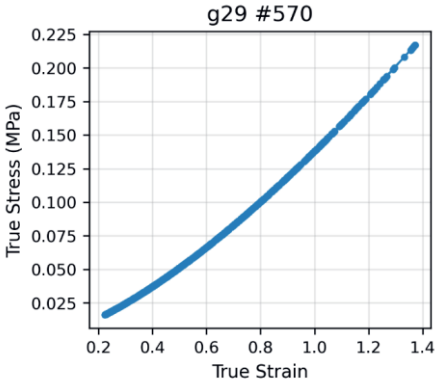

g29 #571
True Stress (MPa)
True Strain
0.20
0.15
0.10
0.05
0.00
0.00
0.25
0.50
0.75
1.00
1.25

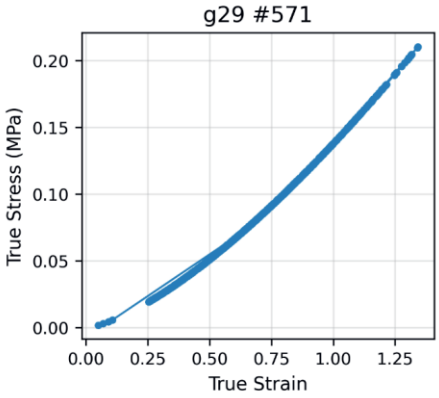

g23 #558
True Stress (MPa)
True Strain
0.07
0.06
0.05
0.04
0.03
0.02
0.01
0.00
0.0
0.1
0.2
0.3
0.4
0.5

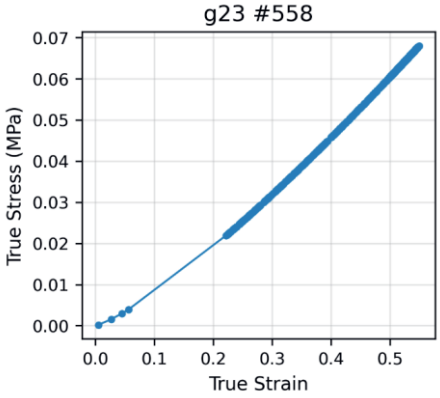

g34 #562
True Stress (MPa)
True Strain
0.175
0.150
0.125
0.100
0.075
0.050
0.025
0.000
0.0
0.2
0.4
0.6
0.8
1.0
1.2

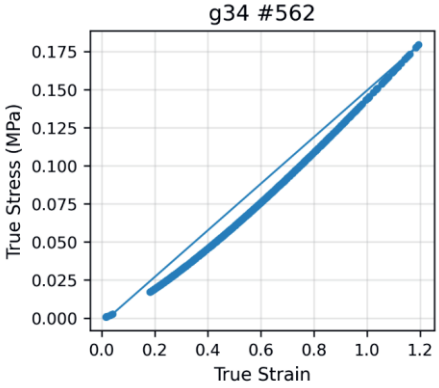

g34 #568
True Stress (MPa)
True Strain
0.0225
0.0200
0.0175
0.0150
0.0125
0.0100
0.0075
0.00
0.05
0.10
0.15
0.20
0.25

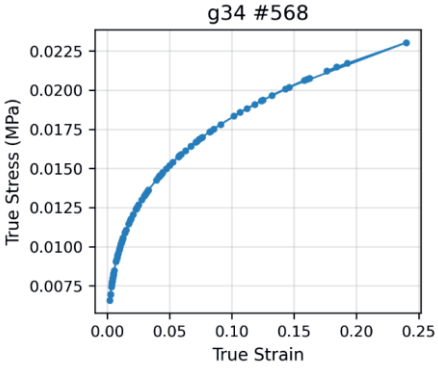

g34 #569
True Stress (MPa)
True Strain
0.040
0.035
0.030
0.025
0.020
0.015
0.010
0.005
0.0
0.5
1.0
1.5
2.0

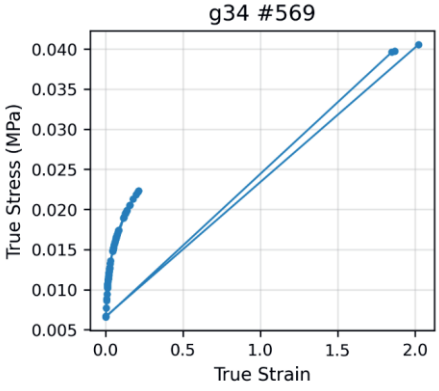

g29 #570
True Stress (MPa)
True Strain

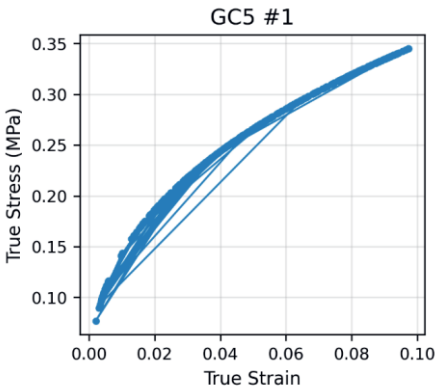

g29 #571
True Stress (MPa)
True Strain

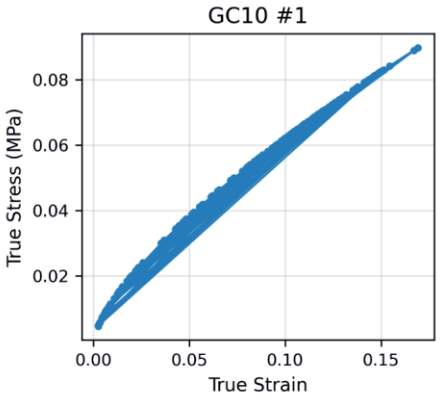

g23 #558
True Stress (MPa)
True Strain

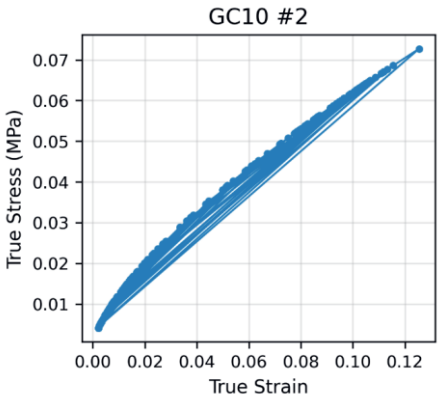

g34 #562
True Stress (MPa)
True Strain

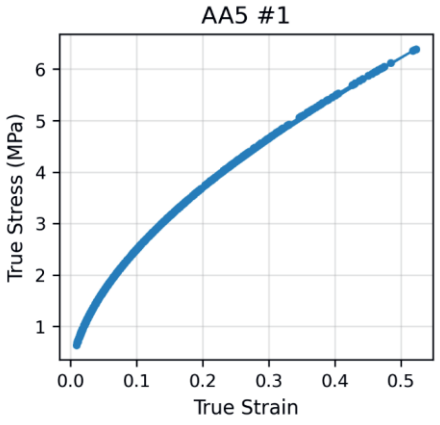

g34 #568
True Stress (MPa)
True Strain

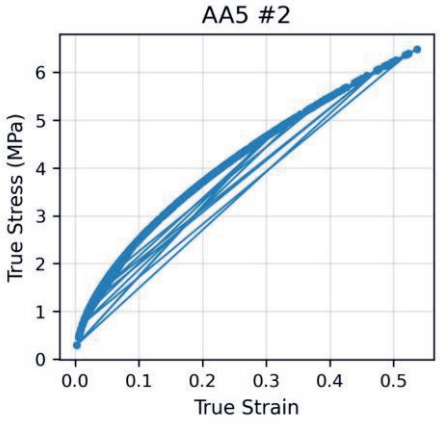

g34 #569
True Stress (MPa)
True Strain

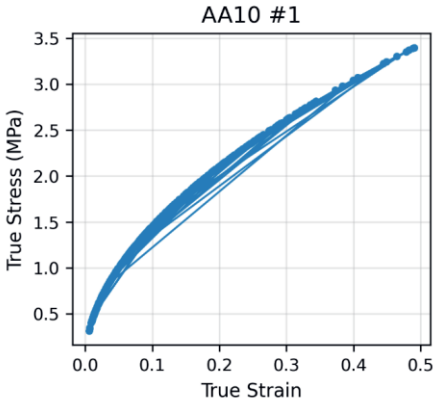

GC5 #1
True Stress (MPa)
0.35
0.30
0.25
0.20
0.15
0.10
0.00
0.02
0.04
0.06
0.08
0.10
True Strain

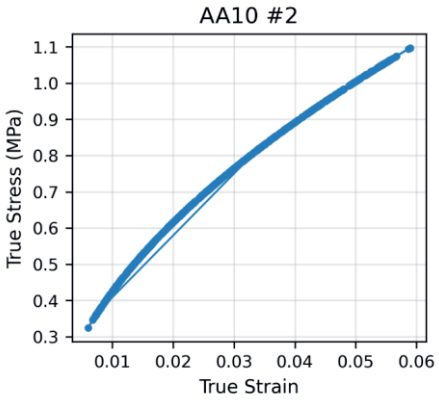

GC10 #1
True Stress (MPa)
0.08
0.06
0.04
0.02
0.00
0.05
0.10
0.15
True Strain

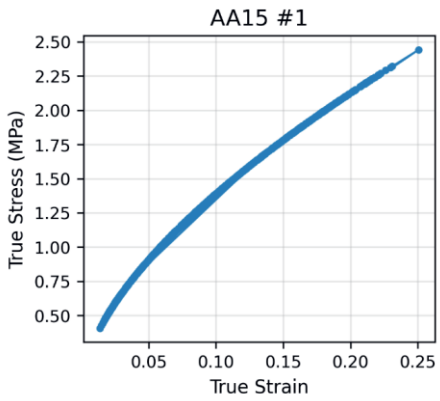

GC10 #2
True Stress (MPa)
0.07
0.06
0.05
0.04
0.03
0.02
0.01
0.00
0.02
0.04
0.06
0.08
0.10
0.12
True Strain

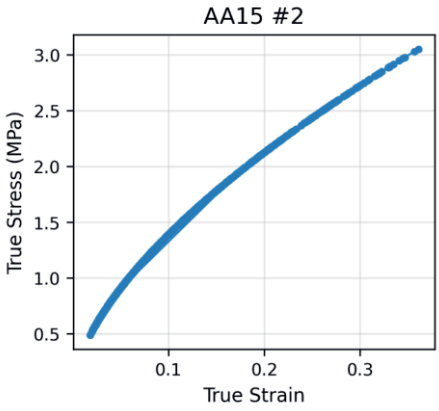

AA5 #1
True Stress (MPa)
6
5
4
3
2
1
0.0
0.1
0.2
0.3
0.4
0.5
True Strain

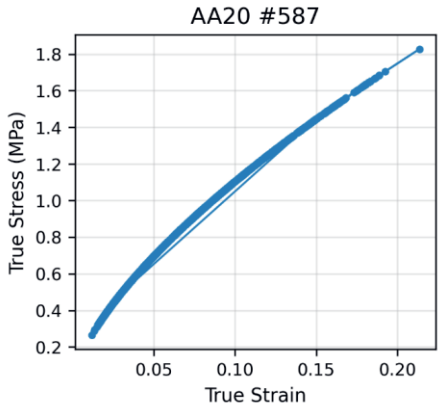

AA5 #2
True Stress (MPa)
6
5
4
3
2
1
0
0.0
0.1
0.2
0.3
0.4
0.5
True Strain

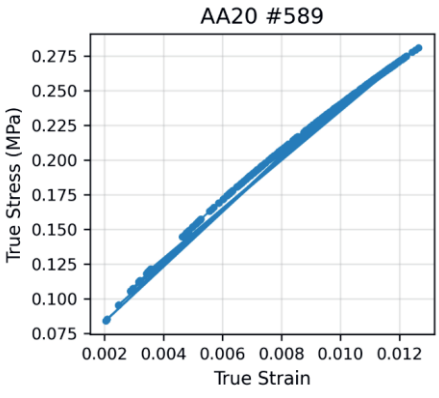

AA10 #1
True Stress (MPa)
3.5
3.0
2.5
2.0
1.5
1.0
0.5
0.0
0.1
0.2
0.3
0.4
0.5
True Strain


AA10 #2
True Stress (MPa)
1.1
1.0
0.9
0.8
0.7
0.6
0.5
0.4
0.3
0.01
0.02
0.03
0.04
0.05
0.06
True Strain


AA15 #1
True Stress (MPa)
2.50
2.25
2.00
1.75
1.50
1.25
1.00
0.75
0.50
0.05
0.10
0.15
0.20
0.25
True Strain


AA15 #2
True Stress (MPa)
3.0
2.5
2.0
1.5
1.0
0.5
0.1
0.2
0.3
True Strain


AA20 #587
True Stress (MPa)
1.8
1.6
1.4
1.2
1.0
0.8
0.6
0.4
0.2
0.05
0.10
0.15
0.20
True Strain


AA20 #589
True Stress (MPa)
0.275
0.250
0.225
0.200
0.175
0.150
0.125
0.100
0.075
0.002
0.004
0.006
0.008
0.010
0.012
True Strain

A4.2 Fatigue testing using biaxial tensile test setup

For the preliminary cyclic bulge testing, one experiment was performed for selected film types based on their expected ability to stretch and shrink. Pressure was oscillated four times between 0 and 50% of the pressure that had been determined to cause film failure during prior bulge tests. The first cycle took 210 seconds while every subsequent cycle took 180 seconds. In the fifth and final cycle, pressure was set at the maximum to cause film rupture. The air pressure was changed at rate of 0.04 bar/s.

Results with the AA-IPN films show that despite the application of the same pressure limit during the first four cycles, the highest strain observed increases slightly each cycle. This could be related to the Mullin's effect observed in elastomers, but requires further investigation (Krpovic et al., 2021).

Table A4.4 *Tensile strength (MPa) comparison between single and cyclic bulge tests*

Film type	Tensile strength Single test (MPa, average ± SD)	Tensile strength Cyclic test (MPa)	Remarks
AA5	10.5 (± 0.9)	12.3	
AA10	4.718 (± 0.09)	5.108	
AA15	2.61 (± 0.03)	1.48	Broke in 2nd cycle
AA10-reference	1.091 (± 0.006)	0.624	Broke in 1st cycle
GC5	0.42 (± 0.01)	0.40	

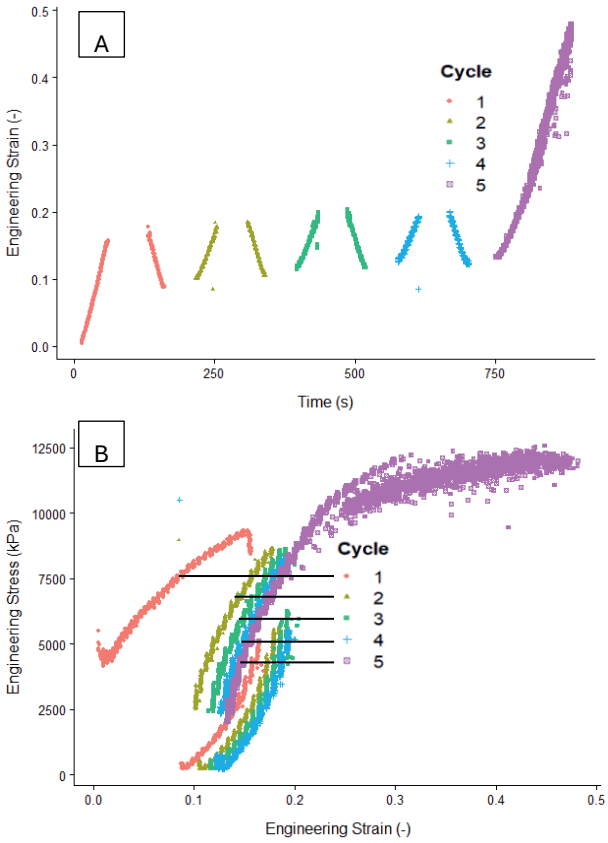


Fig. A4.1 *A) Engineering strain over time and B) Engineering stress-strain curve of AA5 film during a bulge test with five cycles, where maximum setpoint pressure was applied in the last cycle to cause rupture. Notably, data points during pressure calibration were removed to reduce noise.*

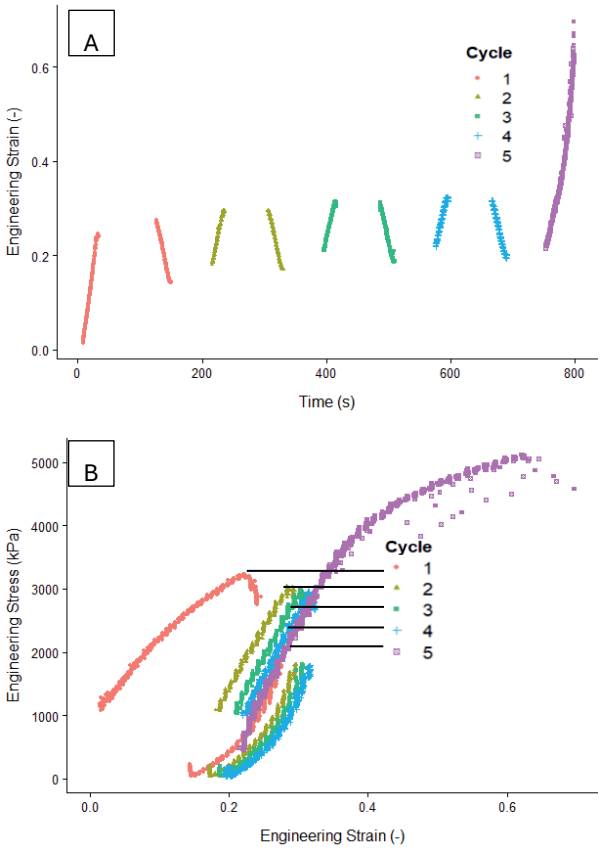


Fig. A4.2 *A) Engineering strain over time and B) Engineering stress-strain curve of AA10 film during a bulge test with five cycles, where maximum setpoint pressure was applied in the last cycle to cause rupture. Notably, data points during pressure calibration were removed to reduce noise.*

Chapter 5

General discussion

5.1 Thesis overview

The studies reported in this thesis aimed to unveil guidelines for the development of edible, digestible materials that can be used to pioneer the field of edible robotics and enable novel applications of materials in other fields to benefit health, society and the environment. Bioinspired, soft edible robots with anisotropic designs show the most potential, and require development of two opposing material types: one rigid and stiff with the other being flexible and extensible. This chapter first summarizes the processing and characterization methods that were developed to fabricate and evaluate these material types in this thesis. A reflection on the implications of these developments follows and at the end of this chapter some directions for future research are suggested.

5.2 Main findings and general limitations

In **Chapter 1** the need to develop materials for edible robotics was introduced. It highlighted the lack of suitable analytical methods to evaluate material performance of edible materials in non-edible applications as well as a lack of knowledge on how to use (food) processing methods to produce edible composite materials for non-eating applications within food science. Composites were defined as materials formed by combining one or more ingredients through specific formulation and processing steps. A thorough understanding of structure-function relationships of composites would allow a rational selection of food ingredients and processing methods to design composites with desired properties and functionality.

In **Chapters 2, 3 and 4** different processing and analytical methods were investigated and optimized, with progressive insight on overlapping themes such as fused deposition modelling to manufacture digital designs and computer vision analysis methods to evaluate mechanical performance of

composites. A key limitation in selecting processing methods that render materials deformable is that many induce irreversible structural changes, such as heat-induced crosslinking, thereby making the materials indigestible. Concepts from other scientific fields were adopted, such as bulge testing, which is commonly used to evaluate strain hardening of sheet metals under biaxial stress (Mulder et al., 2015). However, many models from other scientific fields cannot be applied directly to food materials due to differences in matrix interactions. For example, polymers typically adopt random-coil conformations, whereas many food matrices contain proteins with tertiary structures. However, some theories can still be applied to food materials. For example, the Flory-Huggins theory, which was originally developed for systems without tertiary structures, has been successfully applied to describe protein-rich matrices (Van Der Sman, 2025; van der Sman, 2012).

In **Chapter 2** fused deposition modelling of thermoplastic proteins was explored. First, the material requirements for FDM processing were established based on literature data. Subsequently, a feedstock for a fused deposition modelling 3D printer was developed through processing steps involving protein dissolution, plasticization, film casting and pelletisation. The thermal and rheological properties of composites with various plasticizer levels were characterized and correlated well with their printing performance. It was found that controlling the glass transition temperature is essential for controlling the material state during FDM. Based on these findings a state diagram with iso-viscosity lines was constructed based on the glass transition temperatures of zein-based composites with a range of plasticizer levels, allowing prediction of suitable 3D printing temperatures. Zein-based pellets were used to 3D print several demonstrator models, without the need for postprocessing and achieving overhang angles up to 45°. This was a first step towards the fabrication of rigid components for edible robotics. A limitation

of the FDM process was the high viscosity of most protein-based composites (e.g. based on calcium caseinate), as well as the cross-linking many proteins exhibit when exposed to elevated temperatures for extended times. This would constrain the choice of ingredients, reducing the ability to select them according to desired properties such as solubility or digestibility. Additionally, the pellet production process would be expensive to scale up, hindering wide-scale adaptation. Only limited plasticization could be achieved with glycerol due to phase separation at higher plasticizer levels.

In **Chapter 3** the fused deposition modelling process of edible proteins was further developed. Addition of amphiphilic fatty acids as plasticizer in addition to hydrophilic glycerol in zein composites was found to have a synergistic effect on glass transition temperature depression, while maintaining phase compatibility. A relation between T_g/T and viscosity was also identified. After the development of the formulation, the thermoplastic zein filaments could be fabricated on a continuous extrusion line, proving the feasibility to scale up the production of edible filament. The edible filament was then utilized to 3D print complex geometries, such as a flexible spiral spring. The mechanical properties of objects 3D printed with edible filament were compared to references printed using common 3D printing plastics. This work demonstrated that through rational formulation development, conventional manufacturing equipment such as extruders and FDM 3D printers can be utilized to produce edible, rigid components at large scale with possibilities for high levels of customization. Future studies may improve the 3D printing process of the edible filament by optimizing filament retraction and cooling. Another interesting pathway for exploration is the incorporation of active fillers to the filament, such as conductive materials to enable 3D printing of electronically conductive objects.

In **Chapter 4** the mechanical behaviour of edible hydrogels was explored to identify materials suitable for high-stretch applications, such as pneumatic actuators. The extensional properties of single network (SN), crosslinked network (CN) and interpenetrating network (IPN) hydrogels were studied as function of plasticizer content. Their extensional properties were characterized with a custom computer-vision-based biaxial extension testing method developed at our lab and compared to standard uniaxial tensile testing results. Biaxial deformation could be described accurately using an ellipsoid shape function. The plasticizer content affected the tensile properties of IPN films differently under uniaxial and biaxial loading conditions, highlighting the need to combine both analysis methods to evaluate the applicability of materials for applications involving multiple types of stress loading. Furthermore, IPN films had very high tensile strength.

The results from this study reveal that network structure and plasticization can be used to modulate the tensile properties of thin films to allow for a wide range of mechanical properties. This insight contributes to the development of rational design approaches for edible films for various applications. Future works should focus on characterising the stress-strain response of hydrogels over multiple actuation cycles to improve translation of the results to application scenarios such as pneumatic actuators. A limitation of the edible films studied here, was their yield-stress behaviour, which makes repeated actuation behaviour more difficult to model compared to conventional elastomers like rubbers and silicone. Additionally, it is of interest to study the performance of anisotropic films, for example films with added fibers. Finally, some consideration should be given to the development of an edible source of gas generation for pneumatic actuation, to enable untethered movement. For example, chemical reactions could be employed to generate gas within an edible actuator (Floreano et al., 2024). Release of gas in

multiple phases as well as reversible actuation should be targeted in future works.

Chapters 2, 3 and 4 described the feasibility of fabricating both rigid and stiff materials as well flexible and extensible materials, plus several analytical methods for evaluation of their performance. In the sections below, some suggestions are provided for the utilisation of these materials in the context of edible robotics and materials with added functionalities, as well as for further testing of material performance in specific applications.

5.2.1 Conductive protein-based filaments and films

The functionality of the materials developed in this work could be further extended, for example using dispersions. In the robotics field, carbon black has been widely utilized as filler in polymeric materials for its conductive properties. The high specific surface area of carbon black allows a conductive network to be formed even at low filler concentrations (Huang, 2002). An edible (though not digestible) alternative with a low conductivity is activated carbon. The melt-compounding process utilized during filament making can be used to disperse conductive materials in the polymer matrix.

When the typical distance between conductive (i.e. carbon black) aggregates becomes smaller than a critical distance, electrons can flow across from one aggregate to another, resulting in electric percolation through the matrix, in effect creating a conductive material. The polymer matrix thus exhibits a major transition from an electrical insulator to an electrical conductor once a threshold concentration of conductive filler is reached. This critical filler concentration is known as the percolation threshold (Ren et al., 2014).

The exact percolation threshold is a function of the shape and density of the carbon aggregates shape, interaction between polymer and filler, as well as

the melt viscosity and crystallinity of the polymer. Irregular and low-density particles may already connect at low volume fractions. Crystallisation of the polymer can expel the carbon aggregates towards amorphous regions, effectively lowering the percolation threshold. Finally, threshold concentrations increase with polymer molecular weight. Lower viscosities speed up the formation of conductive networks. Adding plasticizers therefore also reduces the percolation threshold and increases (surface and volume) conductivity (Huang, 2002). The percolation threshold of carbon black is commonly 3-15% w/w, which is high enough to increase the melt viscosity and decrease mechanical properties of polymers (Huang, 2002; Li et al., 2007). The percolation threshold of activated carbon has not yet been reported in literature.

Addition of fillers also affects the rheology of the polymer melt. At low filler content, the melt flow is similar to that of the neat polymer (Ren et al., 2014). At higher concentrations, the complex viscosity becomes dependent on the filler concentration. The lowest filler concentration which induces this dependency is called the rheological percolation threshold.

Based on these literature observations on carbon black filled polymer matrices, we developed edible conductive filaments and films using zein, glycerol and activated carbon (Vinoferm). Carbon black (99.9%, acetylene black, 50% compressed, Thermo Fischer Scientific) was used as a non-edible conductive filler (reference). The rheological properties of these composites were analysed during compounding, which were compared to that of the one without adding fillers. The stable (equilibrium) shear stress and viscosity during compounding were linearly correlated to the filler content (**Fig. 5.1A**) which indicates the rheological percolation threshold for carbon black in zein is low. Moreover, percolation was persistent throughout longer sections of the

filament as indicated by a linear correlation of resistance and filament length (B).

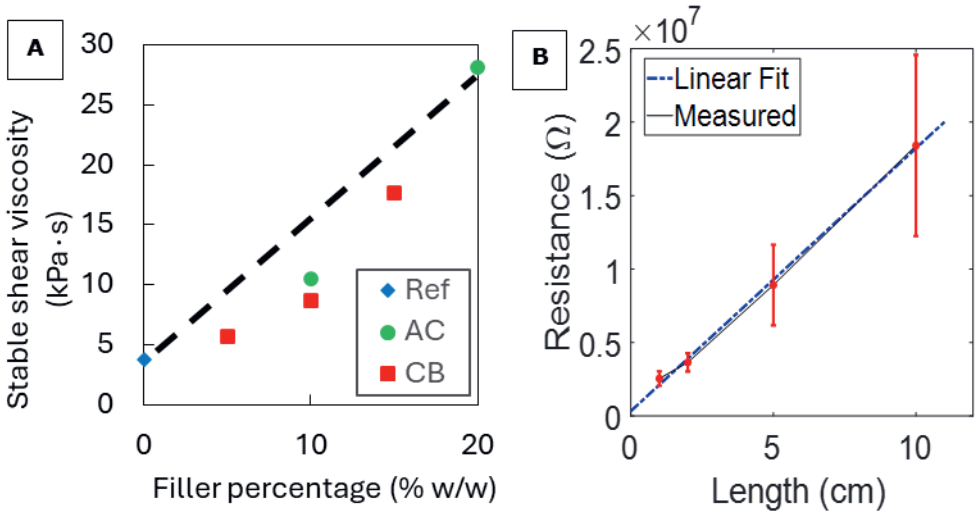


Fig. 5.1 *A: Stable (equilibrium) shear stress of conductive composite materials and reference during compounding, as influenced by the concentration of conductive fillers added to Reference (Ref) composite consisting of 80% zein and 20% glycerol (i.e. activated carbon (AC) and carbon black (CB)); B: resistance of the extruded zein filament with 28% w/w of activated carbon filler as influenced by the length.*

The type of filler did not affect the stable shear viscosity (**Fig. 5.1A**). Generally, the particle size distribution of fillers affects the melt viscosity, so we determined the particle size distribution of activated carbon and carbon black powders using a Mastersizer 3000 equipped with a powder cell. Powders were forced through a sieve prior to measurement to remove larger aggregates. The powder feed rate was adjusted until residuals were less than 2% before data was collected and each sample was measured in triplicate. The results show that carbon black consists of smaller particles and had a wider spread in particle size compared to activated carbon (**Fig.5.2A,B**).

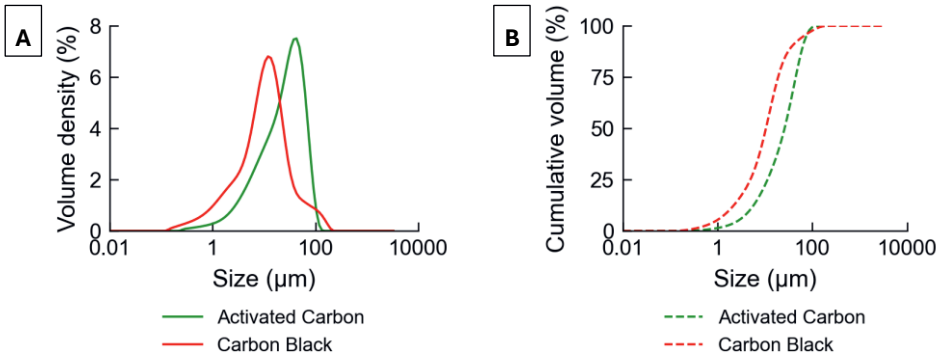


Fig.5.2 *Volume density (A) and cumulative volume (B) of particle size distribution of activated carbon and carbon black used to fabricate edible, conductive composites*

Since the viscosity was independent of the type of carbon filler, this indicates that the viscosity was independent of the particle size distribution. The viscosity could be well described using the Krieger-Dougherty model (Krieger and Dougherty, 1959):

$$\eta_r = \frac{\eta}{\eta_0} = \left(1 - \frac{\phi}{\phi_{max}}\right)^{-[\eta]\phi_{max}} \qquad \textit{Eq. A5.1}$$

With η the bulk viscosity, η_0 the viscosity of the liquid, ϕ the solid (filler) fraction, ϕ_{max} the maximum solid fraction in the suspension at which the suspension can still flow and $[\eta]$ the intrinsic viscosity (a measure for particle shape). Fitting the measurement data and minimizing the sum of squares residuals yields ϕ_{max} = 0.33 and $[\eta]$ = 7.

Compared to literature data for the conductance (or conductivity) of ethylene-vinyl acetate (EVA), the shape of the function is very similar to the percolation scaling relation (Huang, 2002):

$$\sigma = a(\phi - \phi_c)^{\mu} \qquad \text{Eq. A5.2}$$

With σ the conductivity of the composite, a a system-dependent constant, ϕ the carbon volume fraction, ϕ_c the critical volume fraction where a conductive networks forms (percolation threshold) and μ an exponent describing how strongly conductance scales with the volume fraction above the percolation threshold. Fitting the measurement data and minimizing the sum of squares residuals yields a = 0.022, ϕ_c = 8% and μ = 2 (**Fig.5.3**).

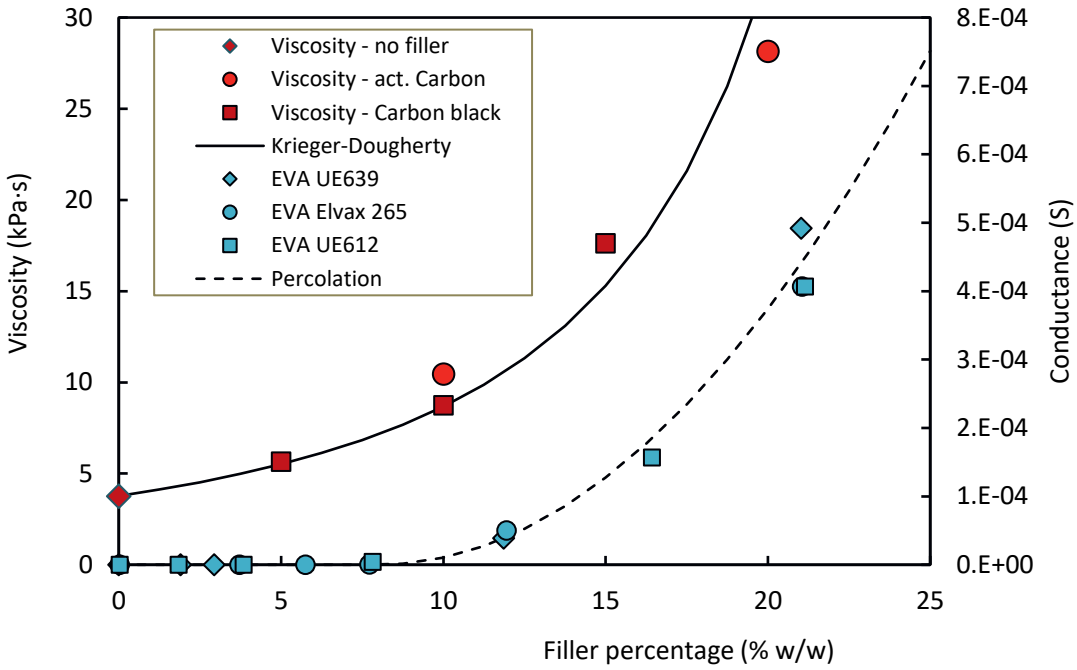


Fig.5.3 Viscosity of dispersions of carbon black and activated carbon in a zein matrix (red symbols) fitted with the Krieger-Dougherty relation (continuous line) with a ϕ_m of 33%. Conductance of EVA (blue symbols, (Huang, 2002)) fitted with percolation threshold relation, with a critical volume fraction ϕ_c of 8% (dashed line).

SEM images show that the conductive particles form aggregates with a rough surface (Fig.5.4). For SEM analysis, samples were fixated on aluminium sample stubs (9.5mm) using carbon adhesive tabs. Before imaging, the samples were coated with gold by a sputter-coater (Joel Smart-Coater). SEM-images were taken at 5kV, using a JEOL JCM-7000.

In conclusion, it can be hypothesized that the rheological percolation threshold and the conductivity percolation threshold are correlated, although more data is required to support this hypothesis.

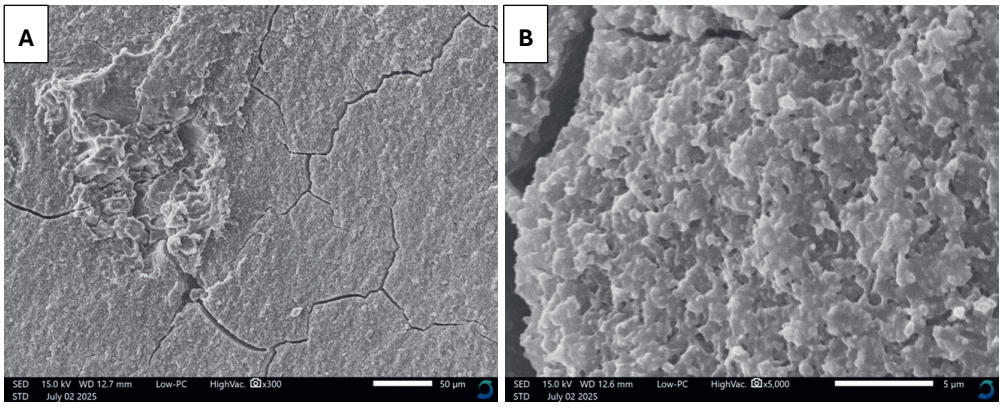


Fig.5.4 *SEM images of zein filament with carbon black at 300x magnification (A) and 5000x magnification (B)*

Increasing the filler content to over 28% w/w increased the torque required for mixing above the machine limit of the extruder (MicroCompounder 15 HT, Xplore, The Netherlands). It was therefore not possible to fabricate filaments at this high filler content. This is in line with the fitted value for ϕ_{max} of 0.33. However, by mixing zein, glycerol and activated carbon at a weight ratio of 48/12/40, and subsequently dispersing the mixture in ethanol followed by film casting and drying, conductive zein sheets with 40% activated carbon filler could be fabricated. We suspect this was possible because the addition of ethanol temporarily reduced the volume fraction of

the filler below the maximum solid fraction. The conductivity of these zein sheets was high enough to act as a conductive trace for powering a 3V LED (Fig. 5.5). To create sheets or traces with a customized shape, a more powerful melt compounding device could be used followed by hot plate pressing (Ren et al., 2014). These carbon sheets can be utilized to create temperature sensors since carbon has a negative temperature coefficient, and such sensors could be safely ingested by humans (Annese et al., 2024).

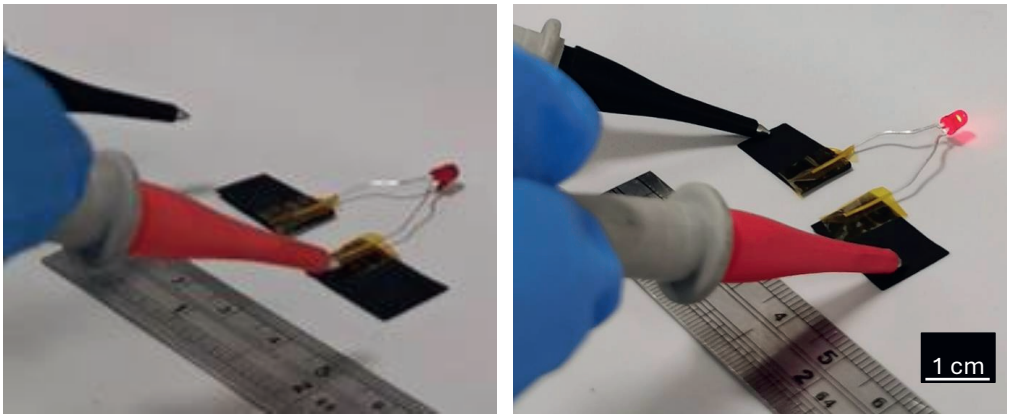


Fig. 5.5 *LED powered by a 3 V laboratory power supply, with a 2 cm conductive sheet positioned between the supply test leads and the LED leads (anode and cathode).*

In summary, our preliminary results indicate that the mechanical and electrical properties of composites with conductive fillers are dependent on both formulation strategy and processing conditions. The conductive percolation threshold and rheological percolation threshold seem correlated, implying that inclusion of activated carbon above the percolation threshold will significantly affect the mechanical properties of edible composites. These conductive composites may be applied in for example edible electronics or sensors.

5.2.2 Edible spring

Elastic energy can be stored using wind-up mechanisms. Several types of such mechanisms can be fabricated using FDM. A device was fabricated to measure the torsional constant of spiral springs 3D printed using zein-based filament (Fig.5.6A). Preliminary results showed that the springs could be rotated up to 140 degrees prior to fracture, with an average torsional spring constant of 13.4 ± 2.2 Nmm/rad. The fracture location was similar for all springs (Fig.5.6B). Finite element simulation of the winding action indicates that the stress is not equally distributed over the spring (Fig.5.7). Both observations support the conclusion that the spring design can be optimized further to allow a higher spring constant without any increase in mass.

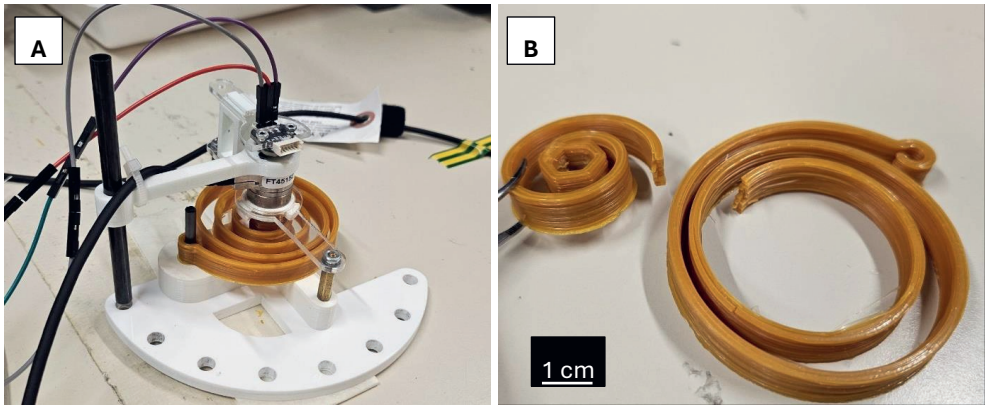


Fig.5.6 *A: Torsional spring constant measuring device and B: common fracture location after rotation*

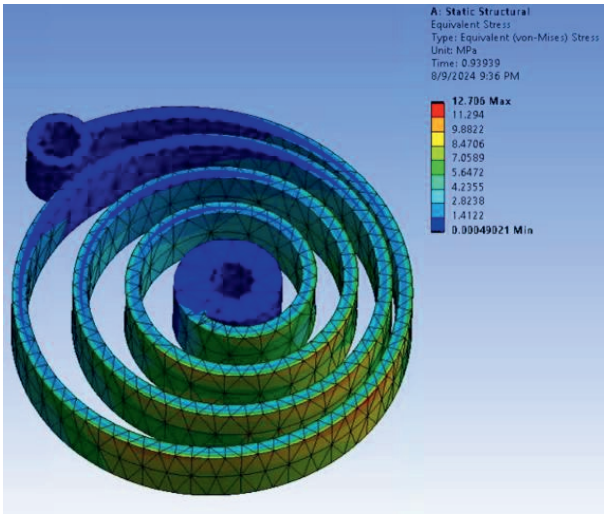


Fig.5.7 *Finite element simulation of spiral spring rotation in Abaqus. Colour gradient indicates the local stress level as result of rotation, with red indicating high local stress and blue low local stress values.*

The FDM process allows for optimisation of many object properties without changing the properties of the material that is being used to print it. For example, the density of an object can be adjusted by incorporating voids into its internal structure. Density can also be adjusted locally, allowing the point of gravity to be adjusted without changing overall geometry, or allowing strength of specific sections to be customized. Moreover, the infill pattern can be used to control compressive strength and flexural modulus. Fracture mechanics of 3D printed snack bars could be modulated by smart design of the infill pattern (Ma et al., 2024). In 3D printed edible cryogels ductility was controlled through outer wall thickness (Zhu et al., 2025).

5.2.3 Fatigue testing

The elastic edible materials developed in **Chapter 3** exhibited strain hardening behaviour, which limits the predictability of repeated actuation. This is especially true when they are compared to more ideal elastomers like silicones and rubbers, which are the standard in the field of soft robotics (Elango and Faudzi, 2015). To further study the behaviour of edible elastic

films over multiple actuation cycles utilizing the bulge test developed in this work, a preliminary experiment was performed in which films were stressed repeatedly (below their maximum tensile strength). This experiment and its results were described further in the Supplementary Materials of paper 3, section “Fatigue testing using biaxial tensile test setup”. A first observation was that the maximum strain achieved per pressure cycle slightly increased with cycle number, which is also observed for elastomers and generally attributed to the Mullin’s effect. The Mullins effect refers to stress softening that occurs during loading and unloading cycles, and indicates a reduction in stiffness of the material per cycle (Zhan et al., 2024). In complex networks, such as IPNs, it is likely that each strain cycle induces some damage to the polymer network on microscopic scale, most likely the soft, sacrificial part of the network.

Further development of this method is required to achieve good predictions of material fatigue. Eventually, integration of data obtained from uniaxial and biaxial methods on both rigid and stretchable materials could help to develop FEM models capable of simulating repeated actuation. Additionally, such models could incorporate the effects of mechanical anisotropy and fibre reinforcement.

5.3 General conclusion

Edible materials can be used in numerous applications that benefit human health, society and the environment. However, edible materials are studied almost exclusively in the context of food processing and food consumption. Therefore, processing routes and evaluation methods for edible composites for non-food applications need to be developed. The studies reported in this thesis aimed to inform design guidelines for the development of soft, edible robots, which required development of two opposing material types, one

being rigid and stiff and the other being flexible and extensible. For the fabrication of strong and rigid components, formulation and process design of protein-based composites for fused deposition modelling 3D printing was investigated. The results revealed the influence of the material states on the material properties. For the fabrication of flexible and extensible components, highly stretchable hydrogel films were developed and their mechanical behaviour under uniaxial and biaxial loading conditions was investigated. Network structure was found to influence the material properties, with the stress-strain response being dependent on loading conditions for specific network structures. The knowledge gained on fabrication methods and material performance analysis benefits the development of edible composites which are strong, flexible and responsive. This way of reinventing structural material engineering using food ingredients strengthens the foundation for the development of edible robots and robotic foods.

References

Acierno, D., Patti, A., 2023. Fused Deposition Modelling (FDM) of Thermoplastic-Based Filaments: Process and Rheological Properties—An Overview. Materials 16, 7664. https://doi.org/10.3390/ma16247664

Ajinjeru, C., Kishore, V., Liu, P., Hassen, A.A., Lindahl, J., Kunc, V., Duty, C., 2017. Rheological evaluation of high temperature polymers to identify successful extrusion parameters.

Annese, V.F., Galli, V., Coco, G., Caironi, M., 2024. A carbon-based NTC resistive temperature sensor for edible electronics. IEEE Journal on Flexible Electronics 3, 300–305.

Arrieta, M.P., Peltzer, M.A., Garrigós, M.D.C., Jiménez, A., 2013. Structure and mechanical properties of sodium and calcium caseinate edible active films with carvacrol. Journal of Food Engineering 114, 486–494. https://doi.org/10.1016/j.jfoodeng.2012.09.002

Bakarich, S.E., Panhuis, M. in het, Beirne, S., Wallace, G.G., Spinks, G.M., 2013. Extrusion printing of ionic–covalent entanglement hydrogels with high toughness. J. Mater. Chem. B 1, 4939–4946. https://doi.org/10.1039/C3TB21159B

Barra, G., Mitchell, J., 2013. The Rheology of Caramel. Current Nutrition & Food Science 9, 15–25. https://doi.org/10.2174/157340113804810842

Basu, T., Bhutani, U., Majumdar, S., 2022. Cross-linker-free sodium alginate and gelatin hydrogels: a multiscale biomaterial design framework. J. Mater. Chem. B 10, 3614–3623. https://doi.org/10.1039/D2TB00028H

Baumgartner, M., Hartmann, F., Drack, M., Preninger, D., Wirthl, D., Gerstmayr, R., Lehner, L., Mao, G., Pruckner, R., Demchyshyn, S., Reiter, L., Strobel, M., Stockinger, T., Schiller, D., Kimeswenger, S., Greibich, F., Buchberger, G., Bradt, E., Hild, S., Bauer, S., Kaltenbrunner, M., 2020. Resilient yet entirely degradable gelatin-based biogels for soft robots and electronics. Nat. Mater. 19, 1102–1109. https://doi.org/10.1038/s41563-020-0699-3

Bengoechea, C., Arrachid, A., Guerrero, A., Hill, S.E., Mitchell, J.R., 2007. Relationship between the glass transition temperature and the melt flow behavior for gluten, casein and soya. Journal of Cereal Science 45, 275–284. https://doi.org/10.1016/j.jcs.2006.08.011

Bhatia, S., Al-Harrasi, A., Almohana, I.H., Albayati, M.S., Jawad, M., Shah, Y.A., Ullah, S., Philip, A.K., Halim, S.A., Khan, A., Anwer, M.K., Koca, E., Aydemir, L.Y., Dıblan, S., 2024. The physicochemical properties and molecular docking study of plasticized amphotericin B loaded sodium alginate, carboxymethyl cellulose, and gelatin-based films. Heliyon 10, e24210. https://doi.org/10.1016/j.heliyon.2024.e24210

Bonnaillie, L., Zhang, H., Akkurt, S., Yam, K., Tomasula, P., 2014. Casein Films: The Effects of Formulation, Environmental Conditions and the Addition of Citric Pectin on the Structure and Mechanical Properties. Polymers 6, 2018–2036. https://doi.org/10.3390/polym6072018

Bootsma, K., Fitzgerald, M.M., Free, B., Dimbath, E., Conjerti, J., Reese, G., Konkolewicz, D., Berberich, J.A., Sparks, J.L., 2017. 3D printing of an interpenetrating network hydrogel material with tunable viscoelastic properties. Journal of the Mechanical Behavior of Biomedical Materials 70, 84–94. https://doi.org/10.1016/j.jmbbm.2016.07.020

Bouman, J., Belton, P., Venema, P., Van Der Linden, E., De Vries, R., Qi, S., 2015. The Development of Direct Extrusion-Injection Moulded Zein Matrices as Novel Oral Controlled Drug Delivery Systems. Pharm Res. https://doi.org/10.1007/s11095-015-1663-9

Brindle, L.P., Krochta, J.M., 2008. Physical Properties of Whey Protein–Hydroxypropylmethylcellulose Blend Edible Films. Journal of Food Science 73. https://doi.org/10.1111/j.1750-3841.2008.00941.x

Chambers, L.D., Winfield, J., Ieropoulos, I., Rossiter, J., 2014. Biodegradable and edible gelatine actuators for use as artificial muscles, in: Electroactive Polymer Actuators and Devices (EAPAD) 2014. Presented at the Electroactive Polymer Actuators and Devices (EAPAD) 2014, SPIE, pp. 46–51. https://doi.org/10.1117/12.2045104

Chambi, H., Grosso, C., 2006. Edible films produced with gelatin and casein cross-linked with transglutaminase. Food Research International 39, 458–466. https://doi.org/10.1016/j.foodres.2005.09.009

Charalambides, M., Wanigasooriya, L., Williams, G., Chakrabarti, S., 2002. Biaxial deformation of dough using the bubble inflation technique. I. Experimental. Rheologica Acta 41, 532–540. https://doi.org/10.1007/s00397-002-0242-2

Chaunier, L., Dalgalarrondo, M., Della Valle, G., Lourdin, D., Marion, D., Leroy, E., 2017a. Rheological characterization of plasticized corn proteins for fused deposition modeling. Presented at the PROCEEDINGS OF THE INTERNATIONAL CONFERENCE OF GLOBAL NETWORK FOR INNOVATIVE TECHNOLOGY AND AWAM INTERNATIONAL CONFERENCE IN CIVIL ENGINEERING (IGNITE-AICCE'17): Sustainable Technology And Practice For Infrastructure and Community Resilience, Penang, Malaysia, p. 040002. https://doi.org/10.1063/1.5008028

Chaunier, L., Guessasma, S., Belhabib, S., Della Valle, G., Lourdin, D., Leroy, E., 2018. Material extrusion of plant biopolymers: Opportunities & challenges for 3D printing. Additive Manufacturing 21, 220–233. https://doi.org/10.1016/j.addma.2018.03.016

Chaunier, L., Leroy, E., Valle, G.D., Dalgalarrondo, M., Bakan, B., Marion, D., Madec, B., Lourdin, D., 2017b. 3D printing of maize protein by fused deposition modeling. Presented at the PROCEEDINGS OF PPS-32: The 32nd International Conference of the Polymer Processing Society - Conference Papers, Lyon, France, p. 190003. https://doi.org/10.1063/1.5016792

Chaunier, L., Valle, G.D., Lourdin, D., Réguerre, A.-L., Cochet, K., Leroy, E., 2019. Viscous sintering kinetics of biopolymer filaments extruded for 3D printing. Polymer Testing 77, 105873. https://doi.org/10.1016/j.polymertesting.2019.04.020

Chaunier, L., Viau, L., Falourd, X., Lourdin, D., Leroy, E., 2020. A drug delivery system obtained by hot-melt processing of zein plasticized by a pharmaceutically active ionic liquid. Journal of Materials Chemistry B 8, 4672–4679.

Chen, J., Smith, D.E., 2021. Filament rheological characterization for fused filament fabrication additive manufacturing: A low-cost approach. Additive Manufacturing 47, 102208. https://doi.org/10.1016/j.addma.2021.102208

Chen, Q., Zhu, L., Huang, L., Chen, H., Xu, K., Tan, Y., Wang, P., Zheng, J., 2014. Fracture of the Physically Cross-Linked First Network in Hybrid Double Network Hydrogels. Macromolecules 47, 2140–2148. https://doi.org/10.1021/ma402542r

Chen, X., Xiao, J., Cai, J., Liu, H., 2020. Phase separation behavior in zein-gelatin composite film and its modulation effects on retention and release of multiple bioactive compounds. Food Hydrocolloids 109, 106105. https://doi.org/10.1016/j.foodhyd.2020.106105

Cheng, Z., Qiu, Y., Ahmad, I., Pang, Y., Yue, A., Chen, Z., Zhang, G., Ding, Y., Lyu, F., 2025. Enhancement of structural properties of 3D-printed plant-based meat analogs by TGase/laccase. Journal of Food Engineering 387, 112352. https://doi.org/10.1016/j.jfoodeng.2024.112352

Chevalier, E., Assezat, G., Prochazka, F., Oulahal, N., 2018. Development and characterization of a novel edible extruded sheet based on different casein sources and influence of the glycerol concentration. Food Hydrocolloids 75, 182–191. https://doi.org/10.1016/j.foodhyd.2017.08.028

Chhabra, R.P., Richardson, J.F., 2011. Non-Newtonian flow and applied rheology: engineering applications. Butterworth-Heinemann.

Choe, G., Tang, X., Wang, R., Wu, K., Jin Jeong, Y., Kyu An, T., Hyun Kim, S., Mi, L., 2022. Printing of self-healable gelatin conductors engineered for improving physical and electrical functions: Exploring potential application in soft actuators and sensors. Journal of Industrial and Engineering Chemistry 116, 171–179. https://doi.org/10.1016/j.jiec.2022.09.005

Choi, W.-S., Han, J.H., 2001. Physical and Mechanical Properties of Pea-Protein-based Edible Films. Journal of Food Science 66, 319–322. https://doi.org/10.1111/j.1365-2621.2001.tb11339.x

Clark, A.H., 1996. Biopolymer gels. Current Opinion in Colloid & Interface Science 1, 712–717. https://doi.org/10.1016/S1359-0294(96)80072-0

Coogan, T.J., Kazmer, D.O., 2019. In-line rheological monitoring of fused deposition modeling. Journal of Rheology 63, 141–155. https://doi.org/10.1122/1.5054648

Cox, W.P., Merz, E.H., 1958. Correlation of dynamic and steady flow viscosities. Journal of Polymer Science 28, 619–622. https://doi.org/10.1002/pol.1958.1202811812

Das, A., Gilmer, E.L., Biria, S., Bortner, M.J., 2021. Importance of Polymer Rheology on Material Extrusion Additive Manufacturing: Correlating Process Physics to Print Properties. ACS Appl. Polym. Mater. 3, 1218–1249. https://doi.org/10.1021/acsapm.0c01228

De Angelis, D., Latrofa, V., Caponio, F., Pasqualone, A., Summo, C., 2024. Techno-functional properties of dry-fractionated plant-based proteins and application in food product development: a review. Journal of the Science of Food and Agriculture 104, 1884–1896. https://doi.org/10.1002/jsfa.13168

de Carvalho, R.A., Grosso, C.R.F., 2004. Characterization of gelatin based films modified with transglutaminase, glyoxal and formaldehyde. Food Hydrocolloids 18, 717–726. https://doi.org/10.1016/j.foodhyd.2003.10.005

Del Dottore, E., Sadeghi, A., Mondini, A., Mattoli, V., Mazzolai, B., 2018. Toward Growing Robots: A Historical Evolution from Cellular to Plant-Inspired Robotics. Front. Robot. AI 5. https://doi.org/10.3389/frobt.2018.00016

Dey, A., Roan Eagle, I.N., Yodo, N., 2021. A Review on Filament Materials for Fused Filament Fabrication. JMMP 5, 69. https://doi.org/10.3390/jmmp5030069

Di Gioia, L., Cuq, B., Guilbert, S., 1999. Thermal properties of corn gluten meal and its proteic components. International Journal of Biological Macromolecules 24, 341–350. https://doi.org/10.1016/S0141-8130(99)00048-3

Di Gioia, L., Guilbert, S., 1999. Corn Protein-Based Thermoplastic Resins: Effect of Some Polar and Amphiphilic Plasticizers. J. Agric. Food Chem. 47, 1254–1261. https://doi.org/10.1021/jf980976j

Dudderar, T.D., Koch, F.B., Doerries, E.M., 1977. Measurement of the shapes of foil bulge-test samples: Post-test shapes of bulge samples are determined by optical contouring. Radius-of-curvature distributions are evaluated using computer-based polynomial-spline fitting routines to analyze the resulting interferometric-fringe data. Experimental Mechanics 17, 133–140. https://doi.org/10.1007/bf02324211

Dufour, M., Chaunier, L., Hugon, F., Dugué, A., Kansou, K., Saulnier, L., Della Valle, G., 2024. From Alveograph test to extensional behavior of wheat flour dough. Rheol Acta 63, 179–190. https://doi.org/10.1007/s00397-024-01430-6

Duty, C., Ajinjeru, C., Kishore, V., Compton, B., Hmeidat, N., Chen, X., Liu, P., Hassen, A.A., Lindahl, J., Kunc, V., 2018. What makes a material printable? A viscoelastic model for extrusion-based 3D printing of polymers. Journal of Manufacturing Processes 35, 526–537. https://doi.org/10.1016/j.jmapro.2018.08.008

Ebnesajjad, S., 2016. Effect of Chemicals on Plastics, in: Chemical Resistance of Commodity Thermoplastics. Elsevier, pp. xxvii–xli. https://doi.org/10.1016/B978-0-323-47358-3.00018-1

Ebrahimi, R., Lotfabad, F.R., 2022. A Comprehensive Mathematical Analysis on Achieving Stress–Strain Behavior at Large Strains in Bulge Test. Iran J Sci Technol Trans Mech Eng 46, 901–909. https://doi.org/10.1007/s40997-021-00451-3

Edward, S., Golecki, H.M., 2023. Gelatin Soft Actuators: Benefits and Opportunities. Actuators 12, 63. https://doi.org/10.3390/act12020063

Elango, N., Faudzi, A.A.M., 2015. A review article: investigations on soft materials for soft robot manipulations. Int J Adv Manuf Technol 80, 1027–1037. https://doi.org/10.1007/s00170-015-7085-3

Enrione, J., Osorio, F., Pedreschi, F., Hill, S., 2010. Prediction of the Glass Transition Temperature on Extruded Waxy Maize and Rice Starches in Presence of Glycerol. Food Bioprocess Technol 3, 791–796. https://doi.org/10.1007/s11947-010-0345-1

Eslami, Z., Elkoun, S., Robert, M., Adjallé, K., 2023. A Review of the Effect of Plasticizers on the Physical and Mechanical Properties of Alginate-Based Films. Molecules 28, 6637. https://doi.org/10.3390/molecules28186637

Floreano, D., Kwak, B., Pankhurst, M., Shintake, J., Caironi, M., Annese, V.F., Qi, Q., Rossiter, J., Boom, R.M., 2024. Towards edible robots and robotic food. Nat Rev Mater. https://doi.org/10.1038/s41578-024-00688-9

Friedrich, Chr., Braun, H., 1992. Generalized Cole-Cole behavior and its rheological relevance. Rheola Acta 31, 309–322. https://doi.org/10.1007/BF00418328

Gao, C., Pollet, E., Avérous, L., 2017. Properties of glycerol-plasticized alginate films obtained by thermo-mechanical mixing. Food Hydrocolloids 63, 414–420. https://doi.org/10.1016/j.foodhyd.2016.09.023

Gilmer, E.L., Miller, D., Chatham, C.A., Zawaski, C., Fallon, J.J., Pekkanen, A., Long, T.E., Williams, C.B., Bortner, M.J., 2018. Model analysis of feedstock behavior in fused filament fabrication: Enabling rapid materials screening. Polymer 152, 51–61. https://doi.org/10.1016/j.polymer.2017.11.068

Godoi, F.C., Prakash, S., Bhandari, B.R., 2016a. 3d printing technologies applied for food design: Status and prospects. Journal of Food Engineering 179, 44–54. https://doi.org/10.1016/j.jfoodeng.2016.01.025

Godoi, F.C., Prakash, S., Bhandari, B.R., 2016b. 3d printing technologies applied for food design: Status and prospects. Journal of Food Engineering 179, 44–54. https://doi.org/10.1016/j.jfoodeng.2016.01.025

Gontard, N., Ring, S., 1996. Edible Wheat Gluten Film: Influence of Water Content on Glass Transition Temperature. J. Agric. Food Chem. 44, 3474–3478. https://doi.org/10.1021/jf960230q

Güner, A., Brosius, A., Tekkaya, A.E., 2009. Analysis of the Hydraulic Bulge Test with FEA Concerning the Accuracy of the Determined Flow Curves. Key Engineering Materials 410–411, 439–447. https://doi.org/10.4028/www.scientific.net/KEM.410-411.439

Guo, J., Liu, Y.-C., Yang, X.-Q., Jin, Y.-C., Yu, S.-J., Wang, J.-M., Hou, J.-J., Yin, S.-W., 2014. Fabrication of edible gellan gum/soy protein ionic-covalent entanglement gels with diverse mechanical and oral processing properties. Food Research International 62, 917–925. https://doi.org/10.1016/j.foodres.2014.05.014

Hallfeldt, T., Hotz, W., Leppin, C., Keller, S., Friebe, H., Till, E.T., Müller, R., Vučetić, M., Vegter, H., 2014. Sheet Bulge Testing, in: Comprehensive Materials Processing. Elsevier, pp. 85–93. https://doi.org/10.1016/B978-0-08-096532-1.00105-9

Hartmann, F., Baumgartner, M., Kaltenbrunner, M., 2021. Becoming Sustainable, The New Frontier in Soft Robotics. Advanced Materials 33, 2004413. https://doi.org/10.1002/adma.202004413

Heiden, A., Preninger, D., Lehner, L., Baumgartner, M., Drack, M., Woritzka, E., Schiller, D., Gerstmayr, R., Hartmann, F., Kaltenbrunner, M., 2022. 3D printing of resilient biogels for omnidirectional and exteroceptive soft actuators. Sci. Robot. 7, eabk2119. https://doi.org/10.1126/scirobotics.abk2119

Hernandez-Izquierdo, V.M., Krochta, J.M., 2008. Thermoplastic Processing of Proteins for Film Formation—A Review. J Food Science 73, R30–R39. https://doi.org/10.1111/j.1750-3841.2007.00636.x

Hill, R., 1950. C. A theory of the plastic bulging of a metal diaphragm by lateral pressure. The London, Edinburgh, and Dublin Philosophical Magazine and Journal of Science 41, 1133–1142. https://doi.org/10.1080/14786445008561154

Hong, S., Sycks, D., Chan, H.F., Lin, S., Lopez, G.P., Guilak, F., Leong, K.W., Zhao, X., 2015. 3D Printing of Highly Stretchable and Tough Hydrogels into Complex, Cellularized Structures. Adv Mater 27, 4035–4040. https://doi.org/10.1002/adma.201501099

Huang, C.K., Lou, W.M., Tsai, C.J., Wu, T.-C., Lin, H.-Y., 2007. Mechanical properties of polymer thin film measured by the bulge test. Thin Solid Films 515, 7222–7226. https://doi.org/10.1016/j.tsf.2007.01.058

Huang, J.-C., 2002. Carbon black filled conducting polymers and polymer blends. Advances in Polymer Technology 21, 299–313. https://doi.org/10.1002/adv.10025

Hur, J., Im, K., Kim, S.W., Kim, J., Chung, D.-Y., Kim, T.-H., Jo, K.H., Hahn, J.H., Bao, Z., Hwang, S., Park, N., 2014. Polypyrrole/Agarose-Based Electronically Conductive and Reversibly Restorable Hydrogel. ACS Nano 8, 10066–10076. https://doi.org/10.1021/nn502704g

Hwang, U., Moon, H., Park, J., Jung, H.W., 2024. Crosslinking and Swelling Properties of pH-Responsive Poly(Ethylene Glycol)/Poly(Acrylic Acid) Interpenetrating Polymer Network Hydrogels. Polymers 16, 2149. https://doi.org/10.3390/polym16152149

Jacobsen, S., Fritz, H.G., 1999. Plasticizing polylactide—the effect of different plasticizers on the mechanical properties. Polymer Engineering & Sci 39, 1303–1310. https://doi.org/10.1002/pen.11517

Janes, M.E., Dai, Y., 2012. Edible films for meat, poultry and seafood, in: Advances in Meat, Poultry and Seafood Packaging. Elsevier, pp. 504–521. https://doi.org/10.1533/9780857095718.4.504

Jeong, D., Kim, C., Kim, Y., Jung, S., 2020. Dual crosslinked carboxymethyl cellulose/polyacrylamide interpenetrating hydrogels with highly enhanced mechanical strength and superabsorbent properties. European Polymer Journal 127, 109586. https://doi.org/10.1016/j.eurpolymj.2020.109586

Joardder, M.U.H., Kumar, C., Karim, M.A., 2017. Food structure: Its formation and relationships with other properties. Critical Reviews in Food Science and Nutrition 57, 1190–1205. https://doi.org/10.1080/10408398.2014.971354

Jødal, A.-S.S., Larsen, K.L., 2021. Investigation of the relationships between the alveograph parameters. Sci Rep 11. https://doi.org/10.1038/s41598-021-84959-3

Kalichevsky, M.T., Blanshard, J.M.V., Tokargzuk, P.F., 1993. Effect of water content and sugars on the glass transition of casein and sodium caseinate. Int J of Food Sci Tech 28, 139–151. https://doi.org/10.1111/j.1365-2621.1993.tb01259.x

Kalichevsky, M.T., Jaroszkiewicz, E.M., Ablett, S., Blanshard, J.M.V., Lillford, P.J., 1992. The glass transition of amylopectin measured by DSC, DMTA and NMR. Carbohydrate Polymers 18, 77–88. https://doi.org/10.1016/0144-8617(92)90129-E

Kanno, R., Kwak, B., Pankhurst, M., Shintake, J., Floreano, D., 2024. Edible soft actuators based on konjac glucomannan for underwater operation. Advanced Intelligent Systems 6, 2300473.

Kasaai, M.R., 2018. Zein and zein -based nano-materials for food and nutrition applications: A review. Trends in Food Science & Technology 79, 184–197. https://doi.org/10.1016/j.tifs.2018.07.015

Kaya, S., Altan, T., Groche, P., Klöpsch, C., 2008. Determination of the flow stress of magnesium AZ31-O sheet at elevated temperatures using the hydraulic bulge test. International Journal of Machine Tools and Manufacture, Advances in Sheet Metal Forming Applications 48, 550–557. https://doi.org/10.1016/j.ijmachtools.2007.06.011

Khalesi, H., Lu, W., Nishinari, K., Fang, Y., 2020. New insights into food hydrogels with reinforced mechanical properties: A review on innovative strategies. Advances in Colloid and Interface Science 285, 102278. https://doi.org/10.1016/j.cis.2020.102278

Khwaldia, K., Banon, S., Perez, C., Desobry, S., 2004. Properties of Sodium Caseinate Film-Forming Dispersions and Films. Journal of Dairy Science 87, 2011–2016. https://doi.org/10.3168/jds.S0022-0302(04)70018-1

Kianirad, S., MokhtariHosseini, Z.B., HatamianZaremi, A., Sarsangi, M., AfsharYegane, S., Setareyi, R., AziziAlavijeh, A., Haddadi, M., 2021. Preparation and Study of Physical Properties of Zein Based Composite Films as Food Coatings. Int. J. Adv. Biol. Biomed. Res. 9. https://doi.org/10.22034/ijabbr.2021.522968.1342

Knothe, G., Dunn, R.O., 2009. A Comprehensive Evaluation of the Melting Points of Fatty Acids and Esters Determined by Differential Scanning Calorimetry. J Americ Oil Chem Soc 86, 843–856. https://doi.org/10.1007/s11746-009-1423-2

Knothe, G., Steidley, K.R., 2005. Kinematic viscosity of biodiesel fuel components and related compounds. Influence of compound structure and comparison to petrodiesel fuel components. Fuel 84, 1059–1065. https://doi.org/10.1016/j.fuel.2005.01.016

Kozempel, M., Tomasula, P.M., 2004. Development of a Continuous Process To Make Casein Films. J. Agric. Food Chem. 52, 1190–1195. https://doi.org/10.1021/jf0304573

Krieger, I.M., Dougherty, T.J., 1959. A Mechanism for Non-Newtonian Flow in Suspensions of Rigid Spheres. Transactions of The Society of Rheology 3, 137–152. https://doi.org/10.1122/1.548848

Krpovic, S., Dam-Johansen, K., Skov, A.L., 2021. Importance of Mullins effect in commercial silicone elastomer formulations for soft robotics. Journal of Applied Polymer Science 138, 50380. https://doi.org/10.1002/app.50380

Kruglov, A.A., Enikeev, F.U., Lutfullin, R.Ya., 2002. Superplastic forming of a spherical shell out a welded envelope. Materials Science and Engineering: A 323, 416–426. https://doi.org/10.1016/S0921-5093(01)01376-4

Lai, H., Padua, G.W., 1997. Properties and Microstructure of Plasticized Zein Films. Cereal Chem 74, 771–775. https://doi.org/10.1094/CCHEM.1997.74.6.771

Lawton, J.W., 2004. Plasticizers for Zein: Their Effect on Tensile Properties and Water Absorption of Zein Films. Cereal Chem 81, 1–5. https://doi.org/10.1094/CCHEM.2004.81.1.1

Lazarescu, L., Comsa, D.S., Banabic, D., 2011. Analytical and Experimental Evaluation of the Stress-Strain Curves of Sheet Metals by Hydraulic Bulge Tests. KEM 473, 352–359. https://doi.org/10.4028/www.scientific.net/KEM.473.352

Le, A.-D., Cosson, B., Asséko, A.C.A., 2021. Simulation of large-scale additive manufacturing process with a single-phase level set method: a process parameters study. Int J Adv Manuf Technol 113, 3343–3360. https://doi.org/10.1007/s00170-021-06703-5

Leceta, I., Etxabide, A., Cabezudo, S., De La Caba, K., Guerrero, P., 2014. Bio-based films prepared with by-products and wastes: environmental assessment. Journal of Cleaner Production 64, 218–227. https://doi.org/10.1016/j.jclepro.2013.07.054

Li, J., Ma, P.C., Chow, W.S., To, C.K., Tang, B.Z., Kim, J.-K., 2007. Correlations between Percolation Threshold, Dispersion State, and Aspect Ratio of Carbon Nanotubes. Advanced Functional Materials 17, 3207–3215. https://doi.org/10.1002/adfm.200700065

Li, J., Qiu, Y., Wang, H., Wang, Z., 2019. Estimation of the Strength Coefficient and Strain Hardening Exponent from Monotonic Tensile Properties of Steels. Int J Steel Struct 19, 1951–1968. https://doi.org/10.1007/s13296-019-00256-w

Li, L., Guan, S., Yang, L., Qin, X., Feng, W., 2018. Mechanical and Adhesive Properties of Ploy(ethylene glycerol) Diacrylate Based Hydrogels Plasticized with PEG and Glycerol. Chem. Res. Chin. Univ. 34, 311–317. https://doi.org/10.1007/s40242-018-7337-5

Li, X., Xu, H., Yang, Q., Long, S., Yuan, Y., Chen, M., 2018. Sodium alginate-agar dual-network high-strength natural hydrogel material, and preparation method thereof.

Lide, D.R., 2006. Handbook of chemistry and physics, 88th edn. ed. CRC, cop.

Lie-Piang, A., Möller, A.C., Köllmann, N., Garre, A., Boom, R., van der Padt, A., 2022. Functionality-driven food product formulation – An illustration on selecting

sustainable ingredients building viscosity. Food Research International 152, 110889. https://doi.org/10.1016/j.foodres.2021.110889

Lille, M., Nurmela, A., Nordlund, E., Metsä-Kortelainen, S., Sozer, N., 2018. Applicability of protein and fiber-rich food materials in extrusion-based 3D printing. Journal of Food Engineering, 3D Printed Food – Design and Technology 220, 20–27. https://doi.org/10.1016/j.jfoodeng.2017.04.034

Lin, F., Lu, X., Wang, Z., Lu, Q., Lin, G., Huang, B., Lu, B., 2019. In situ polymerization approach to cellulose–polyacrylamide interpenetrating network hydrogel with high strength and pH-responsive properties. Cellulose 26, 1825–1839. https://doi.org/10.1007/s10570-018-2171-y

Lin, P., Ma, S., Wang, X., Zhou, F., 2015. Molecularly Engineered Dual-Crosslinked Hydrogel with Ultrahigh Mechanical Strength, Toughness, and Good Self-Recovery. Advanced Materials 27, 2054–2059. https://doi.org/10.1002/adma.201405022

Liu, F., Chiou, B.-S., Avena-Bustillos, R.J., Zhang, Y., Li, Y., McHugh, T.H., Zhong, F., 2017. Study of combined effects of glycerol and transglutaminase on properties of gelatin films. Food Hydrocolloids 65, 1–9. https://doi.org/10.1016/j.foodhyd.2016.10.004

Liu, S., Zheng, R., Chen, S., Wu, Y., Liu, H., Wang, P., Deng, Z., Liu, L., 2018. A compliant, self-adhesive and self-healing wearable hydrogel as epidermal strain sensor. Journal of Materials Chemistry C 6, 4183–4190. https://doi.org/10.1039/C8TC00157J

Ma, Y., Schutyser, M.A.I., Boom, R.M., Zhang, L., 2024. Quantification of fracture mechanics with digital image correlation guides the infill design of 3D-printed snack bars with modulated flexural properties. Virtual and Physical Prototyping 19, e2349679. https://doi.org/10.1080/17452759.2024.2349679

Ma, Y., Schutyser, M.A.I., Boom, R.M., Zhang, L., 2022. Thermographic and rheological characterization of viscoelastic materials for hot-extrusion 3D food printing. Innovative Food Science & Emerging Technologies 81, 103135. https://doi.org/10.1016/j.ifset.2022.103135

Mackay, M.E., 2018. The importance of rheological behavior in the additive manufacturing technique material extrusion. J. Rheol. 62, 1549–1561. https://doi.org/10.1122/1.5037687

Maidannyk, V.A., Roos, Y.H., 2016. Modification of the WLF model for characterization of the relaxation time-temperature relationship in trehalose-whey protein isolate systems. Journal of Food Engineering 188, 21–31. https://doi.org/10.1016/j.jfoodeng.2016.05.006

Mattice, K.D., Marangoni, A.G., 2020. Comparing methods to produce fibrous material from zein. Food Research International 128, 108804. https://doi.org/10.1016/j.foodres.2019.108804

Min, J., Stoughton, T.B., Carsley, J.E., Carlson, B.E., Lin, J., Gao, X., 2017. Accurate characterization of biaxial stress-strain response of sheet metal from bulge

testing. International Journal of Plasticity 94, 192–213. https://doi.org/10.1016/j.ijplas.2016.02.005

Mio, L., Sacco, P., Donati, I., 2022. Influence of Temperature and Polymer Concentration on the Nonlinear Response of Highly Acetylated Chitosan–Genipin Hydrogels. Gels 8, 194. https://doi.org/10.3390/gels8030194

Mulder, J., Vegter, H., Aretz, H., Keller, S., Van Den Boogaard, A.H., 2015. Accurate determination of flow curves using the bulge test with optical measuring systems. Journal of Materials Processing Technology 226, 169–187. https://doi.org/10.1016/j.jmatprotec.2015.06.034

Mulder, J., Vegter, H., Aretz, H., Van Den Boogaard, T., 2013. Accurate Evaluation Method for the Hydraulic Bulge Test. KEM 554–557, 33–40. https://doi.org/10.4028/www.scientific.net/KEM.554-557.33

Myung, D., Koh, W., Ko, J., Hu, Y., Carrasco, M., Noolandi, J., Ta, C.N., Frank, C.W., 2007. Biomimetic strain hardening in interpenetrating polymer network hydrogels. Polymer 48, 5376–5387. https://doi.org/10.1016/j.polymer.2007.06.070

Nachal, N., Moses, J.A., Karthik, P., Anandharamakrishnan, C., 2019. Applications of 3D Printing in Food Processing. Food Eng Rev 11, 123–141. https://doi.org/10.1007/s12393-019-09199-8

Nath, P.C., Debnath, S., Sridhar, K., Inbaraj, B.S., Nayak, P.K., Sharma, M., 2022. A Comprehensive Review of Food Hydrogels: Principles, Formation Mechanisms, Microstructure, and Its Applications. Gels 9, 1. https://doi.org/10.3390/gels9010001

Niu, Y., Xia, Q., Gu, M., Yu, L. (Lucy), 2019. Interpenetrating network gels composed of gelatin and soluble dietary fibers from tomato peels. Food Hydrocolloids 89, 95–99. https://doi.org/10.1016/j.foodhyd.2018.10.028

Oechsle, A.M., Häupler, M., Weigel, F., Gibis, M., Kohlus, R., Weiss, J., 2016. Modulation of extruded collagen films by the addition of co-gelling proteins. Journal of Food Engineering 171, 164–173. https://doi.org/10.1016/j.jfoodeng.2015.10.004

Panteli, P.A., Patrickios, C.S., 2019. Multiply Interpenetrating Polymer Networks: Preparation, Mechanical Properties, and Applications. Gels 5, 36. https://doi.org/10.3390/gels5030036

Permadi, A., Hidayah, N., Simamora, W.I., Imanuel, C., Endah, G.W., Nurbani, S.Z., Sayuti, M., Dharmayanti, N., Afifah, R.A., 2024. Characterization of Sodium Alginate-Based Edible Film with Addition of Gelatin and Casein. BIO Web Conf. 87, 01007. https://doi.org/10.1051/bioconf/20248701007

Pommet, M., Redl, A., Morel, M.-H., Guilbert, S., 2003. Study of wheat gluten plasticization with fatty acids. Polymer 44, 115–122. https://doi.org/10.1016/S0032-3861(02)00746-2

Portanguen, S., Tournayre, P., Sicard, J., Astruc, T., Mirade, P.-S., 2019. Toward the design of functional foods and biobased products by 3D printing: A review. Trends in Food Science & Technology 86, 188–198. https://doi.org/10.1016/j.tifs.2019.02.023

Poveda-Reyes, S., Mellera-Oglialoro, L.R., Martínez-Haya, R., Gamboa-Martínez, T.C., Gómez Ribelles, J.L., Gallego Ferrer, G., 2015. Reinforcing an Injectable Gelatin Hydrogel with PLLA Microfibers: Two Routes for Short Fiber Production. Macromolecular Materials and Engineering 300, 977–988. https://doi.org/10.1002/mame.201500033

Purcell, T., Delaplace, G., Riaublanc, A., Demême, M., Derensy, A., Della Valle, G., 2025. A general viscosity model for high moisture extrudates of pea protein isolates/gluten blend. Physics of Fluids 37, 033120. https://doi.org/10.1063/5.0256835

Rahman, M.S., Al-Marhubi, I.M., Al-Mahrouqi, A., 2007. Measurement of glass transition temperature by mechanical (DMTA), thermal (DSC and MDSC), water diffusion and density methods: A comparison study. Chemical Physics Letters 440, 372–377. https://doi.org/10.1016/j.cplett.2007.04.067

Rauwendaal, C., 2014. Different types of extruders. Polymer Extrusion 11–33.

Rees, D.W.A., 1995. Plastic flow in the elliptical bulge test. International Journal of Mechanical Sciences 37, 373–389. https://doi.org/10.1016/0020-7403(94)00071-Q

Ren, D., Zheng, S., Wu, F., Yang, W., Liu, Z., Yang, M., 2014. Formation and evolution of the carbon black network in polyethylene/carbon black composites: Rheology and conductivity properties. J of Applied Polymer Sci 131, app.39953. https://doi.org/10.1002/app.39953

Renzetti, S., Van Den Hoek, I.A.F., Van Der Sman, R.G.M., 2021. Mechanisms controlling wheat starch gelatinization and pasting behaviour in presence of sugars and sugar replacers: Role of hydrogen bonding and plasticizer molar volume. Food Hydrocolloids 119, 106880. https://doi.org/10.1016/j.foodhyd.2021.106880

Rowat, S.Ja., Legge, R.L., Moresoli, C., 2021. Plant protein in material extrusion 3D printing: Formation, plasticization, prospects, and challenges. Journal of Food Engineering 308, 110623. https://doi.org/10.1016/j.jfoodeng.2021.110623

Rüegg, M., Moor, U., 1984. Effect of calcium on the hydration of casein. I. Water vapour sorption and fine structure of calcium caseinates compared with sodium caseinates in the pH range 4·6–8·0. Journal of Dairy Research 51, 103–111. https://doi.org/10.1017/S0022029900023360

Rusli, A., 2017. Physical and mechanical properties of agar based edible film with glycerol plasticizer. https://doi.org/10.31227/osf.io/tq2pf

Sanchez, L.C., Beatrice, C.A.G., Lotti, C., Marini, J., Bettini, S.H.P., Costa, L.C., 2019. Rheological approach for an additive manufacturing printer based on material extrusion. Int J Adv Manuf Technol 105, 2403–2414. https://doi.org/10.1007/s00170-019-04376-9

Schreiber, F., Frohn-Sörensen, P., Engel, B., Manns, M., 2025. Applicability of models to predict the bending behavior of soft pneumatic grippers. Int J Adv Manuf Technol 138, 273–286. https://doi.org/10.1007/s00170-025-15497-9

Schröter, K., Donth, E., 2000. Viscosity and shear response at the dynamic glass transition of glycerol. The Journal of Chemical Physics 113, 9101–9108. https://doi.org/10.1063/1.1319616

Schutyser, M.A.I., Houlder, S., De Wit, M., Buijsse, C.A.P., Alting, A.C., 2018. Fused deposition modelling of sodium caseinate dispersions. Journal of Food Engineering 220, 49–55. https://doi.org/10.1016/j.jfoodeng.2017.02.004

Sears, J.K., Darby, J.R., 1982. The technology of plasticizers. (No Title).

Selling, G.W., 2010. The effect of extrusion processing on Zein. Polymer Degradation and Stability 95, 2241–2249. https://doi.org/10.1016/j.polymdegradstab.2010.09.013

Shi, H., Li, J., Xu, E., Yang, H., Liu, D., Yin, J., 2023. Microscale 3D printing of fish analogues using soy protein food ink. Journal of Food Engineering 347, 111436. https://doi.org/10.1016/j.jfoodeng.2023.111436

Shintake, J., Sonar, H., Piskarev, E., Paik, J., Floreano, D., 2017. Soft Pneumatic Gelatin Actuator for Edible Robotics.

Siemons, I., Veser, J., Boom, R.M., Schutyser, M.A.I., van der Sman, R.G.M., 2022. Rheological behaviour of concentrated maltodextrins describes skin formation and morphology development during droplet drying. Food Hydrocolloids 126, 107442. https://doi.org/10.1016/j.foodhyd.2021.107442

Skrdla, P.J., Floyd, P.D., Dell'Orco, P.C., 2017. The amorphous state: first-principles derivation of the Gordon–Taylor equation for direct prediction of the glass transition temperature of mixtures; estimation of the crossover temperature of fragile glass formers; physical basis of the "Rule of 2/3." Phys. Chem. Chem. Phys. 19, 20523–20532. https://doi.org/10.1039/C7CP04124A

Smith, A.M., Inocencio, D.G., Pardi, B.M., Gopinath, A., Andresen Eguiluz, R.C., 2024. Facile Determination of the Poisson's Ratio and Young's Modulus of Polyacrylamide Gels and Polydimethylsiloxane. ACS Appl. Polym. Mater. 6, 2405–2416. https://doi.org/10.1021/acsapm.3c03154

Sola, A., 2022. Materials Requirements in Fused Filament Fabrication: A Framework for the Design of Next-Generation 3D Printable Thermoplastics and Composites. Macro Materials & Eng 307, 2200197. https://doi.org/10.1002/mame.202200197

Sou, K., Nishikawa, K., Koga, Y., Tozaki, K., 2011. High-resolution calorimetry on thermal behavior of glycerol (I): Glass transition, crystallization and melting, and discovery of a solid–solid transition. Chemical Physics Letters 506, 217–220. https://doi.org/10.1016/j.cplett.2011.03.043

Spoerk, M., Arbeiter, F., Cajner, H., Sapkota, J., Holzer, C., 2017. Parametric optimization of intra- and inter-layer strengths in parts produced by extrusion-based additive manufacturing of poly(lactic acid). J of Applied Polymer Sci 134, 45401. https://doi.org/10.1002/app.45401

Stachowicz, F., Rzeszowska, P., 2003. Biaxial Stress-Strain Relationship Of Sheet Metal From Hydraulic Bulging Test. Presented at the 5th International Multidisciplinary Conference.

Steffens, Q., Vliek, M., Van Der Sman, R., Boom, R., Zhang, L., 2025. 3D-printing of thermoplastic protein-based composites by fused deposition modelling. Journal of Food Engineering 401, 112660. https://doi.org/10.1016/j.jfoodeng.2025.112660

Sun, J.-Y., Zhao, X., Illeperuma, W.R.K., Chaudhuri, O., Oh, K.H., Mooney, D.J., Vlassak, J.J., Suo, Z., 2012. Highly stretchable and tough hydrogels. Nature 489, 133–136. https://doi.org/10.1038/nature11409

Sun, X., Liang, H., Ye, L., 2024. Strong, tough and conductive single-network hydrogels based on deswelling and the salting-out effect. Soft Matter 20, 3771–3779. https://doi.org/10.1039/D4SM00298A

Suo, H., Zhang, D., Yin, J., Qian, J., Wu, Z., Fu, J., 2018. Interpenetrating polymer network hydrogels composed of chitosan and photocrosslinkable gelatin with enhanced mechanical properties for tissue engineering. Materials science & engineering. C, Materials for biological applications 92, 612–620. https://doi.org/10.1016/j.msec.2018.07.016

Tallawi, M., Amrein, D., Gemmecker, G., Aifantis, K.E., Drechsler, K., 2023. A novel polysaccharide/zein conjugate as an alternative green plastic. Sci Rep 13, 13161. https://doi.org/10.1038/s41598-023-40293-4

Tang, X., Li, H., Ma, T., Yang, Y., Luo, J., Wang, H., Jiang, P., 2022. A Review of Soft Actuator Motion: Actuation, Design, Manufacturing and Applications. Actuators 11, 331. https://doi.org/10.3390/act11110331

Tavares-Negrete, J.A., Aceves-Colin, A.E., Rivera-Flores, D.C., Díaz-Armas, G.G., Mertgen, A.-S., Trinidad-Calderón, P.A., Olmos-Cordero, J.M., Gómez-López, E.G., Pérez-Carrillo, E., Escobedo-Avellaneda, Z.J., Tamayol, A., Moisés Alvarez, M., Trujillo-de Santiago, G., 2020. Biofabrication using maize protein: 3D printing using zein formulations (preprint). Bioengineering. https://doi.org/10.1101/2020.07.29.227744

Thadasack, M., Reguerre, A.-L., Leroy, E.B.M., Guessasma, S., Denis, L., Weitkamp, T., Chaunier, L., 2023. Tuning Pharmaceutically Active Zein-Based Formulations for Additive Manufacturing. https://doi.org/10.2139/ssrn.4558465

Tillekeratne, M., Easteal, A.J., 2000. Modification of zein films by incorporation of poly(ethylene glycol)s. Polym. Int. 49, 127–134. https://doi.org/10.1002/(SICI)1097-0126(200001)49:1%253C127::AID-PI320%253E3.0.CO;2-B

Vaes, D., Van Puyvelde, P., 2021. Semi-crystalline feedstock for filament-based 3D printing of polymers. Progress in Polymer Science 118, 101411. https://doi.org/10.1016/j.progpolymsci.2021.101411

van der Sman, R., Renzetti, S., Voudouris, P., Asghari, A., Khalloufi, S., 2026. Correlation of T2 NMR with Tg/T<math><mrow is="true"><msub is="true"><mrow is="true"><mi is="true">T</mi></mrow><mrow is="true"><mi is="true">g</mi></mrow></msub><mo is="true">/</mo><mi is="true">T</mi></mrow></math> and viscosity. Current Research in Food Science 12, 101309. https://doi.org/10.1016/j.crfs.2026.101309

Van Der Sman, R.G.M., 2025. Modelling Thermodynamics of Food Plasticizers. https://doi.org/10.1039/9781837676699-00072

van der Sman, R.G.M., 2012. Thermodynamics of meat proteins. Food Hydrocolloids 27, 529–535. https://doi.org/10.1016/j.foodhyd.2011.08.016

Van Der Sman, R.G.M., Chakraborty, P., Hua, N.P., Kollmann, N., 2023. Scaling relations in rheology of proteins present in meat analogs. Food Hydrocolloids 135, 108195. https://doi.org/10.1016/j.foodhyd.2022.108195

van der Sman, R.G.M., Chakraborty, P., Hua, N.P., Kollmann, N., 2023. Scaling relations in rheology of proteins present in meat analogs. Food Hydrocolloids 135, 108195. https://doi.org/10.1016/j.foodhyd.2022.108195

Van Der Sman, R.G.M., Renzetti, S., Tian, B., 2024. Rheology of edible soft glassy materials. Food Hydrocolloids 149, 109586. https://doi.org/10.1016/j.foodhyd.2023.109586

Venkatachalam, A., Balasubramaniam, A., Wilms, P.F.C., Zhang, L., Schutyser, M.A.I., 2023a. Impact of varying macronutrient composition on the printability of pea-based inks in extrusion-based 3D food printing. Food Hydrocolloids 142, 108760. https://doi.org/10.1016/j.foodhyd.2023.108760

Venkatachalam, A., Balasubramaniam, A., Wilms, P.F.C., Zhang, L., Schutyser, M.A.I., 2023b. Impact of varying macronutrient composition on the printability of pea-based inks in extrusion-based 3D food printing. Food Hydrocolloids 142, 108760. https://doi.org/10.1016/j.foodhyd.2023.108760

Walker, S., Rueben, J., Volkenburg, T.V., Hemleben, S., Grimm, C., Simonsen, J., Mengüç, Y., 2017. Using an environmentally benign and degradable elastomer in soft robotics. Int J Intell Robot Appl 1, 124–142. https://doi.org/10.1007/s41315-017-0016-8

Wallin, T.J., Pikul, J., Shepherd, R.F., 2018. 3D printing of soft robotic systems. Nat Rev Mater 3, 84–100. https://doi.org/10.1038/s41578-018-0002-2

Wang, S., Chen, H., Tong, Y., Li, Y., Zhang, J., Chen, C., Ren, F., Hou, C., Wang, P., 2023. Composite films with properties improved by increasing the compatibility of sodium caseinate and zein in a heated 60% ethanol solvent. Food Hydrocolloids 134, 108017. https://doi.org/10.1016/j.foodhyd.2022.108017

Wang, X., Chen, Y., Zhao, X., Pang, J., 2025. Incorporating Fatty Acids Enhanced the Performance of Konjac Glucomannan/Chitosan/Zein Film. Foods 14. https://doi.org/10.3390/foods14091563

Wang, Y., Padua, G.W., 2003. Tensile Properties of Extruded Zein Sheets and Extrusion Blown Films. Macro Materials & Eng 288, 886–893. https://doi.org/10.1002/mame.200300069

Whitcomb, K., 2023. RH107 Determining the Linear Viscoelastic Region in Oscillatory Measurements.

Williams, M.L., Landel, R.F., Ferry, J.D., 1955. The temperature dependence of relaxation mechanisms in amorphous polymers and other glass-forming liquids. Journal of the American Chemical society 77, 3701–3707.

Wittaya, T., 2012. Protein-Based Edible Films: Characteristics and Improvement of Properties, in: Structure and Function of Food Engineering. InTech. https://doi.org/10.5772/48167

Xavier, M.S., Tawk, C.D., Zolfagharian, A., Pinskier, J., Howard, D., Young, T., Lai, J., Harrison, S.M., Yong, Y.K., Bodaghi, M., Fleming, A.J., 2022. Soft Pneumatic Actuators: A Review of Design, Fabrication, Modeling, Sensing, Control and Applications. IEEE Access 10, 59442–59485. https://doi.org/10.1109/ACCESS.2022.3179589

Xia, H., Lu, J., Dabiri, S., Tryggvason, G., 2018. Fully resolved numerical simulations of fused deposition modeling. Part I: fluid flow. RPJ 24, 463–476. https://doi.org/10.1108/RPJ-12-2016-0217

Xu, H., Chai, Y., Zhang, G., 2012. Synergistic Effect of Oleic Acid and Glycerol on Zein Film Plasticization. J. Agric. Food Chem. 60, 10075–10081. https://doi.org/10.1021/jf302940j

Xu, J., Guo, Z., Chen, Y., Luo, Y., Xie, S., Zhang, Y., Tan, H., Xu, L., Zheng, J., 2021. Tough, adhesive, self-healing, fully physical crosslinked κ-CG-K+/pHEAA double-network ionic conductive hydrogels for wearable sensors. Polymer 236, 124321. https://doi.org/10.1016/j.polymer.2021.124321

Yan, X., Chen, Q., Zhu, L., Chen, H., Wei, D., Chen, F., Tang, Z., Yang, J., Zheng, J., 2017. High strength and self-healable gelatin/polyacrylamide double network hydrogels. Journal of Materials Chemistry B 5, 7683–7691. https://doi.org/10.1039/C7TB01780D

Yang, F., Tadepalli, V., Wiley, B.J., 2017. 3D Printing of a Double Network Hydrogel with a Compression Strength and Elastic Modulus Greater than those of Cartilage. ACS Biomater. Sci. Eng. 3, 863–869. https://doi.org/10.1021/acsbiomaterials.7b00094

Yildirim, M., Hettiarachchy, N. s., 1998. Properties of Films Produced by Cross-linking Whey Proteins and 11S Globulin Using Transglutaminase. Journal of Food Science 63, 248–252. https://doi.org/10.1111/j.1365-2621.1998.tb15719.x

Yin, S., Yao, D.R., Song, Y., Heng, W., Ma, X., Han, H., Gao, W., 2024. Wearable and Implantable Soft Robots. Chem. Rev. 124, 11585–11636. https://doi.org/10.1021/acs.chemrev.4c00513

Yoo, S., Krochta, J.M., 2011. Whey protein–polysaccharide blended edible film formation and barrier, tensile, thermal and transparency properties. J Sci Food Agric 91, 2628–2636. https://doi.org/10.1002/jsfa.4502

Zhan, L., Qu, S., Xiao, R., 2024. A Review on the Mullins Effect in Tough Elastomers and Gels. Acta Mech. Solida Sin. 37, 181–214. https://doi.org/10.1007/s10338-023-00460-6

Zhang, H., Düring, L., Kovacs, G., Yuan, W., Niu, X., Pei, Q., 2010. Interpenetrating polymer networks based on acrylic elastomers and plasticizers with improved actuation

temperature range. Polymer International 59, 384–390. https://doi.org/10.1002/pi.2784

Zhang, L., Liu, J., Zheng, X., Zhang, A., Zhang, X., Tang, K., 2019. Pullulan dialdehyde crosslinked gelatin hydrogels with high strength for biomedical applications. Carbohydrate Polymers 216, 45–53. https://doi.org/10.1016/j.carbpol.2019.04.004

Zhang, X., Gao, M., Zhang, Y., Dong, C., Xu, M., Hu, Y., Luan, G., 2022. Effect of plasticizer and zein subunit on rheology and texture of zein network. Food Hydrocolloids 123, 107140. https://doi.org/10.1016/j.foodhyd.2021.107140

Zhang, Y., Zhang, N., Hingorani, H., Ding, N., Wang, D., Yuan, C., Zhang, B., Gu, G., Ge, Q., 2019. Fast-Response, Stiffness-Tunable Soft Actuator by Hybrid Multimaterial 3D Printing. Adv Funct Materials 29, 1806698. https://doi.org/10.1002/adfm.201806698

Zhao, Z., Fan, L., Song, G., Huo, M., 2024. Micelle-Cross-Linked Hydrogels with Strain Stiffening Properties Regulated by Intramicellar Cross-Linking. Chem. Mater. 36, 1436–1448. https://doi.org/10.1021/acs.chemmater.3c02570

Zheng, Q., Zhao, L., Wang, J., Wang, S., Liu, Y., Liu, X., 2020. High-strength and high-toughness sodium alginate/polyacrylamide double physically crosslinked network hydrogel with superior self-healing and self-recovery properties prepared by a one-pot method. Colloids and Surfaces A: Physicochemical and Engineering Aspects 589, 124402. https://doi.org/10.1016/j.colsurfa.2019.124402

Zhou, L., Pei, X., Fang, K., Zhang, R., Fu, J., 2020. Super tough, ultra-stretchable, and fast recoverable double network hydrogels physically crosslinked by triple non-covalent interactions. Polymer 192, 122319. https://doi.org/10.1016/j.polymer.2020.122319

Zhu, F., Lin, J., Wu, Z.L., Qu, S., Yin, J., Qian, J., Zheng, Q., 2018. Tough and Conductive Hybrid Hydrogels Enabling Facile Patterning. ACS Appl. Mater. Interfaces 10, 13685–13692. https://doi.org/10.1021/acsami.8b01873

Zhu, R., Jarkulisch, J., Schutyser, M.A.I., Boom, R.M., Zhang, L., 2025. Designing 3D-printed wheat starch cryogels: Effect of geometry on mechanical performance. Innovative Food Science & Emerging Technologies 102, 104003. https://doi.org/10.1016/j.ifset.2025.104003

Zondervan, R., Kulzer, F., Berkhout, G.C.G., Orrit, M., 2007. Local viscosity of supercooled glycerol near T_g probed by rotational diffusion of ensembles and single dye molecules. Proc. Natl. Acad. Sci. U.S.A. 104, 12628–12633. https://doi.org/10.1073/pnas.0610521104

Summary

Edible materials offer many opportunities outside of direct consumption as they are renewable, break down in the environment and can be digested safely. Formulating and processing edible materials can yield composite materials that have the capability to revolutionize applications that benefit human health, society and environment. These composites can be used in simple applications, such as packaging, or in further assemblies to construct edible robots and robotics foods. Based on bioinspired soft robotic design principles, two main composite groups of interest were identified: one stiff and rigid, and one soft and flexible. However, a rational approach to design and evaluate performance of these edible composites was still missing. At the composite level, structure-function relationships can be used to describe material behaviour. Understanding the relation between formulation, processing and final product properties therefore allows design guidelines to be derived for edible composite materials.

The aims of this thesis were therefore to identify how food process engineering and manufacturing technologies could be combined to fabricate rigid and flexible composites with desired material characteristics and identify how characterization methods could be applied to study the performance of food materials in non-food applications.

In **Chapter 2** an edible composite was developed which was suitable for fabrication of stiff and rigid objects using Fused Deposition Modelling 3D printing. Material requirements were established based on literature data. Properties of the composite were modulated by adjusting the formulation and processing, to match those requirements. The corn protein zein was found to be a suitable candidate due to its thermoplastic property, suitable melt flow behaviour, sintering ability and ability to be processed without crosslinking. Addition of plasticizer was required to decrease brittleness of the zein

composite. To obtain homogeneous dispersion of the plasticizer, a pelletisation process was developed which involved solubilisation, drying and grinding. The glass transition temperature of the composite was identified as a crucial parameter for controlling its processability. Based on thermal and rheological measurements of zein composites plasticized to different degrees a state diagram with iso-viscosity lines was established, which mapped the material state as function of solids content and temperature allowing the identification of suitable processing temperatures, e.g. for 3D printing. A Fused Deposition Modelling 3D printer was subsequently modified to be able to utilise pelletized materials as feedstock. The zein composite pellets were subsequently utilized to fabricate several demonstrator models, demonstrating that overhang angles up to 45° could be achieved and that no postprocessing was required to stabilize the object after printing. This study proved the feasibility of fused deposition modelling 3D printing with edible thermoplastic protein composites.

In **Chapter 3** the aim was to improve the compatibility of the zein composite with standardized FDM equipment that uses filament as feedstock in order to allow for easy adaptation in the marketplace. Filaments are long strands of extruded material wound on a spool. To provide the composite with sufficient flexibility for this winding process, the flexibility of the composite developed in **Chapter 2** needed to be improved. For this purpose, amphiphilic fatty acids were added to the formulation in addition to the hydrophilic plasticizer glycerol to reduce attractive forces between zein polymer molecules. This combination provided a synergistic effect on glass transition temperature, allowing the glass transition temperature to be reduced more than using just glycerol while maintaining phase compatibility. Furthermore, a relation between glass transition temperature and viscosity was found. After optimisation of the composite formulation, filament was produced on a pilot

scale continuous extruder, providing evidence that upscaling to industrial scale is possible. A standard, commercial FDM 3D printer was used to fabricate several objects with complex geometries using the manufactured zein filament to demonstrate its printing qualities. Additionally, mechanical properties of 3D printed specimens was compared to references made with common 3D printing plastics. This study showcased that thermoplastic protein filament can be produced on large scale and is compatible with commercial 3D printers, allowing more users to utilize the edible filament.

In **Chapter 4** the focus shifted to the development of soft and flexible edible hydrogels. The extensional properties of single biopolymer network (SN), crosslinked network (CN) and interpenetrating network (IPN) hydrogels as function of plasticizer content were studied. To evaluate stress-strain relations under biaxial loading conditions a custom bulge test utilizing computer-vision deformation tracking was developed. Deformation of films during the bulge test was accurately matched using an ellipsoid shape function, which allowed calculation of stress-strain curves. For IPN hydrogels, plasticizer content was found to have a different effect on the stress-strain relation based on the deformation mode (uniaxial or biaxial). This highlights the importance of evaluating material properties under the type of stress loading relevant to the final application. Furthermore, IPN hydrogels were found to exhibit very high tensile strength. This study revealed that network structure and plasticization level could be used to modulate the tensile properties of hydrogel films.

In **Chapter 5** the learnings from earlier chapters were reflected upon, general limitations were identified and directions for future research were provided. It was recommended to study the integration of the composites developed in this work in more complex assemblies to achieve a larger range of functionalities. To achieve this, the functionalities of the composites could be

further extended through inclusion of active fillers, such as activated carbon to impart conductive properties. Additionally, the FDM process could be used to control the macroscale properties of objects fabricated using edible filaments, allowing the range of composite properties to be further extended.

The results of this thesis present a rational material science approach to formulating and processing edible composite materials with designed material properties. The insights will contribute to the advancement of the field of edible robots and robotic foods, and beyond.

Samenvatting

Eetbare materialen zijn geschikt voor consumptie, maar omdat ze hernieuwbaar, biologisch afbreekbaar en veilig voor contact met mens en dier zijn, zijn ze daarnaast ook geschikt voor veel andere toepassingen. Met de juiste formuleringsstrategieën en verwerkingsprocessen kunnen eetbare materialen worden omgevormd tot composieten met de potentie om een revolutie teweeg te brengen in toepassingen op het gebied van gezondheid, maatschappij en milieu. Deze toepassingen variëren van eenvoudig, zoals eetbare verpakkingen, tot complex, zoals assemblages waarin deze composieten de basis vormen voor eetbare robots en robotisch voedsel. Klassieke robots bestaan uit rigide componenten en starre gewrichten, terwijl zachte robots juist geen volledig rigide onderdelen bevatten. Zachte robots kunnen zich daardoor in verschillende richtingen vervormen, waardoor ze zich goed aan kunnen passen aan hun omgeving en minder snel beschadigingen aanrichten. Op basis van algemene ontwerpprincipes voor biologisch geïnspireerde zachte robots kunnen twee complementaire typen composieten worden onderscheiden: enerzijds stijve, weinig buigzame composieten en anderzijds flexibele, zachte composieten. Er ontbrak echter nog een systematische benadering om zulke composieten te formuleren, verwerken en evalueren met eetbare materialen als uitgangspunt. Het materiaalgedrag van composieten kan worden beschreven met structuur-functierelaties. Inzicht in de relatie tussen formulering, verwerking en uiteindelijke materiaaleigenschappen maakt het mogelijk om ontwerpprincipes voor eetbare composieten af te leiden.

Het doel van dit proefschrift was daarom om te onderzoeken hoe kennis uit de levensmiddelentechnologie kan worden gecombineerd met productietechnieken om zowel stijve als flexibele composieten met gewenste materiaaleigenschappen te vervaardigen. Daarnaast werd onderzocht hoe karakteriseringsmethoden kunnen worden ingezet om de prestaties van

eetbare composieten in verschillende gebruiksscenario's accuraat te kunnen voorspellen.

In **Hoofdstuk 2** werd een eetbaar composiet ontwikkeld dat geschikt is om met behulp van de 3D-printtechniek Fused Deposition Modelling (FDM) stijve en rigide objecten te vervaardigen. De voor FDM vereiste materiaaleigenschappen werden afgeleid uit een literatuurstudie. De formulering en fabricagemethode van het composiet werden geoptimaliseerd om aan deze vereisten te voldoen. Het maiseiwit zeïne bleek een geschikte grondstof te zijn door zijn gunstige thermoplastische eigenschappen, vloeigedrag in gesmolten toestand, goede hechting met zichzelf bij hoge temperaturen en de mogelijkheid voor warme verwerking zonder vorming van sterke kruisverbindingen. Om de broosheid van het zeïnecomposiet te verminderen was toevoeging van weekmakers benodigd. Voor een homogene verdeling van de weekmakers in het composiet werd een pelletiseringsproces ontwikkeld, bestaande uit de verwerkingsstappen oplossen, drogen en vermalen. De glastransitietemperatuur van het composiet bleek een cruciale rol te spelen in zijn verwerkbaarheid. Op basis van thermische en reologische metingen aan zeïnecomposieten met verschillende hoeveelheden weekmakers kon een toestandsdiagram met isoviscositeitslijnen worden opgesteld. Dit diagram beschrijft de materiaaltoestand als functie van het drogestofgehalte en de temperatuur, wat inzicht geeft in de ideale verwerkingstemperatuur, bijv. voor 3D-printen. Een FDM-3D-printer werd aangepast om pellets te kunnen verwerken. De zeïnecomposietpellets werden vervolgens gebruikt om verschillende objecten te printen. De resultaten van deze printtesten laten zien dat overhanghoeken tot 45° geprint konden worden en dat de objecten na het printen stabiel en rigide waren. Met deze studie werd aangetoond dat het technisch haalbaar is om eetbare thermoplastische

eiwitcomposieten als grondstof te gebruiken voor de vervaardiging van stijve en rigide objecten middels FDM.

In **Hoofdstuk 3** was het doel om de compatibiliteit van het zeïnecomposiet met reguliere FDM-apparatuur te vergroten. Bij zulke apparatuur wordt de grondstof aangevoerd in de vorm van een filament. Een filament is een lange, geëxtrudeerde draad die om een spoel is gewikkeld. Om het composiet voldoende flexibiliteit te maken voor het wikkelingsproces, moest de flexibiliteit vergroot worden ten opzichte van het composiet dat in **Hoofdstuk 2** ontwikkeld werd. Daartoe werden, naast de hydrofiele weekmaker glycerol, amfifiele vetzuren aan de formulering toegevoegd. Deze vetzuren verminderen de aantrekkingskrachten tussen zeïnepolymeermoleculen. Deze combinatie van additieven had een synergetisch effect op de glastransitietemperatuur, waardoor deze verder verlaagd kon worden dan wanneer uitsluitend glycerol gebruikt zou worden, zonder dat hierbij fasescheiding optrad. Verder werd een verband tussen de glastransitietemperatuur en viscositeit aangetoond. Na optimalisatie van de samenstelling van het composiet werd het filament met een continu extrusieproces op pilotschaal geproduceerd. Hiermee werd aangetoond dat opschaling naar industriële productie mogelijk is. Vervolgens werd het geproduceerde filament met een commercieel verkrijgbare FDM-3D-printer verwerkt tot verschillende objecten met complexe geometrieën om de printkwaliteit van het ontwikkelde filament te kunnen beoordelen. Daarnaast werden proefmonsters geschikt voor buig- en trekproeven geprint, zodat de de mechanische eigenschappen van deze prints vergeleken konden worden met die van referentiemonsters vervaardigd uit veelgebruikte 3D-printkunststoffen. Deze studie toonde aan dat thermoplastisch filament op basis van eetbare materialen op industriële schaal geproduceerd kan worden en compatibel is met commerciële 3D-printers. Hiermee wordt het gebruik

van eetbare filamenten toegankelijk gemaakt voor een bredere groep gebruikers.

In **Hoofdstuk 4** verschoof de focus naar het ontwikkelen van eetbare hydrogels die zacht en flexibel zijn. De rekeigenschappen van gels met biopolymeernetwerken (SN), gekruislinkte netwerken (CN) en interpenetrerende netwerken (IPN) werden onderzocht als functie van hun weekmakergehalte. Om spanning-rek relaties onder biaxiale belasting (belasting over meerdere assen tegelijkertijd) te bepalen werd een pneumatische uitzettingstest ontwikkeld. Hierbij werd een dunne, cirkelvormige hydrogel ingeklemd tussen een matrijs en houder, waarna de druk onder het monster geleidelijk verhoogd werd waardoor het monster opbolt. De vormverandering tijdens deze proef werd nauwkeurig gevolgd met behulp van computervisie. De vervorming van de monsters kon nauwkeurig worden beschreven met een ellipsoïde vormfunctie, wat het berekenen van spanning-rek relaties mogelijk maakte. Voor IPN-hydrogels bleek het effect van het weekmakergehalte op de spanning-rekrelatie afhankelijk te zijn van de belastingswijze (uniaxiaal of biaxiaal). Dit onderstreepte het belang van het karakteriseren van materiaaleigenschappen onder de belastingswijzen die representatief zijn voor de uiteindelijke gebruiksscenario's. Daarnaast werd gevonden dat IPN-hydrogels een erg hoge treksterkte hadden. De studie toonde aan dat zowel de netwerkstructuur als het weekmakergehalte gebruikt kunnen worden om de rekeigenschappen van hydrogels aan te passen.

In **Hoofdstuk 5** werd gereflecteerd op de bevindingen uit voorgaande hoofdstukken, werden de beperkingen van het onderzoek besproken en werden aanbevelingen gedaan voor toekomstig onderzoek. Daarbij werd voorgesteld de in dit proefschrift ontwikkelde composieten te integreren in complexere assemblages om een breder scala aan functionaliteiten te

realiseren. Daarnaast kunnen de eigenschappen van deze composieten verder worden uitgebreid door er actieve vulstoffen in te verwerken, zoals actieve kool voor elektrische geleidbaarheid. Ook biedt het FDM-proces de mogelijkheid om, door middel van slimme ontwerpstrategieën, de macroscopische eigenschappen van objecten te sturen en daarmee het bereik aan realiseerbare materiaaleigenschappen verder te vergroten.

De resultaten van dit proefschrift vormen samen een systematische materiaalkundige benadering voor het formuleren en verwerken van eetbare materialen tot composieten met doelgericht ontworpen materiaaleigenschappen. De verkregen inzichten dragen bij aan de verdere ontwikkeling van eetbare robots, robotisch voedsel en andere innovatieve toepassingen van eetbare materialen.

Appendices

Acknowledgments / Dankwoord

About the author

Publications

Overview of completed training activities

Acknowledgements / Dankwoord

Over the years I have worked on this PhD, I have been lucky enough to receive support from many wonderful people. These people contributed to my work directly, inspired me, or cheered me on along the way. I dare say that the contribution of my friends, who helped me relax after a long day in the lab or spent time with me while I was running computations, was equally important. I would like to express my heartfelt gratitude to all of these people.

First of all, I would like to thank my supervision team for putting their faith in me and hiring me for the RoboFood project at the Food Process Engineering Group at Wageningen University back in 2021. **Lu**, thank you for our weekly meetings, your feedback and for stepping into the lab with me. Your suggestion to dissolve zein in ethanol turned out to be a pivotal step in the work on our first publication on the 3D printing of zein composites. **Remko**, thank you for the mountains of suggestions and ideas you shared throughout the years. It was fascinating to see how you could relate other works to mine and find similarities. It was always motivating to hear you speak about the potential of my work with unwavering enthusiasm. **Ruud**, thank you for sharing your approach to research, the nice symposium and your critical assessment of my work.

Ruihao, thank you for sharing this journey with me as my fellow RoboFood researcher at WUR. I truly enjoyed our discussions about electronics, design, 3D printing and crazy concepts for edible robots. What you taught me about SolidWorks and modifying 3D printers was an important stepping stone that enabled me to set up many experiments the way I wanted, and in a fast manner. Besides that, I am grateful for the dinners we shared, the lab visits and our work trips around Europe. Your excitement about new projects

provided a great boost of motivation, and I will forever remain curious about what the next DIY project on your schedule is going to look like.

Of course, I would like to thank the other members of the RoboFood consortium as well. **Lyneth**, thank you for your help in the lab. **Bokeon**, thank you for your help with pneumatic actuators and your contribution to the design of the edible spring and the collection of data on the spring constants. Your hard work did not go unnoticed. **Shuhang**, thank you for the honest conversations we had during the RoboFood meetings. **Giulia**, thank you for your help with the measurements of the conductive properties of the edible filaments. **Valerio**, it was always a great pleasure to talk to you, and it was a pleasure to work on the conductive filament together. **Alexander**, your jokes made my day whenever we had the opportunity to talk. A word of thanks to **Dario, Mario and Jonathan** for the RoboFood crash courses, allowing me to gain insight into your fields. Thank you also for the kind words about my work and the encouragement during all of the RoboFood meetings.

Over the years, I have been a bit of an office nomad, so I would like to thank the many people that I've had the pleasure of sharing an office with: **Patrick, Regina, Katharina, Hilda, Judith, Iris, Boxin, Martijn** and **Napasorn**. It was great to chat with you, get inspired, celebrate successes, share frustrations, listen to your stories and partake in fun office activities. The small and large things you shared with me over the years often helped me to explore new paths.

Another big thank you goes out to my fellow FPE colleagues. It was great to be able to talk to so many of you during the coffee and lunch breaks over the years. I also truly enjoyed all of the sports activities outside of office hours: the Veluweloop, the tournaments at Thymos and the early morning runs in

Singapore! I'd like to thank the **PhD-trip** committees for organising amazing trips to Singapore and the UK. There were also awesome group days, labuitjes and pizza dinners that I remember fondly.

Aadi, you were a joy to be around! Thank you for coming to Wageningen to chat and for including me in your layman's speech; it was an honour. **Kieke**, thank you for all the fun conversations at the lab and for listening to me express my frustrations. I enjoyed your crash course on pitch presentations a lot! **Julia**, your positive approach to tackling problems and ability to always find a way forward were truly inspiring. Thank you for asking me to help you out with some creative projects; it was a joy to work on them together. **Koen**, thank you for your encouragement over the years and your great energy as an athlete. It was great fun to join the training sessions you organised for the Veluweloop. **Jolien**, thank you for checking in on me when I needed it. **Lingfeng**, thank you for all of the sports activities. **Yifeng**, it was always nice to talk about travel, cats and 3D printing business opportunities with you. **Santiago**, thank you for your help with Python programming and for asking me to create a city for your D&D campaign—a fun challenge! **Napasorn**, I had a great time listening to your stories about food and travel. Thank you for the snacks you brought over the years and the fun board game nights. **Thijs**, thanks for the great introduction to survival runs and for helping me to become a better boulderer; it was great to learn from you! **Napasorn** and **Thijs**, I am grateful to have you by my side during my defence. **Meinou**, thank you for having me as part of the Mathematical Concepts for Food Technologists course crew! It reminded me of how much I loved mathematics. It was always fun to derive equations with you and to discuss scientific problems.

I dare say FPE has the best support crew a PhD could wish for. The technicians are simply amazing, and my work could not have been completed without them. **Jos**, thank you for always being available with a smile and helping me to resolve problems I had with all different types of equipment. I really appreciate that you never took no for an answer and really helped me to get the most out of the research equipment we had available. **Maurice**, thank you for your help with the microscopes and the fun board games. **Wouter**, it was great to have your support when I had issues with new software, and I enjoyed our chats about the most fun characters to play in the Diablo games. **Martin**, thank you for all the bookkeeping and other help over the years! **Anastasia**, your enthusiasm about the work we did in the lab was delightful, and a great motivator to see how far we could push the RoboFood experiments.

Throughout my PhD, I have participated in multiple fun and educational activities organised by the **VLAG** graduate school. I would like to thank **Jochem** in particular for our walks, conversations and calmly offering advice that was truly helpful. On that note, I am grateful that I was able to improve the lives of other PhDs a little as a member of the VLAG PhD council. **Katharina**, it was great to experience your chaotic energy as the chairperson, crack jokes together, complain about all of the things related to PhD life and eat cookies. **Robert**, thank you for being my co-secretary and making it super easy to keep track of everything. **Koen**, it was great to run into you again at the council after our time at the Wageningen Beasts. Thank you for sharing some of your amazing food with me.

I would also like to express my gratitude to the people at the workshop. **Eric**, it was always nice to hear you say that ‘of course you had some time for me’ when I approached you with yet another project. Thank you **Hans, Johan** and

Kyle for helping me to create custom equipment for my experiments. Your insights and expertise were crucial in getting everything to work smoothly.

All of my students made important contributions to my research, and I am proud that I could honour many of them by listing them as co-authors on my publications. **Gregorio**, thank you for your help in developing the lab protocols during the early stages of my research. **Marije**, dank voor jouw enthousiasme voor mijn project, de vele uren die je in het lab gemaakt hebt en de leuke gesprekken! **Naomi**, het was gaaf om te zien hoe jij de software voor het project met de filmblazer verder wist te ontwikkelen en hoe je mijn eigen programmeervaardigheden al snel wist te overtreffen. **Dyllan**, super om te zien hoe snel jij alles oppakte en hoe je binnen korte tijd veel verschillende materialen hebt weten te testen. Het was altijd leuk om jouw verhalen te horen tijdens de wekelijkse overleggen. **Leanne**, dank voor jouw uitgebreide werk en uitstekende verslaglegging, dit was erg behulpzaam bij het schrijven van mijn laatste publicatie! Het was bovendien erg gaaf om samen het opschalen van de filamentproductie te kunnen testen!

Guido, jij hebt op zoveel momenten tijdens mijn studie en carrière een belangrijke rol gespeeld, ik kan je daar niet genoeg voor bedanken. Aan jouw steun door de jaren heen heb ik veel gehad en je hebt mij geïnspireerd op wetenschappelijk vlak en zeker ook als atleet. I would also like to thank the members of the Geographically United Italians Doing Outdoor Sports club, better known as **Guido's** run club: **Giuseppe, Giulia, Elena, Kjelt, Stan, Timo, Siebrand, Andrei, Luk, Pavel, Pedro** and many others over the years. It was always nice to go for a run with you after work, discuss whether ticks are real (hint: they are) and participate in the Veluweloop. The recent additions of swimming and cycling sessions have been fun as well. It is

inspiring and super fun to be surrounded by such amazing athletes. I am looking forward to completing my first half-distance triathlon!

Remco en **Jeffrey**, ik geniet ervan dat wij vanuit de collegebanken samen gegroeid zijn van legendarische Hearthstone-spelers naar masters in Eternal en inmiddels lekker burgerlijk de Beleggende Bühlerboys vormen. Het is fijn om al zo lang met jullie bevriend te zijn en dat ik met jullie over alles kan praten. Jullie steun en adviezen hebben mij door de jaren heen ontzettend geholpen. Maar ook de leuke avonden waarop we Spirit Island speelden, de escape rooms, wandelingen en etentjes waren altijd fantastisch leuk en konden mij echt door een lange werkweek heen slepen. En wat gaaf om via jullie **Amy** en **Janneke** te leren kennen; ook jullie ontzettend bedankt voor de steun en leuke tijden samen!

Annika, thank you for introducing me to guided meditation. It helped me greatly to bring some calm to my mind when it was most needed.

João, chef, thank you for being my friend since our internship adventures in Belgium. I will never forget the barbecued fish from the nice ladies at the corner of the street and 'saving' all of the chocolate with hazelnuts from the bin by keeping it safe inside our bellies. It was and still is a great pleasure to practise crazy calisthenics moves and smash bike rides with you after work. Keeping the cadence correctly will be forever ingrained in my mind!

Alexandra, thank you for being by my side for such a large part of this journey. Thank you for providing a listening ear when I was burned out from work and reminding me that sometimes the solution is not to just work more. Thank you for cheering me on and reminding me that I have many skills. And most of all, thank you for teaching me that my achievements are worth celebrating.

Matijs, Erwin, Nick en **Karst**, bedankt voor de vele leuke avonden in Wageningen gevuld met Magic, de prereleases in Arnhem en MagicCon. Om uitspraken als ‘ik ga dit onthouden’ en ‘ga je nou de kleine man aanvallen’ kan ik nog steeds hard lachen. Het was altijd fijn om mijn werkdag los te kunnen laten tijdens een potje Magic. Ook de serieuze gesprekken die we samen hebben gehad waardeer ik heel erg. Ik kijk uit naar de vele leuke potten Magic die nog zullen volgen!

Mama, bedankt voor jouw onvoorwaardelijke steun. Het was fijn dat jij altijd beschikbaar was om naar mijn verhaal te luisteren. Ik kan **papa** en jou niet genoeg bedanken dat jullie mij altijd aangemoedigd hebben om mijn eigen pad te kiezen. **Mama, papa** en **Yorben**, bedankt voor al jullie hulp met mijn eerste eigen woning. Het is een fantastische plek geworden waar ik nog altijd met veel plezier woon.

En tot slot, **Anne**, bedankt voor alle hulp bij het maken van de schetsen voor mijn PhD-boekje. Dankzij jouw feedback zijn ze echt heel mooi geworden. En wat een geluk heb ik dat je naast alle leuke vogels ook mij ‘gespot’ hebt in het wild. Ik kijk er naar uit om nog veel meer mooie momenten met jou te kunnen delen!

About the author



Quinten Steffens was born on the 21st of November in Haarlem, the Netherlands. He studied Food Technology at Wageningen University, where he obtained his BSc degree cum laude in 2015. For his bachelor's thesis at the department of Food Quality and Design, Quinten investigated the use of glycated whey proteins to increase the melting point of white chocolate. He also completed a minor in Nutritional Sciences in France.

In 2017, Quinten obtained his MSc degree in Food Technology with a specialization in Gastronomy. His master's thesis focused on the contribution of dairy ingredients and sugar to the rheological and tribological behaviour of chocolate. He also completed an internship at Barry Callebaut in Belgium, where he worked on the development of a sugar-free chocolate.

After completing his master's degree, Quinten worked as a product developer before returning to academia as a junior scientist at Wageningen Food & Biobased Research. Here, he contributed to research on the protein transition and 3D food printing.

In 2021, Quinten started his PhD at the Food Process Engineering (FPE) group as part of the RoboFood consortium. His research explored how food process engineering and advanced manufacturing technologies can be combined to fabricate rigid and flexible food-based composites with tailored material properties. In addition, he investigated how characterization methods can be applied to evaluate the performance of food materials in non-food applications. The findings of his research are presented in this thesis.

Contact: quinten.steffens@hotmail.com

Publications

This thesis

Steffens, Q., Vliek, M., Van Der Sman, R., Boom, R., Zhang, L., (2025). 3D-printing of thermoplastic protein-based composites by fused deposition modelling. *Journal of Food Engineering*, 401, 112660.

Steffens, Q., Yu-Jing, D.G., Schuppert, N., Van Der Sman, R., Boom, R., Ma, Y., Zhang, L., (2026). Mechanical characterization of elastic edible films with single, crosslinked and interpenetrating biopolymer networks using combined uniaxial and biaxial analysis. *Current Research in Food Science*, 101381.

Submitted

Steffens, Q., Te Koppele, L,. Van der Sman, R.G.M., Boom, R. M., Zhang, L. (2026). Zein-based Edible Filament: Formulation Development, Fabrication and Fused Deposition Modelling Performance

Overview of completed training activities

Discipline specific activities	**Institute**	**Year**
Big Data Analysis in the Life Sciences	VLAG	2021
Consortium (project) meetings	EPFL	2021
4d printing online conference	Jakajima	2022
Edible soft matter	WUR	2023
Dutch soft robotics symposium	UT	2023
ICEF	GEPEA-Oniris	2023
Visit to collaborators lab	IIT	2023-2024
Edible soft matter in between fluid and solid states	WFBR / FPE	2024
General courses		
VLAG PhD week	VLAG	2022
Scientific Writing	WUR	2022
Seminar & Training on differential scanning calorimetry	TA instruments	2023
Research data management	FPE	2022
Soft robotics crash course	UoB, EPFL, IIT	2023-2025
Career perspectives	WGS	2025
Assisting in teaching and supervision activities		
Mathematical concepts for food technologists	FPE	2022-2024
BSc/MSc thesis supervision	FPE	2022-2025
Other activities		
Preparation of research proposal	FPE	2021-22
PhD study tour (Singapore)	FPE	2022
VLAG PhD council	WUR	2022-2023
PhD study tour (UK)	FPE	2024
FPE group weekly + monthly science meetings	FPE	2021-2025

About the cover

In this thesis, two research gaps were identified, namely:

1. “How can food process engineering and manufacturing technologies be combined to fabricate rigid and flexible composites with desired material characteristics?”
2. “How can food characterization methods be applied to study the performance of edible composites in non-food applications, like structural material engineering?”

The equipment required to answer these questions did not always exist, and when it did, it had not necessarily been used for the purposes we had in mind. It was therefore important to carefully conceptualise our experiments and the equipment required to carry them out. This stage is represented on the front and back covers by the pencil sketches.

Next, digital design tools were used to develop these concepts further. The rendered image of the equipment on the back cover represents this stage. Finally, we put the equipment to the test in the laboratory, a stage illustrated by the photograph on the front cover.

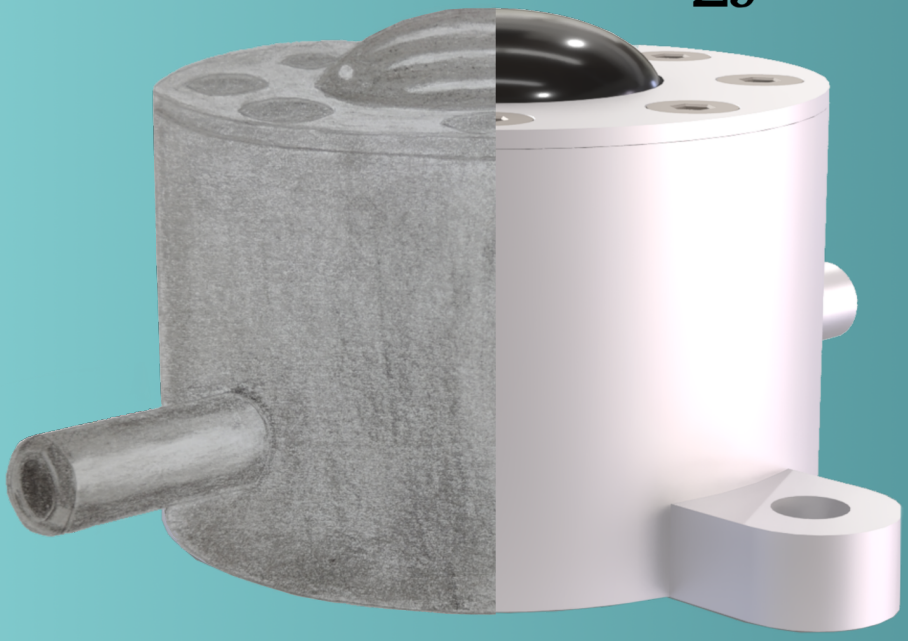
The photograph shows a 3D Benchy being printed. The 3D Benchy is a small 3D model that is commonly used as a diagnostic test when setting up a 3D printer or testing a new filament. Its design allows various aspects of print quality to be assessed, making it a suitable object for demonstrating the printability of the edible filament developed during this thesis.

The research described in this thesis was financially support by the European Union's Horizon 2020 research and innovation program under Grant Agreement #964596 ROBOFOOD.

Cover design by Quinten Steffens

Printed by ProefschriftMaken

$$\sigma_b = \frac{pR}{2s}$$



$$\varepsilon_3 = \ln\left(\frac{s}{s_0}\right) = -(\varepsilon_1 + \varepsilon_2)$$